

The University of Maine

DigitalCommons@UMaine

Electronic Theses and Dissertations

Fogler Library

Fall 12-15-2023

Compact VHF and UHF antennas for integration with SAW devices in harsh environment

Sri Lekha Srimat Kilambi

University of Maine, sri.srimat@maine.edu

Follow this and additional works at: <https://digitalcommons.library.umaine.edu/etd>



Part of the [Electromagnetics and Photonics Commons](#)

Recommended Citation

Srimat Kilambi, Sri Lekha, "Compact VHF and UHF antennas for integration with SAW devices in harsh environment" (2023). *Electronic Theses and Dissertations*. 3894.

<https://digitalcommons.library.umaine.edu/etd/3894>

This Open-Access Thesis is brought to you for free and open access by DigitalCommons@UMaine. It has been accepted for inclusion in Electronic Theses and Dissertations by an authorized administrator of DigitalCommons@UMaine. For more information, please contact um.library.technical.services@maine.edu.

**COMPACT VHF AND UHF ANTENNAS FOR INTEGRATION WITH SAW DEVICES
IN HARSH ENVIRONMENT**

By

Sri Lekha Srimat Kilambi

B.E. Osmania University, 2018

A THESIS

Submitted in Partial Fulfillment of the
Requirements for the Degree of
Master of Science
(in Electrical Engineering)

The Graduate School

The University of Maine

December 2023

Advisory Committee:

Mauricio Pereira da Cunha, Professor of Electrical and Computer Engineering, Advisor

Nuri Emanetoglu, Associate Professor of Electrical and Computer Engineering

Donald Hummels, Professor of Electrical and Computer Engineering

© Sri Lekha Srimat Kilambi 2023
All Rights Reserved

COMPACT VHF AND UHF ANTENNAS FOR INTEGRATION WITH SAW DEVICES IN HARSH ENVIRONMENT

By Sri Lekha Srimat Kilambi

Thesis Advisor: Dr. Mauricio Pereira da Cunha

An Abstract of the Thesis Presented
In Partial Fulfillment of the Requirements for the
Degree of Master of Science
(in Electrical Engineering)
December 2023

With increasing demand for harsh environment (HE) wireless sensor applications, the need for antennas capable of operating under temperatures up to 1000° C and under corrosive and erosive environments also increases. These environments place severe survivability, stability, and performance demands on antennas designed and fabricated to operate in such conditions.

This work focuses on the design, fabrication, simulation and performance investigation of a compact (~1/25th to 1/10th of a wavelength) combined helical and microstrip antenna design operating as a normal mode helical antenna structure (NMHAS) around 300MHz. The ground plane of the microstrip line also serves as a ground plane to the helical structure radiating element. It was found that varying the length of the microstrip line and associated ground plane from 0.5 inch to 3 inches resulted in the decrease of the measured NMHAS operating frequency and also affected the reactive response of the antenna. A compact 1:1 balun transformer was used to partially decouple the integrated NMHAS from the external sheath of the coaxial cable connected to a vector network analyzer, used to measure the NMHAS scattering (S) parameters. The balun parasitics network was modeled and simulated with the aid of ADS software. The NMHAS S_{11} and corresponding impedance response were also simulated on two different platforms, ANSYS-

HFSS and WIPL-D Pro, and compared to the measured frequency responses. The effect of the helix orientation with respect to the microstrip line plane on the response of NMHAS was also measured and found to have an impact in the antenna impedance response. Finally, the transmission loss of two similar NMHASs placed at different distances apart from each other was measured with and without the presence of an additional matching network. It was found that at the measured distances between 10 inch and 44 inches, the two NMHASs interact, thus affecting each other's impedance when compared to each NMHAS structure operating alone. This work confirmed that the NMHAS serves as a viable antenna structure for HE wireless sensor applications, owing to its utilization of air as a dielectric, compact design, and ease of integration.

DEDICATION

This thesis is dedicated in memory of my grandmother, Gomattam Janaki.

ACKNOWLEDGEMENT

I would like to take this opportunity to express my heartfelt gratitude to the individuals who played a pivotal role. Without their unwavering support, guidance, and encouragement, this endeavor would not have been possible.

First and foremost, I extend my deepest appreciation to my advisor, Prof. Mauricio Pereira da Cunha. Your mentorship was instrumental in shaping the direction of this research and in my growth as a scholar. Your patience, wisdom, and dedication to my intellectual development have been invaluable. I am grateful for the countless hours you spent guiding me through the research process, providing critical feedback, and helping me navigate the challenges that arose along the way.

I would like to thank Prof. Herbert Aumann for his valuable help in understanding the antenna basics and introducing a new modeling platform. I would like to thank David Leff for his help with laboratory equipment.

Additionally, I extend my thankfulness to the Castle Professorship for the financial support of my research, the partial support of DOE through the grant DE-SC0021981, and to the ECE department and FIRST for granting me access to their research facilities.

I would like to extend my gratitude to my friends and family for their unwavering support, understanding, and encouragement throughout this journey. I am grateful to Jyothi Niveditha, Praveen Kumar, and Bhargavi for their faith in my abilities, and their unwavering support in maintaining my morale.

TABLE OF CONTENTS

DEDICATION	iii
ACKNOWLEDGEMENT	iv
LIST OF TABLES	x
LIST OF FIGURES	xi
Chapter 1. INTRODUCTION	1
1.1 Some Harsh Environment Antenna Applications and Technologies	2
1.1.1 Harsh Environment Antenna Applications	2
1.1.2 HT/HE Antennas and Technologies	4
1.2 Antennas in HT / HE: Materials and Desired Design Characteristics	7
1.2.1 Air as Dielectric for HT antennas	9
1.3 Antenna Theory Terminology	10
1.4 Far field, Near Field and Field Coupled Antennas.....	13
1.4.1 Far Field Antennas	13
1.4.2 Near Field Antennas:	14
1.5 Helical Antenna.....	15
1.5.1 Helix Geometry.....	16
1.5.2 Transmission and Radiation Modes of Monofilar Helices	19
1.6 Goals and Scope	20
1.7 Thesis Organization.....	21

Chapter 2. NORMAL MODE HELICAL ANTENNA DESIGN AND IMPLEMENTATION.....	23
2.1 Theory of Normal Mode Helical Antenna	23
2.2 NMHA Structure Design Implemented in this work	30
2.3 NMHA Structure Notation.....	31
2.4 Direct Connection at the End of the Coaxial Cable	33
2.5 Conclusions	36
Chapter 3. NMHAS SIMULATIONS	37
3.1 Simulation of NMHAS on HFSS	37
3.1.1 Half-inch Microstrip Line.....	37
3.1.2 One-inch Microstrip Line	39
3.1.3 Two-inch Microstrip Line.....	41
3.1.4 Three-inch Microstrip Line.....	43
3.1.5 Consideration of the Microstrip Length on the Calculations of the NMHAS Impedance using HFSS.....	45
3.2 Simulations of NMHAS on WIPL-D.....	49
3.2.1 Half-inch Microstrip Line	50
3.2.2 One-inch Microstrip Line	52
3.2.3 Two-inch Microstrip Line.....	53
3.2.4 Three-inch Microstrip Line.....	55

3.2.5	Discussion of Microstrip Length Effect on the NMHAS Impedance	
	Calculation using WIPL-D	57
3.3	Comparison of HFSS and WIPL-D Simulations:	61
3.4	Sensitivity of NMHAS.....	62
3.4.1	Variation of D_h	62
3.4.2	Variation of H	64
3.3	Conclusions	66
Chapter 4. NMHAS FABRICATION AND EXPERIMENTAL SETUP		
	IMPLEMENTATION.....	67
4.1	Introduction of Balun	67
4.2	Modeling of the Balun Mounted between the Coaxial Cable and the NMHAS	67
4.3	Extraction of Equivalent Network Circuit Components for Parasitics in the	
	Balun Equivalent Fixture	70
4.4	NMHAS Impedance Response Variation due to Fabrication Procedure	73
4.4.1	Comparison of Four Similarly Fabricated Helices	73
4.4.2	Comparison of Balun Jigs.....	76
4.5	Implementation of Impedance Matching Network	78
4.6	Conclusions	79
Chapter 5. NMHAS MEASUREMENTS AND ANALYSIS		
5.1	Experimental Setups.....	81

5.2	Measurements in Laboratory Setup.....	82
5.3	Measurements in Anechoic Chamber	84
5.4	Comparing Measurements using the Laboratory Fixture and the Anechoic Chamber	85
5.5	Comparison of Measurements and Simulation:	86
5.6	Helix Structure Oriented in Different Directions	88
5.7	Full S-parameter Measurements for two NMHAS Facing Each Other	92
5.7.1	S-parameter Measurements Without Impedance Matching Network.....	92
5.7.2	S-parameters Measurement with Additional Impedance Matching Circuit	99
5.8	Conclusion.....	105
Chapter 6.	CONCLUSIONS.....	107
6.1	Summary of work and Conclusion.....	107
6.2	Major findings and contributions from this work	109
6.3	Suggested future work.....	110
	REFERENCES	111
	APPENDICES	118
APPENDIX A.	Simulations of nmhas with helix 2	118
APPENDIX B.	Measurement of Helix 2 connected to different microstrip lines	127
APPENDIX C.	Transferring of impedance.....	135
APPENDIX D.	Sensitivity of nmhas to physical dimensions of the structure	137

BIOGRAPHY OF THE AUTHOR..... 141

LIST OF TABLES

Table 2.1: Dimensions of the NMHAS.....	33
Table 3.1: Input impedance simulated on HFSS and transferred input impedance.....	47
Table 3.2: Change in resonant frequency with increase in length of microstrip line on HFSS	47
Table 3.3: Input impedance simulated on WIPL-D and transferred input impedance.	58
Table 3.4: Change in resonant frequency and input impedance with increase in length of microstrip line on WIPL-D.	58
Table 3.5: Change in resonant frequency with respect to change in diameter of helix.	64
Table 3.6: change in resonant frequency with respect to change in height of helix.	66
Table 4.1: Measured S_{11} and input impedance for the fixtures shown in Figure 4.2.....	69
Table 4.2: Optimized values of L, C and Φ for different loads	71
Table A.1: Dimensions of Helix 2	118

LIST OF FIGURES

Figure 1.1: (a)-(b) The basic PIFA structure and (c)-(d) its electrically smaller version [34]	7
Figure 1.2: Near and far field regions of an antenna	13
Figure 1.3: Geometry of helix [53]	15
Figure 1.4: Geometry and dimensions of a helix	17
Figure 1.5: Relationship between C, S, L and α of a helix [53].	17
Figure 1.6: Helix chart showing the location of different modes of operation as a function of helix dimensions [53].	18
Figure 2.1: Field patterns along with relative size indicated of: (a.) axial; (b.) 4-lobed ; (c) normal mode helical antennas [53].....	24
Figure 2.2: Dimensions for: (a.) helix; (b.) loop; (c.) dipole [53].....	25
Figure 2.3: Modified helix for normal-mode calculations [53].	26
Figure 2.4: Resonant narrowband circularly polarized monofilar normal-mode coil, pattern is that of a short dipole [53].	28
Figure 2.5: Resonant monofilar normal mode helical antenna mounted over a ground plane as substitute for $\lambda/4$ stub [53].	30
Figure 2.6: A car smart key with normal mode helical antenna connected to the circuit board.	31
Figure 2.7: Geometry of NMHAS.	32
Figure 2.8: Helical antenna connected to a SMA connector.	34
Figure 2.9: Four different microstrip structures connected to helical structure.....	35
Figure 3.1: (a) Top-view of helix connected to half-inch microstrip line; (b) Side-view of helix connected to half-inch microstrip line.	38

Figure 3.2: Frequency response of helix connected at the end of half-inch microstrip line: a) magnitude of reflection coefficient [dB]; b) real part of impedance [Ω]; c) imaginary part of the impedance [Ω].	39
Figure 3.3: a.) Top-view of the helix connected to one-inch microstrip line; b.) Side-view of the helix connected to one-inch microstrip line.....	40
Figure 3.4: Frequency response of helix connected at the end of one-inch microstrip line: a) magnitude of reflection coefficient [dB]; b) real part of impedance [Ω]; c) imaginary part of the impedance [Ω]......	41
Figure 3.5: a.) Top-view of the helix connected to two-inch microstrip line; b.) Side-view of the helix connected to two-inch microstrip line.	42
Figure 3.6: Frequency response of helix connected at the end of two-inch microstrip line: a) magnitude of reflection coefficient [dB]; b) real part of impedance [Ω]; c) imaginary part of the impedance [Ω]......	43
Figure 3.7: a.) Top-view of the helix connected to three-inch microstrip line; b.) Side-view of the helix connected to three-inch microstrip line.....	44
Figure 3.8: Frequency response of helical structure connected at the end of three-inch microstrip line: a) magnitude of reflection coefficient [dB]; b) real part of impedance [Ω]; c) imaginary part of the impedance [Ω]......	45
Figure 3.9: Reference points for transferring the impedance.	46
Figure 3.10: Smith plots of simulated and transferred impedance presented in Table 3.1 for: a.) half-inch microstrip line; b.) one-inch microstrip line; c.) two-inch microstrip line; d.) three-inch microstrip line	48

Figure 3.11: Transferred impedances to Point L in Figure 3.9 for different microstrip lengths plotted on Smith Chart calculated from HFSS simulations.	49
Figure 3.12: a.) NMHAS design simulated on WIPL-D; b) Trapezoidal plates with wire and generator connected between them.	50
Figure 3.13: Helix connected to half-inch microstrip line simulated on WIPL-D. The gray area is the axes on WIPL-D.	50
Figure 3.14: Frequency response of helix connected at the end of half-inch microstrip line: a) magnitude of reflection coefficient [dB]; b) real part of impedance [Ω]; c) imaginary part of the impedance [Ω].	51
Figure 3.15: Helix connected to one-inch microstrip line simulated on WIPL-D. The gray area is the axes on WIPL-D.	52
Figure 3.16: Frequency response of helix connected at the end of one-inch microstrip line: a) magnitude of reflection coefficient [dB]; b) real part of impedance [Ω]; c) imaginary part of the impedance [Ω].	53
Figure 3.17: Helix connected to two-inch microstrip line simulated on WIPL-D. The gray area is the axes on WIPL-D.	54
Figure 3.18: Frequency response of helix connected at the end of two-inch microstrip line: a) magnitude of reflection coefficient [dB]; b) real part of impedance [Ω]; c) imaginary part of the impedance [Ω].	55
Figure 3.19: Helix connected to three-inch microstrip line simulated on WIPL-D. The gray area is the axes on WIPL-D.	56

Figure 3.20: Frequency response of helix connected at the end of three-inch microstrip line: a) magnitude of reflection coefficient [dB]; b) real part of impedance [Ω]; c) imaginary part of the impedance [Ω].	57
Figure 3.21: Smith plots of simulated and transferred impedance presented in Table 3.3 and Table 3.1 for: a.) half-inch microstrip line; b.) one-inch microstrip line; c.) two-inch microstrip line; d.) three-inch microstrip line	59
Figure 3.22: Transferred impedances to Point L in Figure 3.9 for different microstrip lengths plotted on Smith Chart calculated from WIPL-D simulations.	60
Figure 3.23: Simulated NMHAS input impedance utilizing both WIPL-D and HFSS: a.) real part input impedance [Ω]; b.) imaginary part of input impedance [Ω].	61
Figure 3.24: Frequency response of NMHAS with two-inch microstrip line with respect to variation in D_h : a.) $ S_{11} $ [dB]; b.) real part of input impedance [Ω]; c.) imaginary part of input impedance [Ω].	63
Figure 3.25: Frequency response of NMHAS with two-inch microstrip line w.r.to variation in H: a.) $ S_{11} $ [dB]; b.) real part of input impedance [Ω]; c.) imaginary part of input impedance [Ω].	65
Figure 4.1: TC1-1-13M+ RF Transformer [77].	68
Figure 4.2: Different loads connected to balun: a) 25 Ω ; b.) 50 Ω ; c.) 100 Ω ; d) 150 Ω ; e) baluns connected end to end.	69
Figure 4.3: Balun equivalent circuit.	70
Figure 4.4: NMHAS balun connected at input.	72
Figure 4.5: a) NMHAS measurement block diagram; b.) Balun equivalent circuit: parameters obtained through measurement and error minimization.	72

Figure 4.6: Four similarly wound helices connected to same two-inch microstrip line.	74
Figure 4.7: Frequency response of four similarly wound helices connected to same two-inch microstrip line: a) $ S_{11_NMHAS} $ [dB]; b) $\text{Re}(Z_{in_NMHAS})$ [Ω]; c) $\text{Im}(Z_{in_NMHAS})$ [Ω].	75
Figure 4.8: Two-inch microstrip line connected to: a.) Balun Jig 1; b.) Balun Jig 2.....	76
Figure 4.9: S-parameter response of balun Jigs 1 and 2 connected to same helix at the end of two-inch microstrip line: a) $ S_{11_NMHAS} $ [dB]; b) $\text{Re}(Z_{in_NMHAS})$ [Ω]; c) $\text{Im}(Z_{in_NMHAS})$ [Ω].	77
Figure 4.10: Impedance matching network implemented on ADS.....	78
Figure 4.11: FR-4 board outline fabricated to hold the LC matching circuit.	79
Figure 5.1: Test setups used: a.) microwave engineering lab test bench; b.) anechoic chamber.	82
Figure 5.2: Measured S_{11} , S_{11_MEAS} utilizing the measurement setup of Figure 5.1a at the balun input-plane A (solid line) and translated S_{11} , S_{11_NMHAS} , at the input of the integrated microstrip and helical structure input-plane B (dashed line) displayed as: a.) $ S_{11} $ [dB]; b.) real part of the impedance [Ω]; c.) imaginary part of the impedance [Ω].	83
Figure 5.3: Measured S_{11} , S_{11_MEAS} utilizing the measurement setup of Figure 5.1b at the balun input-plane A (solid line) and translated S_{11} , S_{11_NMHAS} , at the input of the integrated microstrip and helical structure input-plane B (dashed line) displayed as: a.) $ S_{11} $ [dB]; b.) real part of the impedance [Ω]; c.) imaginary part of the impedance [Ω].	84

Figure 5.4: Frequency response of NMHAS as measured using laboratory fixture (solid) and in anechoic chamber (dashed) : a) $ S_{11_NMHAS} $ [dB]; b) real part of impedance [Ω]; c) imaginary part of impedance [Ω].	85
Figure 5.5: Simulated and measured $ S_{11} $ response of NMHAS.	87
Figure 5.6: Real part of impedance response of simulated and measured NMHAS.	87
Figure 5.7: Imaginary part of impedance response of simulated and measured NMHAS.	88
Figure 5.8: Helix oriented along different directions with respect to microstrip line: a.) X- direction; b.) Y-direction; c.) +Z-direction; d) -Z-direction.	89
Figure 5.9: S_{11_NMHAS} (at reference Plane B) for the NMHAS structure connected along X- direction, +Z-direction, -Z-direction and Y-direction.	90
Figure 5.10: Real part of Z_{NMHAS} (at reference Plane B) for the NMHAS structure connected along X-direction, +Z-direction, -Z-direction and Y-direction.	90
Figure 5.11: Imaginary part of Z_{NMHAS} (at reference Plane B) for the NMHAS structure connected along X-direction, +Z-direction, -Z-direction and Y-direction.	91
Figure 5.12: NMHAS mounted on antenna mounting structure and spaced 44 inches apart.	93
Figure 5.13: Frequency response of the antenna structures spaced 44 inches apart: a.) $ S_{11} $ and $ S_{22} $ [dB]; b.) $ S_{12} $ [dB]; c.) $\text{Re}(Z_{MEAS})$ [Ω]; d.) $\text{Im}(Z_{MEAS})$ [Ω].	94
Figure 5.14: NMHAS mounted on antenna mounting structure and spaced 22 inches apart.	95
Figure 5.15: Frequency response of the antenna structures spaced 22 inches apart: a.) $ S_{11} $ and $ S_{22} $ [dB]; b.) $ S_{12} $ [dB]; c.) $\text{Re}(Z_{MEAS})$ [Ω]; d.) $\text{Im}(Z_{MEAS})$ [Ω].	96
Figure 5.16: NMHAS mounted on antenna mounting structure and spaced 10 inches apart.	97
Figure 5.17: Frequency response of the NMHAS spaced 10 inches apart: a.) $ S_{11} $ and $ S_{22} $ [dB]; b.) $ S_{12} $ [dB]; c.) $\text{Re}(Z_{MEAS})$ [Ω]; d.) $\text{Im}(Z_{MEAS})$ [Ω].	98

Figure 5.18: The NMHAS spaced 44 inches apart with the matching circuit connected. 99

Figure 5.19: Frequency response of the NMHAS with matching network spaced 44 inches
apart: a.) $|S_{11}|$ and $|S_{22}|$ [dB]; b.) $|S_{12}|$ [dB]; c.) $\text{Re}(Z_{\text{MEAS}})$ [Ω]; d.) $\text{Im}(Z_{\text{MEAS}})$ [Ω]. 100

Figure 5.20: The NMHAS spaced 22 inches apart with the matching network connected. 101

Figure 5.21: Frequency response of the NMHAS with matching network spaced 22 inches
apart: a.) $|S_{11}|$ and $|S_{22}|$ [dB]; b.) $|S_{12}|$ [dB]; c.) $\text{Re}(Z_{\text{MEAS}})$ [Ω]; d.) $\text{Im}(Z_{\text{MEAS}})$ [Ω]. 102

Figure 5.22: The NMHAS spaced 10 inches apart with the matching network connected. 103

Figure 5.23: Frequency response of the NMHAS with matching network spaced 10 inches
apart: a.) $|S_{11}|$ and $|S_{22}|$ [dB]; b.) $|S_{12}|$ [dB]; c.) $\text{Re}(Z_{\text{MEAS}})$ [Ω]; d.) $\text{Im}(Z_{\text{MEAS}})$ [Ω]. 104

Figure A.1: Frequency response of Helix 2 connected at the end of half-inch microstrip
line simulated on HFSS: a) $|S_{11_Simulated}|$ [dB]; b) $\text{Re}(Z_{in_Simulated})$ [Ω];
c) $\text{Im}(Z_{in_Simulated})$ [Ω]. 119

Figure A.2: Frequency response of Helix 2 connected at the end of one-inch microstrip
line simulated on HFSS: a) $|S_{11_Simulated}|$ [dB]; b) $\text{Re}(Z_{in_Simulated})$ [Ω];
c) $\text{Im}(Z_{in_Simulated})$ [Ω]. 120

Figure A.3: Frequency response of Helix 2 connected at the end of two-inch microstrip
line simulated on HFSS: a) $|S_{11_Simulated}|$ [dB]; b) $\text{Re}(Z_{in_Simulated})$ [Ω];
c) $\text{Im}(Z_{in_Simulated})$ [Ω]. 121

Figure A.4: Frequency response of Helix 2 connected at the end of three-inch microstrip
line simulated on HFSS: a) $|S_{11_Simulated}|$ [dB]; b) $\text{Re}(Z_{in_Simulated})$ [Ω];
c) $\text{Im}(Z_{in_Simulated})$ [Ω]. 122

Figure A.5: Frequency response of Helix 2 connected at the end of half-inch microstrip line simulated on WIPL-D: a) $ S_{11_Simulated} $ [dB]; b) $\text{Re}(Z_{in_Simulated})$ [Ω]; c) $\text{Im}(Z_{in_Simulated})$ [Ω].	123
Figure A.6: Frequency response of Helix 2 connected at the end of one-inch microstrip line simulated on WIPL-D: a) $ S_{11_Simulated} $ [dB]; b) $\text{Re}(Z_{in_Simulated})$ [Ω]; c) $\text{Im}(Z_{in_Simulated})$ [Ω].	124
Figure A.7: Frequency response of Helix 2 connected at the end of two-inch microstrip line simulated on WIPL-D: a) $ S_{11_Simulated} $ [dB]; b) $\text{Re}(Z_{in_Simulated})$ [Ω]; c) $\text{Im}(Z_{in_Simulated})$ [Ω].	125
Figure A.8: Frequency response of Helix 2 connected at the end of three-inch microstrip line simulated on WIPL-D: a) $ S_{11_Simulated} $ [dB]; b) $\text{Re}(Z_{in_Simulated})$ [Ω]; c) $\text{Im}(Z_{in_Simulated})$ [Ω].	126
Figure B.1: Measured response of Helix 2 connected to half inch microstrip line in setup shown in Figure 5.1a: a.) $ S_{11_NMHAS} $ [dB]; b.) $\text{Re}(Z_{in_NMHAS})$ [Ω]; c) $\text{Im}(Z_{in_NMHAS})$ [Ω].	127
Figure B.2: Measured response of Helix 2 connected to one inch microstrip line in setup shown in Figure 5.1a: a.) $ S_{11_NMHAS} $ [dB]; b.) $\text{Re}(Z_{in_NMHAS})$ [Ω]; c) $\text{Im}(Z_{in_NMHAS})$ [Ω].	128
Figure B.3: Measured response of Helix 2 connected to two inch microstrip line in setup shown in Figure 5.1a: a.) $ S_{11_NMHAS} $ [dB]; b.) $\text{Re}(Z_{in_NMHAS})$ [Ω]; c) $\text{Im}(Z_{in_NMHAS})$ [Ω].	129

Figure B.4: Measured response of Helix 2 connected to three inch microstrip line in setup shown in Figure 5.1a: a.) $ S_{11_NMHAS} $ [dB]; b.) $\text{Re}(Z_{in_NMHAS})$ [Ω]; c) $\text{Im}(Z_{in_NMHAS})$ [Ω].	130
Figure B.5: Measured response of Helix 2 connected to half inch microstrip line in setup shown in Figure 5.1b: a.) $ S_{11_NMHAS} $ [dB]; b.) $\text{Re}(Z_{in_NMHAS})$ [Ω]; c) $\text{Im}(Z_{in_NMHAS})$ [Ω].	131
Figure B.6: Measured response of Helix 2 connected to one inch microstrip line in setup shown in Figure 5.1b: a.) $ S_{11_NMHAS} $ [dB]; b.) $\text{Re}(Z_{in_NMHAS})$ [Ω]; c) $\text{Im}(Z_{in_NMHAS})$ [Ω].	132
Figure B.7: Measured response of Helix 2 connected to two inch microstrip line in setup shown in Figure 5.1b: a.) $ S_{11_NMHAS} $ [dB]; b.) $\text{Re}(Z_{in_NMHAS})$ [Ω]; c) $\text{Im}(Z_{in_NMHAS})$ [Ω].	133
Figure B.8: Measured response of Helix 2 connected to three inch microstrip line in setup shown in Figure 5.1b: a.) $ S_{11_NMHAS} $ [dB]; b.) $\text{Re}(Z_{in_NMHAS})$ [Ω]; c) $\text{Im}(Z_{in_NMHAS})$ [Ω].	134
Figure C.1: Representation of MATLAB code implemented.	135
Figure D.1: Compressed helix connected to a two inch microstrip line mounted on a tripod in the anechoic chamber.	137
Figure D.2: Measured response of compressed helical structure when connected to a two inch microstrip line: a.) $ S_{11_NMHAS} $ [dB]; b.) $\text{Re}(Z_{in_NMHAS})$ [Ω]; c.) $\text{Im}(Z_{in_NMHAS})$ [Ω].	138
Figure D.3: Elongated helix connected to a two inch microstrip line mounted on a tripod in the anechoic chamber.	139

Figure D.4: Measured response of elongated helical structure when connected to a two
inch microstrip line: a.) $|S_{11_NMHAS}|$ [dB]; b.) $\text{Re}(Z_{in_NMHAS})$ [Ω];

c.) $\text{Im}(Z_{in_NMHAS})$ [Ω]. 140

CHAPTER 1. INTRODUCTION

The demand for wireless sensing in harsh-environment (HE) applications with small, difficult to reach spaces and/or complex metallic industrial or power plant structures has been rising over the past few decades [1]-[7]. Various industries require HE sensors, including power generation industry, aerospace and other defense related industries, including powerplant equipment such as furnaces, turbines, boilers, and heat pumps, ceramic and metallurgic industries [8]-[18]. Wireless sensor operation is very attractive for HT HE applications, since it allows for sensor mobility, easier placement in hard to reach and out of line-of-sight areas [7]. Together with other technologies, such as surface acoustic wave [1], wireless sensing allows for operation on moving and rotating parts, without the need of wires directly connected to the sensor to provide power and collect information.

The increased demand in wireless sensor applications, increases the need for antennas. The insertion of the sensor and antenna integrated structure in HE environment, places severe survivability, stability, and performance demands on antennas designed and fabricated to operate in such conditions. Sensors and antennas used in such systems need to be robust and often be able to withstand one or more of the following environmental situations: erosive and/or corrosive conditions, high pressure, high temperature, high radiation and high rotational speed (for example in case of turbines). These harsh environments generally degrade the efficiency, durability and usability of various widely used electronics [19]. Therefore, the integrated sensor and respective antenna must withstand extreme environments for sensing and communication purposes.

1.1 Some Harsh Environment Antenna Applications and Technologies

Antennas are devices that are designed to transmit or receive electromagnetic waves. They are essential components of wireless communication systems, as they enable the transmission and reception of information wirelessly. Harsh environment antennas are essential in various industries and applications where traditional antennas may not withstand extreme conditions such as extreme temperatures, moisture, corrosion, vibration, and mechanical stress. These antennas are designed to provide reliable communication and signal reception in challenging environments.

1.1.1 Harsh Environment Antenna Applications

Some examples of industries and applications where harsh environment antennas are required include:

- **Oil and gas industry**: In offshore drilling and production operations, antennas are used for underwater communication, data transmission and remote control of equipment. These antennas must withstand extreme pressure, saltwater corrosion and low temperatures at ocean depths. They are typically housed in rugged enclosures with specialized materials to prevent water ingress [20].
- **Aerospace and aviation**: Antennas on aircraft serve various purposes, including communication, navigation and weather radar. They are designed to withstand the rigors of flight, including aerodynamic forces, temperature fluctuations and lightning strikes. Composite materials are often used to reduce weight and enhance durability [21].
- **Military and defense**: Antennas on military vehicles, such as tanks and armored personnel carriers, need to operate in rugged environments, including combat zones. They must be robust to withstand shocks, vibrations and harsh weather conditions while maintaining reliable communication and data links [22].

- **Maritime and shipping**: Antennas on ships are exposed to saltwater corrosion, mechanical stress from waves and extreme weather conditions. They are often made of corrosion-resistant materials like stainless steel and designed to be watertight [23].
- **Mining industry**: Underground mining operations require communication systems to ensure safety and coordination. Antennas in mines need to endure dust, moisture, and mechanical stress. Ruggedized enclosures and protective coatings are often used to mitigate these challenges [24].
- **Industrial Automation**: In industrial environments, antennas are used for wireless communication in automation and control systems. They may be exposed to extreme temperatures, humidity, and electromagnetic interference. Industrial-grade antennas are designed to withstand these conditions while ensuring reliable data transmission [25].
- **Environmental monitoring**: Antennas used in weather monitoring stations and environmental research need to be weatherproof. They should resist exposure to rain, snow, and temperature variations. Enclosures with weatherproof seals are commonly used to protect these antennas [26].
- **Medical Applications**: Medical implants prioritize the compactness of the system and they also be considered to operate under harsh environments [27]. As discussed in [27], a comprehensive examination of the deployment of a normal mode helical antenna in healthcare, involves evaluating physiological processes and relaying acquired data to the patient or medical professional. The antenna's compactness is essential in reducing discomfort during implantation in the human body. The paper showcases the transmission and reception of signals between helical antennas and the exchange of information between an antenna and a smartphone.

1.1.2 HT/HE Antennas and Technologies

High temperature (HT) condition is a particular case of harsh environment. In developing passive sensing technologies to operate in HT HE, one targets to not depend on external power supplies, long cables or transmission lines in such environments [1]. Therefore wireless operation of passive sensors is very attractive [28], which of course must rely on dependable, long lasting antennas equally capable of operating in such HT HE conditions. There is a significant demand for wireless passive sensors designed to function in ultra-harsh environments in order to monitor structural integrity [29]. When compared to physical wires, wireless devices are more cost-effective to maintain in high-temperature settings and are less prone to malfunctions. In [29] wireless sensors were designed using conductive carbon paste with polymer derived ceramic silicon carbon nitride disk as substrate for temperature sensing, and silicon carbide ceramic substrate for pressure sensor. The wireless interrogation system comprises a patch antenna sensor, a horn antenna, and a vector network analyzer that conducts frequency sweeps and signal measurements. The patch antenna's simplicity is advantageous because it is lightweight, has a low profile, and is also cost-effective to produce. To use it as a temperature and pressure sensor, an interrogating horn antenna is placed outside the furnace and directed towards the patch antenna. The sensor's resonant frequencies were designed to be around 5.75 GHz and 4.7 GHz for temperature and pressure, respectively. The interrogation frequency, which is close to the sensor's resonant frequency, enables the desired power transfer to the sensor because of the minimum impedance at its resonance. The operational frequency of the system is inversely proportional to the antenna size, meaning that as the frequency increases, the antenna size decreases. Therefore, using a higher operational frequency makes the patch antenna small enough to be comparable to the sensor's size. However, the patch antenna is

not as convenient when the operational frequency is lower, as this necessitates a larger antenna size. The effect of frequency on the size will be discussed in the later sections.

Fiber optical system is another example of wireless system that can be used in HE. Fiber optic technology is making noteworthy progress in its application for various air and space purposes, such as communication networks, navigation, and sensors [30]. These applications require integration into systems that must function in demanding environments with extreme conditions, including high and low temperatures, shock, vibration, radiation, corrosive settings, high levels of electromagnetic and radio-frequency interference, and pressure. Despite the numerous benefits associated with fiber optic systems, such as their resistance to electromagnetic interference, small size and weight, high bandwidth, and ease of upgrade, there are also some obstacles to their implementation. These obstacles include the high cost of installation, reliability concerns (performance over long periods of time), and difficulties associated with installation. However, the main drawback is the directivity and positioning of sensors. One of the primary necessities for an optical transmission system is that the transmitter and receiver must be aligned in a line of sight, which is not always feasible in harsh environments [30].

Another interesting technique explored for wireless interrogation in harsh environments is field coupling. Field coupling is a technique where both the interrogating antenna and the sensor antenna are in close proximity. When the available size of the antenna is too small with respect to the wavelength, the proximity of a metal ground plane, usually where sensing needs to be performed, can hinder the operation of a field coupling antenna, and also of radiating antennas. A downside of field coupling is that it has a limited interrogation distance, usually only a few centimeters in practice. In situations where the signal must be transmitted over longer distances and the antenna

is allowed to have a higher profile, the radiating signal solution is a better option. This approach allows for wireless interrogation over a longer range, typically several meters [1], [31]-[33].

A PIFA antenna system designed for harsh environments is another instance of an already existing interrogation antenna system [34]. One approach involves using the metallic object itself to construct the antenna, where an RFID tag is made by cutting a slot into a metallic foil. Several RFID tag antennas have been proposed for metallic objects, such as planar inverted-F antenna (PIFA), U slot, and inverted-F tag antenna [34]- [37]. However, slot antennas have the requirement that the object to be identified can be altered, and the RFID chip may be prone to physical damage if it is placed in the air between two metallic edges. The PIFA structure has demonstrated that it can occupy a relatively small area compared to the microstrip antenna. The paper [34] discusses a very small PIFA antenna that is made with circular geometry and is situated inside a metallic cup. The PIFA antenna was created for a frequency of 868 MHz, but it experiences greater loss compared to a larger antenna that operates around the same frequency. Figure 1.1 shows the PIFA antenna designed and discussed in [34]. Additionally, the narrowband structure of the PIFA poses challenges to its manufacturing, which is subject to strict limitations. This holds true for most electrically small antennas (as in antennas where the wavelength is very large compared to the dimensions of the antenna), as their bandwidth is highly susceptible to mechanical tolerances during the manufacturing process.

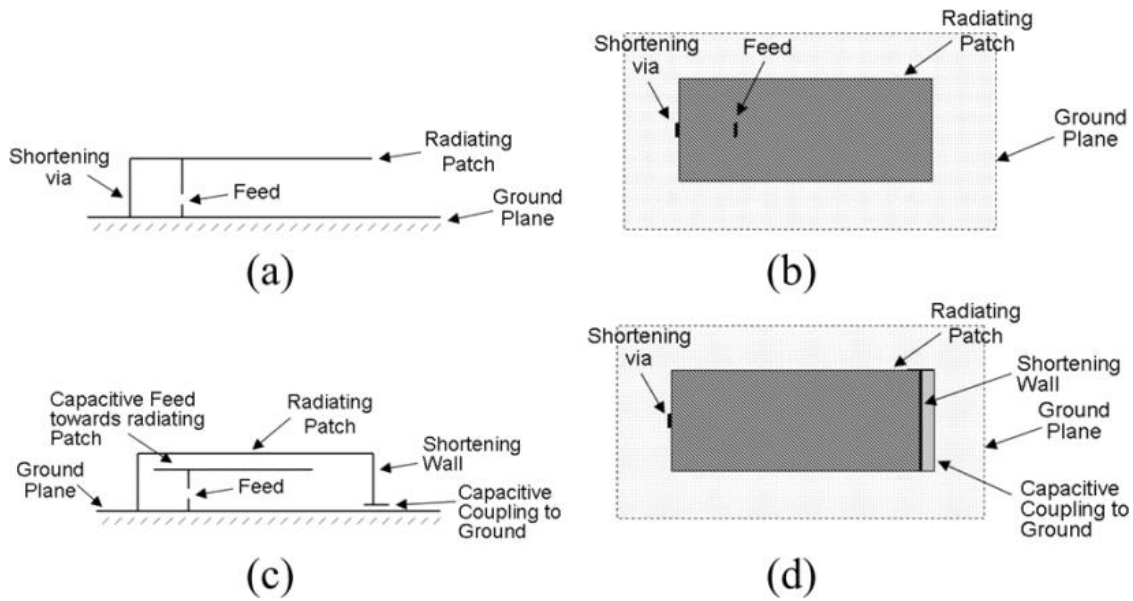


Figure 1.1: (a)-(b) The basic PIFA structure and (c)-(d) its electrically smaller version [34]

1.2 Antennas in HT / HE: Materials and Desired Design Characteristics

Antennas designed to operate at high temperatures typically require materials that can withstand extreme thermal stresses and maintain their mechanical and electrical properties over extended periods [38]. Some common materials used in high temperature antennas include:

Ceramics: High-temperature ceramics, such as aluminum oxide (Al_2O_3) (used up to around 1600°C), silicon carbide (SiC) (can withstand temperatures up to $1600\text{-}1700^\circ\text{C}$), and zirconia (ZrO_2) (stable up to approximately 2400°C), are widely used in high-temperature applications due to their high melting points and thermal stability. These ceramics also exhibit excellent electrical properties and low dielectric loss at high frequencies [39].

Metals: High-temperature metals, such as tungsten (W) (has a melting point of 3422°C , making it suitable for high temperatures), molybdenum (Mo) (melting point 2623°C), and tantalum (Ta) (melting point of 3290°C), and alloys, such as Inconel (depending on the grade can be used up to

1093°C) are commonly used in high-temperature antennas due to their high melting points, high strength, and good thermal conductivity. These metals are often used for antenna elements and support structures [40].

Composites: High-temperature composites, such as carbon-carbon (C-C) (depending on specific combination, can withstand temperatures up to 3000°C) and carbon-silicon carbide (C-SiC) (high temperature stability suitable for applications up to 1600°C or higher), are used in high-temperature antennas due to their high strength, low thermal expansion coefficient, and thermal stability. These composites are often used for structural components and antenna radomes [41].

Polymers: High-temperature polymers, such as polyimides (depending on the specific type, they can typically operate in the range of -50°C to 300°C), are used in high-temperature antennas due to their high thermal stability, low dielectric loss, and excellent mechanical properties. These polymers are often used as dielectric materials for antenna substrates and coatings [42].

The relationship between antenna size and dielectric at high temperatures is an important consideration in the design of antennas for high-temperature applications. Dielectric materials, which are commonly used to insulate and support the conductors of an antenna, can be subject to significant changes in their electrical properties at high temperatures. These changes can have a significant impact on the performance of the antenna, particularly with respect to its radiation efficiency and bandwidth. One important consideration in the design of high-temperature antennas is the selection of dielectric materials that can maintain their dielectric permittivity at high temperatures. Common dielectric materials used in antenna construction, such as ceramic and glass, have been shown to exhibit stable dielectric permittivity up to temperatures of around 500-600°C (932-1112°F) [43]. However, above these temperatures, these materials can experience

significant changes in dielectric constant and increased losses, which can degrade antenna performance [44].

Another important consideration in the design of high-temperature antennas is the size of the antenna itself. As antenna size increases, it can limit the usage of the antenna/sensor for reduced space applications and also poses higher demand on packaging. In addition, the amount of material used to construct the antenna also increases, which can impact the overall performance of the antenna at high temperatures. Several studies have investigated the impact of antenna size and dielectric properties on antenna performance at high temperatures. For example, a study explained in [43] examined the performance of a small planar inverted-F antenna (PIFA) constructed using various dielectric materials at temperatures up to 600°C. The study found that the performance of the antenna was impacted by the dielectric material used, with ceramic materials exhibiting the best performance at high temperatures. Another study by [44] investigated the impact of antenna size on the performance of a patch antenna constructed using a high-temperature ceramic dielectric material. The study found that as the size of the antenna increased, the smaller frequencies bandwidth of the antenna decreased, due to an increase in dielectric losses associated with the increased amount of ceramic material used in the construction of the antenna.

The selection of dielectric materials that can maintain low losses, reduced dielectric dielectric constant variation at high temperatures is crucial, and the size of the antenna can impact the overall performance of the antenna at high temperatures. Hence, air is a convenient dielectric, due to reduced increase in loss and reduced variation of the dielectric permittivity with temperature.

1.2.1 Air as Dielectric for HT antennas

High temperature antennas with air as the dielectric material are commonly used in high-temperature applications due to their low dielectric loss, high power handling capacity, ease of

fabrication and most importantly the reduced change in the antenna response with temperature, since $\epsilon_r = 1$ under HT conditions. The use of air as the dielectric also reduces the overall weight and cost of the antenna. The antenna's dimensions and the spacing between the elements must be carefully designed to ensure that the antenna operates at the desired frequency and with the desired radiation pattern [45]-[47]. Antennas with air as a dielectric are usually larger when compared to antennas that use high-permittivity dielectric materials, because the size of an antenna is inversely proportional to the square root of the permittivity of the material.

A simple air-cooled broadband antenna that can operate at temperatures up to 700°C is discussed in [48]. The antenna consists of a series of parallel wires separated by air gaps, which act as the dielectric material.

The design and development of an air-dielectric patch antenna that can operate at temperatures up to 600°C is presented in [49]. The antenna is made of a copper patch on a quartz substrate with an air gap between the patch and the ground plane.

The design of a low-profile air-filled dielectric resonator antenna that can operate at temperatures up to 900°C is discussed in [50]. The antenna consists of a cylindrical dielectric resonator filled with air and a feeding structure made of a coaxial cable.

This work focuses on design and implementation of one type of antenna that uses air as dielectric and which is relatively compact, the normal mode helical antenna.

1.3 Antenna Theory Terminology

Antenna theory is a complex field that deals with the design, analysis, and performance of antennas. Understanding the terminology associated with antenna theory is critical to developing

a comprehensive understanding of how antennas work. The terminology qualitatively introduced next comes from [22],[51],[52].

1. Radiation pattern: The graphical representation of the directional properties of an antenna's radiated electromagnetic field.
2. Directivity: The measure of an antenna's ability to concentrate radiation in a specific direction.
3. Gain: The ratio of the power density radiated by an antenna in a particular direction to the power density radiated by a hypothetical isotropic antenna.
4. Polarization: The type of orientation of the electric field vector in an electromagnetic wave radiated by an antenna.
5. Frequency: The number of cycles per second of an electromagnetic wave.
6. Bandwidth: The range of frequencies over which an antenna operates effectively.
7. Standing wave ratio (SWR): The ratio of the maximum voltage to the minimum voltage along a transmission line, caused by reflections from an antenna.
8. Radiation intensity: The power radiated by an antenna per unit solid angle is called the radiation intensity.
9. Efficiency: Antenna efficiency is a measure of how effectively an antenna converts the input electrical power into radiated electromagnetic waves. It quantifies how much of the input power is actually radiated as electromagnetic energy, and it is expressed as a percentage. An efficient antenna minimizes losses and maximizes radiation, ensuring that most of the input power is transformed into radiation rather than being dissipated as heat or lost in other ways [51].

Mathematically, antenna efficiency (η) is defined as:

$$\text{Efficiency } (\eta) = \frac{\text{Radiated power}}{\text{input power}} \times 100\%$$

where,

Radiated power: the power radiated by antenna in desired direction.

Input power: The electrical power supplied to the antenna at its input terminals.

The relationship between the frequency of an electromagnetic wave and the size of an antenna is a fundamental concept in antenna theory. For most high performance, antennas their size are proportional to the wavelength of the electromagnetic wave that it is designed to transmit or receive [22].

At low frequencies, antennas need to be physically large to efficiently radiate or receive a signal, while at high frequencies, antennas can be much smaller. For example, a dipole antenna designed for a frequency of 1 MHz in air would be approximately 15 meters long, while a dipole designed for a frequency of 1 GHz would only be 15 cm long. This relationship can be explained by the fact that the size of an antenna needs to be on the order of one-half wavelength to be efficient. This is known as the resonant length of the antenna. This size dependency is related to the fact that a resonating antenna is most efficient when its physical dimensions correspond to half wavelength (or a quarter wavelength in case of a monopole or PIFA antennas). When an antenna is resonant, it has the maximum possible radiation efficiency for a given size. However, designing an antenna to operate around a certain bandwidth requires the consideration of the targeted or allowed antenna size, bandwidth, and directivity. Antennas designed for narrowband operation around their resonant frequency have sizes comparable to the wavelength, while antennas designed for wideband operation can be smaller but have lower efficiency [22], [51].

1.4 Far field, Near Field and Field Coupled Antennas

An important parameter to be considered for a certain wireless system application is the expected distance of operation between the transmitting and the receiving antennas to allow for the data be detected above noise level. The distance between transmission and reception is divided into three regions: reactive near field, radiative near field, and far field. The limiting distances are the Far Field distance (R_{FF}) and the Radiating Near Field distance (R_{NF}) shown in **Error! Reference source not found.**

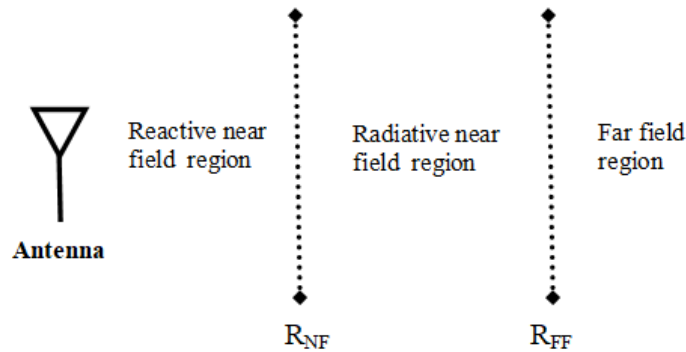


Figure 1.2: Near and far field regions of an antenna

1.4.1 Far Field Antennas

Far-field antennas are those meant to radiate electromagnetic waves at a distance that is much greater than the size of the antenna and the wavelength of the transmitted signal. The far-field region is also called the radiation field or Fraunhofer region. The power density of the electromagnetic waves follows the inverse square law, meaning the intensity of the waves decreases with the square of the distance from the antenna. The lower limit for Far-field distance is given by [22],

$$R_{FF} = \frac{2D^2}{\lambda} \quad (1.1)$$

where D is the largest dimension of the antenna and λ is the wavelength.

Far-field antennas are typically used in applications such as broadcasting, satellite communication, and long-range communication systems [22],[51].

1.4.2 Near Field Antennas:

The electromagnetic waves in this region do not have the spherical wavefronts seen in the far-field. Instead, they have complex patterns that depend on the antenna's geometry and the distance from the antenna. Near-field antennas are typically used in applications such as RFID, wireless power transfer, and medical imaging. Near field is divided into two regions: radiating near field and reactive near field .

1.4.2.1 Radiating near field

Radiating near field is also called Fresnel region. The lower limit for radiating near field distance is given by [22],

$$R_{NF} = 0.62 \sqrt{\frac{D^3}{\lambda}} \quad (1.2)$$

where D is the largest dimension of the antenna and λ is the wavelength.

1.4.2.2 Reactive near field

Field-coupled antennas are those antennas where the distance between the antenna and the target is much smaller than the wavelength of the transmitted signal. This field is also called reactive near field region. An example of this application is the HE wireless interrogation through inductive

coupling between the interrogating and sensor antennas for dynamic strain measurement in HT/HE uses SAWR as discussed in [7], which consists of coils coupled through magnetic field. In this application, the interrogating antenna was suspended approximately 5 mm above the SAWR and sensor antenna. Other applications are: power coupling to charge batteries and consumer appliances.

1.5 Helical Antenna

A helical antenna consists of one or more conducting wires wound in the shape of a helix (Figure 1.3) [53]. A helical antenna with one conducting wire is the most common type. There are two operational modes for helical antennas: Axial Mode Helical Antenna (AMHA) and Normal Mode Helical Antenna (NMHA) [53]. The pitch and diameter of a NMHA are very small compared to the wavelength whereas the pitch and diameter of an AMHA are comparable to the wavelength [53]. A NMHA is omnidirectional whereas an AMHA is directional radiating a beam off the ends of the helix. AMHA is widely used for satellite communications [53]. NMHA antenna applications include Radio Frequency Identification (RFID) tags, Tire Pressure Monitoring Systems (TPMS), and smart keys [54]-[75].

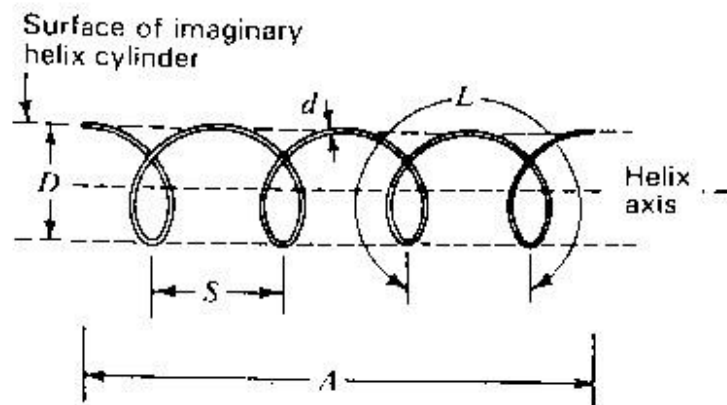


Figure 1.3: Geometry of helix [53]

1.5.1 Helix Geometry

A helix is a geometric combination of straight line, circle and a cylinder. Helix can be either left or right-handed. The symbols used to describe the helix in Figure 1.4 are as follows [53]:

D_h = diameter of the helix measured between the centers of the wire

C = circumference of each loop (πD_h)

R_h = radius of the helix ($\frac{D_h}{2}$)

S = spacing between the turns measured between centers of the wire

α = pitch angle ($\tan^{-1} \frac{S}{C}$)

L = length of one loop ($\sqrt{C^2 + S^2}$)

N = number of turns/loops

H = total height of the helix

d = diameter of the conductor wire

r = radius of the conductor wire ($\frac{d}{2}$)

h = length of the wire between the end of coaxial line and the beginning of helix

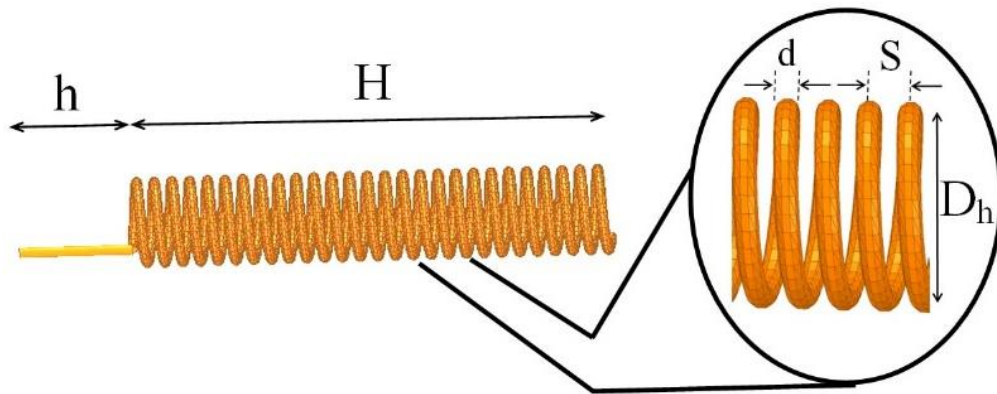


Figure 1.4: Geometry and dimensions of a helix

If one turn of a circular helix is unrolled on a flat plane, the relationship between the spacing S , circumference C , turn length L and pitch angle α are as illustrated by the triangle in Figure 1.5 [53].

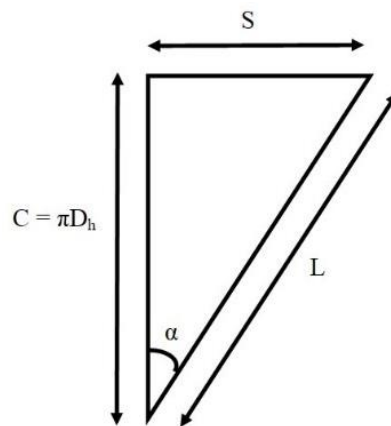


Figure 1.5: Relationship between C , S , L and α of a helix [53].

The relationship between the helix dimensions and the modes excited are depicted in Figure 1.6 using the diameter-spacing chart [53]. The rectangular coordinates of the helix's dimensions is expressed using the spacing ($S_\lambda = S/\lambda$) and the circumference ($C_\lambda = C/\lambda$) as cartesian axes, while the polar coordinates is expressed using the length of one turn ($L_\lambda = L/\lambda$) as amplitude and the pitch angle α . If the spacing is zero, the helix becomes a loop with $\alpha = 0$ and if the diameter is zero,

the helix becomes a linear conductor with $\alpha = 90^\circ$. As a function of frequency, the helix moves along a line of constant pitch angle. Therefore, in Figure 1.6, the abscissa axis represents linear conductors, and the ordinate axis represents loops, with the general case of the helix represented by the entire area between the two axes.

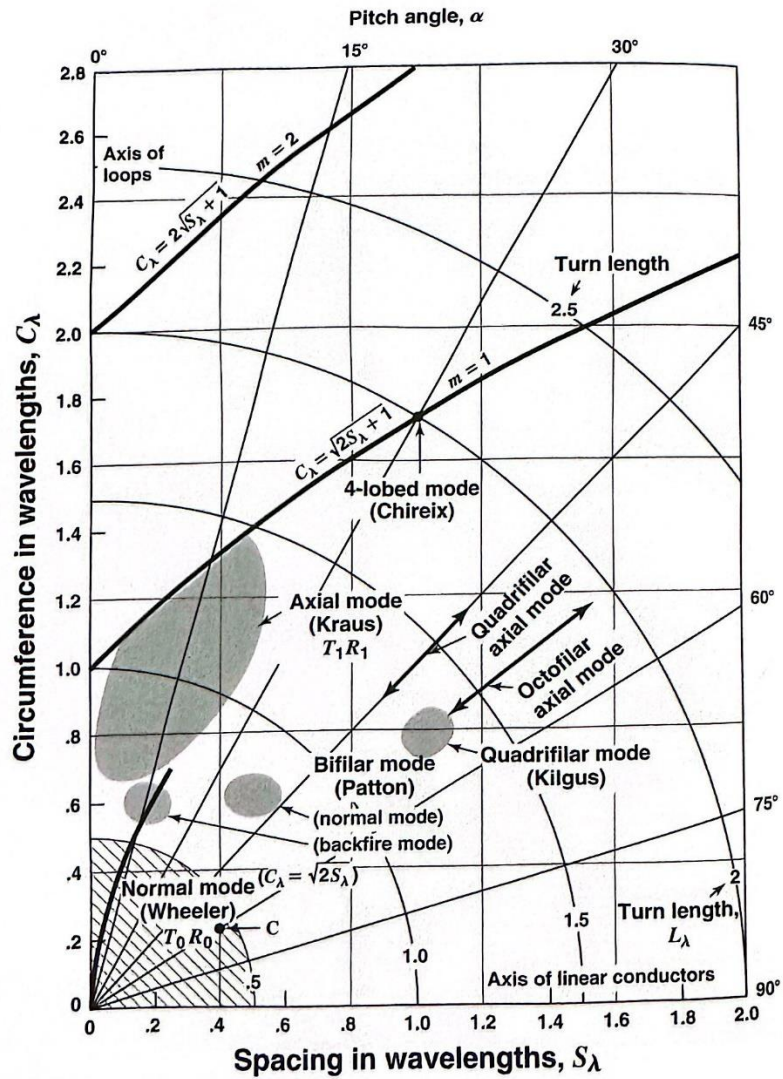


Figure 1.6: Helix chart showing the location of different modes of operation as a function of helix dimensions [53].

1.5.2 Transmission and Radiation Modes of Monofilar Helices

As discussed by Krauss [53], “transmission mode” is used to describe the way in which an electromagnetic wave propagates along an infinite helix as though the helix constitutes an infinite transmission line or waveguide. And “radiation mode” is used to describe the general form of the far-field pattern of a finite helical antenna.

Although many modes are possible, two kinds are of particular interest. One is axial mode of radiation (R_1 mode) and the other is normal mode of radiation (R_0 mode).

The lowest transmission mode for a helix has adjacent regions of positive and negative charges separated by many turns. This mode is designed as T_0 transmission mode. The T_0 mode is important when length of 1 turn of the helix is very small compared to the wavelength. It is important transmission mode in the travelling wave tube [53]. Since the adjacent regions of positive and negative charges are separated by an appreciable axial distance, a substantial axial component of the electric field is present and in travelling wave tube this field interacts with the electron stream. If the criterion $L_\lambda < 1/3$ is arbitrarily selected as a boundary for the T_0 transmission mode, the region of helix dimensions for which this mode is important is within T_0R_0 area marked in Figure 1.6 [53].

A helix excited in the T_0 transmission mode may radiate. Considering a very short helix ($nL \ll \lambda$), current is assumed to be of uniform magnitude and in phase along the entire helix. The maximum field from the helix is normal to the helix axis for all helix dimensions provided only that $nL \ll \lambda$. This condition is called normal radiation mode (R_0). The transmission mode and radiation mode

appropriate for very small helices can be described by combining the T_0 and R_0 designations as T_0R_0 as shown in Figure 1.6 [53].

A first order transmission mode on the helix, designated T_1 , is possible when the helix circumference is of the order 1λ . For small pitch angles, this mode has regions of adjacent positive and negative charge separated by approximately half turn (or near the opposite ends of a diameter). It is found that radiation from helices with circumferences of the order of 1λ and a number of turns ($n > 1$) is a well-defined beam with a maximum in the direction of the helix axis. Hence, this type of operation is called the axial mode of radiation with designation R_1 . The monofilar axial mode of radiation occurs over a range of dimensions as indicated by T_1R_1 area in Figure 1.6. Higher-order transmission modes T_2 , T_3 and so forth are permissible for higher values of C_λ .

The antenna that will be discussed in this work is meant to operate in VHF and UHF frequency range and operate in the T_0R_0 normal mode. In this frequency range, the dimensions of a conventional VHF and UHF antenna comparable to the wavelength are undesirably big for the targeted reduced size sensor applications, such as a SAW sensor [74]. Hence, the need to design a more compact antenna working in VHF and UHF frequency range.

1.6 Goals and Scope

As has been noted in previous sections, antenna interrogating system operating in high temperatures and harsh environments where rapid temperature fluctuations and compact spaces with packed metal surface conditions are encountered in a wide range of applications including industrial setups like turbines, heat pumps and boilers. The reliability of the sensor system employed in these applications depends on the communication/ interrogation system employed. The goal of this thesis is to design, fabricate and test a compact antenna system structure working

in the VHF and UHF frequency range which can be used for future integration with SAW sensor system and for operation in harsh environments.

The scope of this thesis focuses on addressing the following objectives:

- Design a normal mode helical antenna operating around frequency range of 300 MHz, which is the frequency that HE SAW devices have been fabricated at Umaine, and simulating the structure design on different computational software platforms including ANSYS-HFSS and WIPL-D Pro.
- Analyze the antenna structure dependence on the nearby ground plane implemented through the use of microstrip access lines of different lengths.
- Reduce the effect of coaxial cable connected to the structure by introducing a balun and thus measure the antenna impedance.
- Create a network model for the balun structure fabricated with the assistance of the Keysight ADS software.
- Measure the transmission loss of a two-antenna system over different distances to validate the usefulness of the structure for sensor interrogation in mid-range close environments.

1.7 Thesis Organization

To address the topics and report the findings in this thesis, the chapters are organized in the following manner:

- Chapter 2 presents an overview of NMHA operation according to the theoretical background available. The chapter also details the structure under study with different microstrip line sizes.

- Chapter 3 discusses the simulation of the antenna structure on different computational software platforms including ANSYS-HFSS and WIP-D Pro. In addition, this chapter also discusses the structure sensitivity to change in different parametric values.
- Chapter 4 introduces the balun connected to the structure and also calculates the equivalent circuit model for the balun structure using Keysight ADS.
- Chapter 5 reports the measurements of the implemented NMHA. The NMHAs were characterized both in laboratory environments using a dedicated setup in the Microwave Engineering Laboratory and in the Anechoic Chamber available at Umaine.
- Chapter 6 concludes the work done in this thesis and discusses potential future work.

CHAPTER 2. NORMAL MODE HELICAL ANTENNA DESIGN AND IMPLEMENTATION

This chapter outlines and discusses the operation of a Normal Mode Helical Antenna. The chapter addresses the existence of limited theoretical background on the operation of a Normal Mode Helical Antenna. It also discusses the effects of connecting an NMHA coil structure at the end of a coaxial cable and its lack of radiation without the presence of a ground plane. The chapter discusses the effect of connecting different microstrip lines to the NMHA, which serves the role of a ground plane to the NMHA.

2.1 Theory of Normal Mode Helical Antenna

In Chapter 1 the basic model and characteristics of an axial-mode helical antenna with maximum radiation along the helix axis was introduced. In this section normal mode helical antenna is discussed whose radiation is maximum normal to direction of helix axis.

The helix circumference is much smaller in comparison to the wavelength at frequency of operation in case of normal mode radiation. When the circumference is about a wavelength, the axial mode of radiation is prevalent, but when the circumference is much smaller the normal mode is dominant. Figure 2.1 shows helices radiating in axial mode, normal mode, and 4-lobed mode with their relative sizes for generating the corresponding modes.

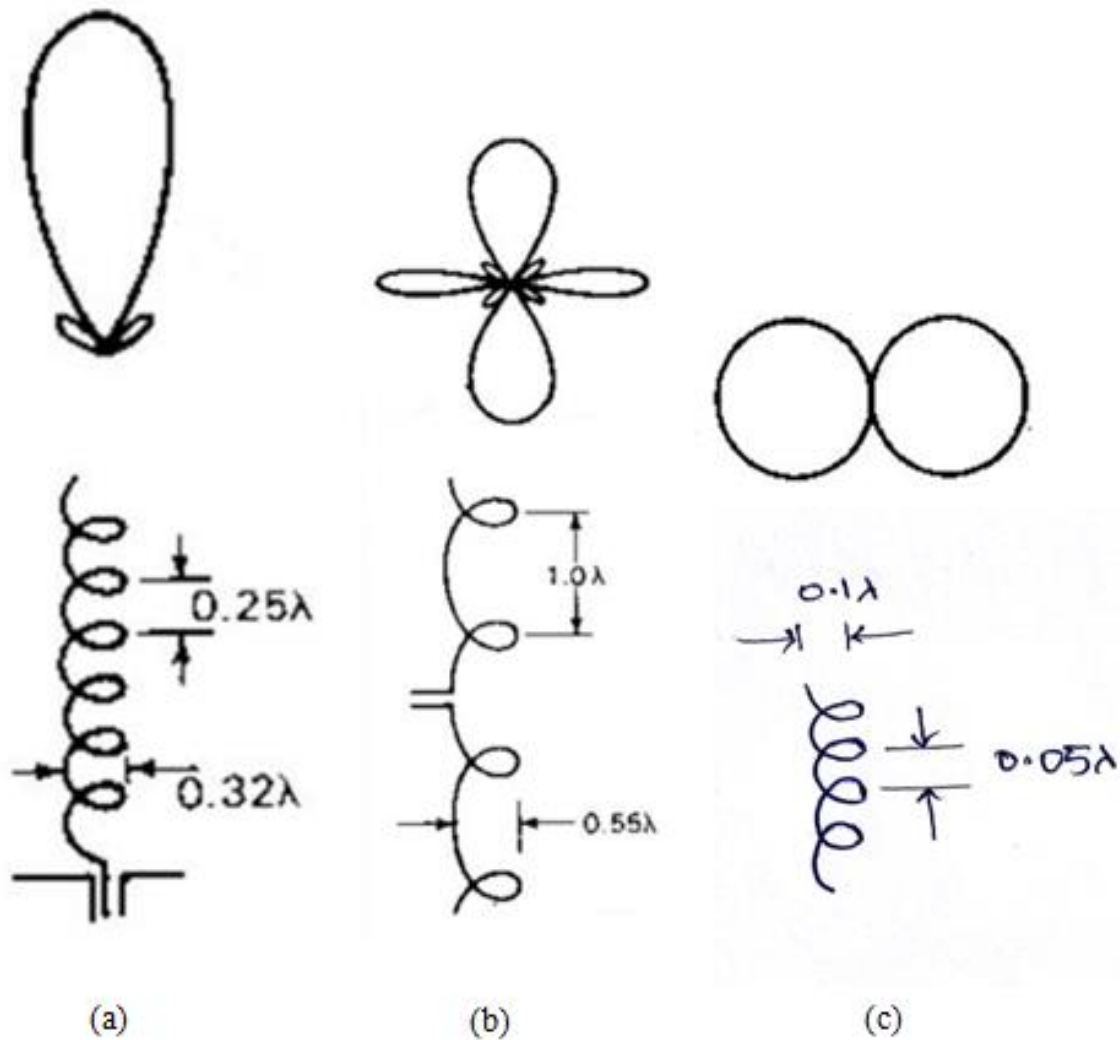
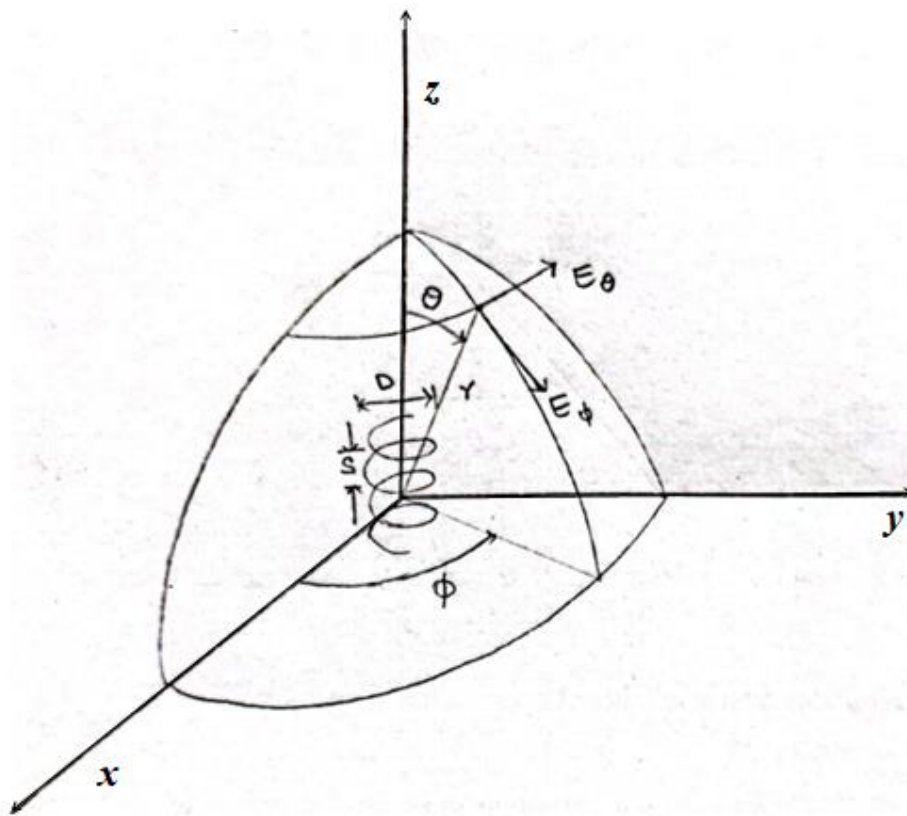


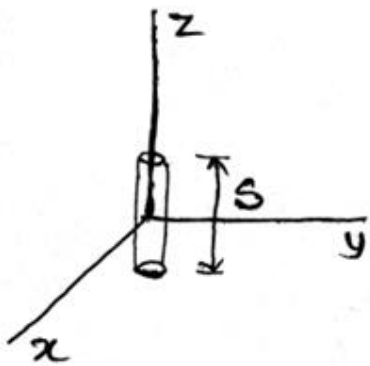
Figure 2.1: Field patterns along with relative size indicated of: (a.) axial; (b.) 4-lobed ; (c) normal mode helical antennas [53].

Figure 2.2a shows a helix with its axis oriented along the z-axis with r, θ, ϕ being the spherical coordinates. The dimensions are small ($nL \ll \lambda$), hence the antenna operates in normal mode with the radiation in the XY-plane with zero field in the direction of helix axis (z-direction in this case).

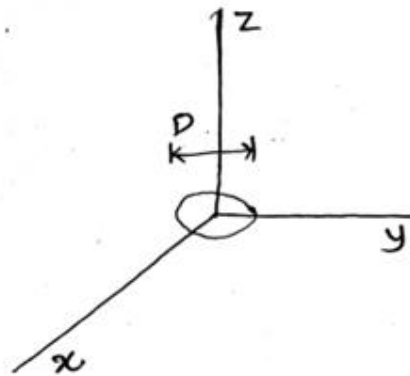
When the pitch angle of the helix is zero, the helix becomes a loop as shown in Figure 2.2b and when the pitch angle is 90° , the helix becomes a dipole antenna as shown in Figure 2.2c. These two are the limiting conditions of the helix structure.



(a)



(b)



(c)

Figure 2.2: Dimensions for: (a.) helix; (b.) loop; (c.) dipole [53].

The far-field radiation of the helical structure has two main components E_θ and E_ϕ as shown in Figure 2.2a. Next expressions for far-field patterns of these components for the case of a short helix are mentioned. This can be done by modifying the structure of helix as a combination of

small loops and short dipoles connected in series as shown in Figure 2.3a. The diameter D of the loop is same as the diameter of helix and the length of short dipole is same as the height of the helix as shown in Figure 2.2. As the helix in consideration is small, the structure shown in Figure 2.2a can be equivalent to the structure shown in Figure 2.3a. Since the height of the helix is small compared to the wavelength the current is assumed to be of uniform magnitude and phase over the entire length of the helix and the far-field pattern is independent of the number of turns. Therefore, it is sufficient to calculate the far-field pattern of a single small loop and short dipole as indicated in Figure 2.3b.

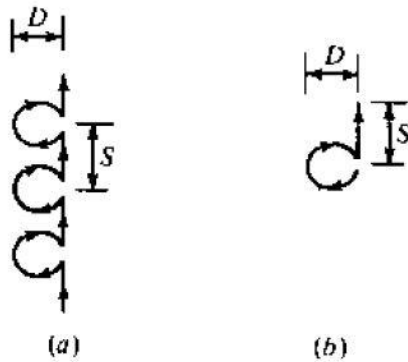


Figure 2.3: Modified helix for normal-mode calculations [53].

The far-field of a small loop has only one component which is E_ϕ . Its value is given by [53]

$$E_\phi = \frac{120\pi^2 [I] \sin \theta}{r} \frac{A}{\lambda^2} \quad (2.1)$$

where the area of the loop is given as $A = \pi D^2/4$ and I is the current in the helix.

The far-field of a short dipole has only E_θ component. Its value is given by [53]

$$E_{\theta} = j \frac{60\pi[I] \sin \theta}{r} \frac{S}{\lambda} \quad (2.2)$$

where S is replacing L as the length of the dipole.

By comparing Equations 2.1 and 2.2, the absence of j term in E_{ϕ} suggests that E_{θ} and E_{ϕ} are in phase quadrature. The ratio of magnitudes of E_{θ} and E_{ϕ} gives the axial ratio of polarization ellipse of the far field [53].

$$AR = \frac{|E_{\theta}|}{|E_{\phi}|} = \frac{S\lambda}{2\pi A} = \frac{2S\lambda}{\pi^2 D^2} = \frac{2S\lambda}{C_{\lambda}^2} \quad (2.3)$$

Based on the axial ratio of polarization ellipse, there are three special cases:

1. When $E_{\phi}=0$, the axial ratio is infinite indicating linear vertical polarization. The helix is a vertical dipole in this case.
2. When $E_{\theta}=0$, the axial ratio is 0 indicating linear horizontal polarization. The helix is horizontal loop in this case.
3. When $E_{\theta}=E_{\phi}$, the axial ratio is unity indicating circular polarization. Substituting $AR=1$ in equation 2.3 yields [58]

$$\pi D = \sqrt{2S\lambda} \text{ or } C_{\lambda} = \sqrt{2S\lambda} \quad (2.4)$$

The radiation is circularly polarized in all directions with zero field in the direction of axis which is z-direction (Figure 2.2a). Figure 2.4 shows a resonant, narrowband, monofilar normal-mode helical antenna which fulfills the condition in Equation 2.4.

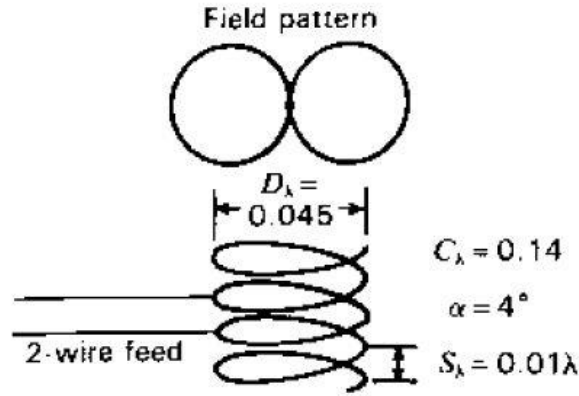


Figure 2.4: Resonant narrowband circularly polarized monofilar normal-mode coil, pattern is that of a short dipole [53].

The three main cases of polarization ellipse were discussed briefly concerning linear and circular polarization. In a more general case, the radiation is elliptically polarized. Hence, the radiation pattern of a constant turn-length helix changes gradually with respect to the pitch angle α . When $\alpha=0$, the helix forms a loop (Figure 2.2b) and has horizontal polarization which is linear. As α increases, the polarization turns into elliptical with the major axis horizontal. When α reaches a value where $AR=1$ ($C_\lambda = \sqrt{2S_\lambda}$), the polarization is circular. The value of α is given by [53]

$$\alpha = \sin^{-1} \frac{-1 + \sqrt{1 + L_\lambda^2}}{L_\lambda} \quad (2.5)$$

As α increases further, the polarization becomes elliptical with the major axis being vertical. When α reaches 90° , the polarization is linear and vertical with the helix turning into a short dipole.

In the discussion about normal-mode radiation, the assumption made is that the current is uniform over the length of helix in both magnitude and phase. This condition can only be approximated if the length of the helix is very small compared to the wavelength and is end-loaded. The bandwidth

for such a small helix antenna is very narrow, and the radiation efficiency is low. Both can be increased by increasing the size of the helix, but this compromises the assumption of constant current throughout the length of the helix. To avoid that, some type of phase shifters is to be placed at regular intervals. This is one of the major limitations to form normal-mode radiation from a helix.

Resonant monofilar normal-mode helical antennas can be used as short, vertically polarized radiators. Figure 2.5 illustrates a helix of height 0.06λ mounted on ground plane with vertical axis is a narrowband substitute for $\lambda/4$ monopole above a ground plane. From Equation 2.3, the axial ratio is calculated to be [53]

$$AR = \frac{2S_\lambda}{C_\lambda^2} = \frac{2 \times 0.01}{(0.04)^2} = 12.5 \quad (2.6)$$

The major axis of polarization ellipse is mostly vertical. The radiation resistance is same as that of a short monopole of height $h_\lambda (=h/\lambda)$ above the ground plane where $h_\lambda = nS_\lambda$, which is given by [53]

$$R_s = \frac{1}{2} \times 790 \left(\frac{I_{av}}{I_o} \right)^2 h_\lambda^2 \quad (\Omega) \quad (2.7)$$

Where I_{av} = amplitude of average current on dipole (peak value in time),

I_o = amplitude of terminal current of center-fed dipole (peak value in time)

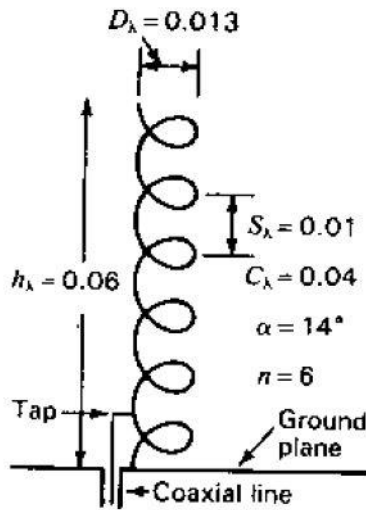


Figure 2.5: Resonant monofilar normal mode helical antenna mounted over a ground plane as substitute for $\lambda/4$ stub [53].

Assuming a sinusoidal current distribution radiation resistance is calculated to be 0.6Ω . This is the radiation resistance between the ground plane and the base of the helix. For the antenna to be connected to a coaxial line, the antenna impedance can be matched to 50Ω by tapping into the helix at a point further away from the ground plane (Figure 2.5), where one can obtain values of input impedance that ease the matching. The advantage of a helix over a straight stub is that the inductance of helix can resonate the antenna.

2.2 NMHA Structure Design Implemented in this work

As discussed in the earlier section, the size of a normal mode helical antenna is much smaller compared to the wavelength at frequency of operation. Initially a normal mode helical antenna was designed and fabricated to replicate a helical antenna connected to a circuit board in car smart key operating at frequency of 433MHz. Figure 2.6 shows an example of a car smart key utilizing a normal mode helical antenna connected to a circuit board.



Figure 2.6: A car smart key with normal mode helical antenna connected to the circuit board.

In this work a normal mode helical antenna is designed from extrapolating the parameter values of a helix to work around the frequency range of 300 MHz from a similar normal mode helical antenna connected to a circuit board as shown in Figure 2.6 working around 433MHz.

The theory discussed in this chapter described a conventional normal mode helical antenna but doesn't explain the helical antenna shown in Figure 2.6 which is basis for the helical antenna structure used in this work. An application notes by RF Monolithics [76] discusses the gain of the antenna structure shown in Figure 2.6. As discussed in [76], the orientation of the helical structure with respect to the PCB/ground plane affects the gain of the antenna.

2.3 NMHA Structure Notation

Figure 2.7 shows the structure analyzed in this work and labels the design dimensions involved: width of the microstrip line (w_p), width of the substrate (w_s), width of the wire (d), length of wire connecting the helix and the microstrip line (h), diameter of the helix measured from the center of the wire (D_h), pitch of the helix (S), number of turns (N), and length of the substrate/length of the

microstrip line (l_s). The other side of the substrate shown in Figure 2.7 has the microstrip line ground plane. The antenna structure implemented in this work is hereby referred to as Normal Mode Helical Antenna Structure (NMHAS) which is a combination of a helical structure connected to a microstrip line as shown in Figure 2.7.

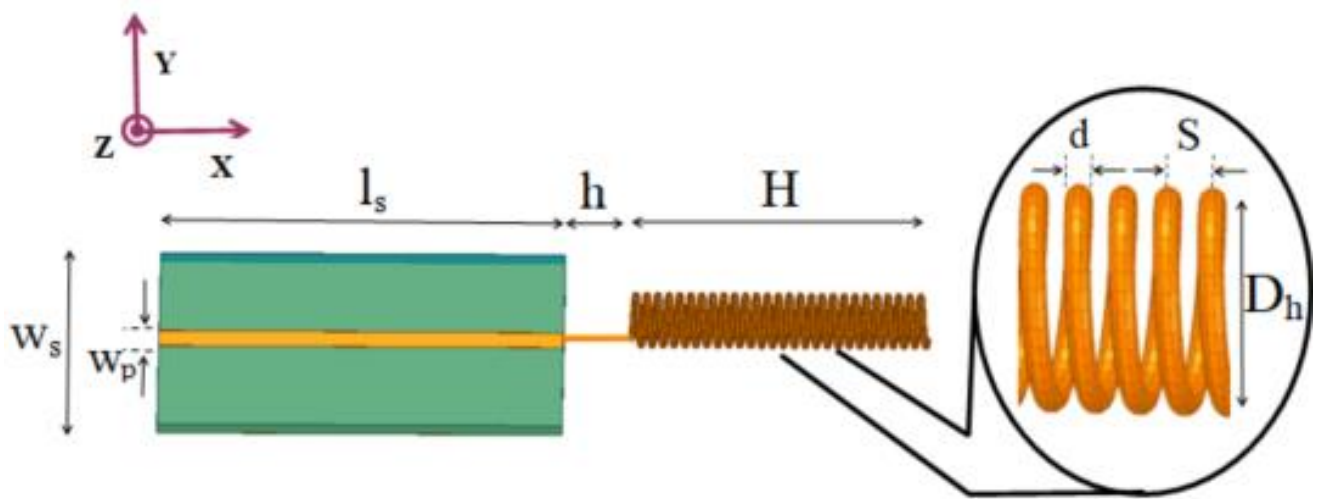


Figure 2.7: Geometry of NMHAS.

The microstrip line utilized FR-4 substrate with dielectric constant 4.4 and thickness of 1.5 mm; 0.02 loss tangent; and 35 μ m copper layers on both sides. The width of the microstrip line, w_p , was calculated for a 50 Ω line considering the chosen substrate; w_s was selected to be over 10 times w_p ; and l_s was selected after some experiments with different dimension, as discussed later in this section. A 20 AWG copper wire (diameter: d) with insulating coating was selected to provide reasonable rigidity to the helical structure fabricated and tested, and h was chosen to allow bending of the helical structure relative to the plane of the microstrip line, as discussed later in this section. A 1/4-20 thread screw (meaning the diameter of the screw is 1/4 inch and there are 20 turns per inch) was used for winding the helix. The Normal Mode Helical Antenna Structure (NMHAS) resonance condition can be adjusted mainly by changing D_h , S , N , w_s , and l_s . The dimensions D_h

(<0.1 λ , with λ being the wavelength, for an NMHAS), S, and N were selected as a compromise between small dimensions and $\text{Re}(Z_{\text{NMHAS}})$ as close to 50Ω as possible to facilitate future NMHAS matching. The values for the dimensions defined and discussed above are shown in table 1. Since the antenna was designed to operate around 300MHz, $\lambda = \frac{c}{f} = 1 \text{ m}$.

W_p [mm]	w_s [mm]	l_s [mm]	d [mm]	h [mm]	D_h [mm]	S [mm]	N
2.58	32	50.8	0.8	8.7	6.2	0.57	27

Table 2.1: Dimensions of the NMHAS

2.4 Direct Connection at the End of the Coaxial Cable

Initially the helical structure was directly connected at the end of a coaxial cable to measure the response of the antenna using a Vector Network Analyzer (VNA). The response of the antenna was observed to change drastically with the slightest variation in position of the coaxial cable or change in the environment around the coaxial cable or the helical antenna. This change in response is attributed to the current flow on the outer conductor of the coaxial cable connecting the antenna to VNA. This is due to the presence of a electrically small ground plane and thus strong interaction with the outer sheath of the coaxial cable. Figure 2.8 shows the helical antenna connected to an SMA connector. The outer conductor of the SMA connector acts as the electrically small ground plane for the helical antenna.

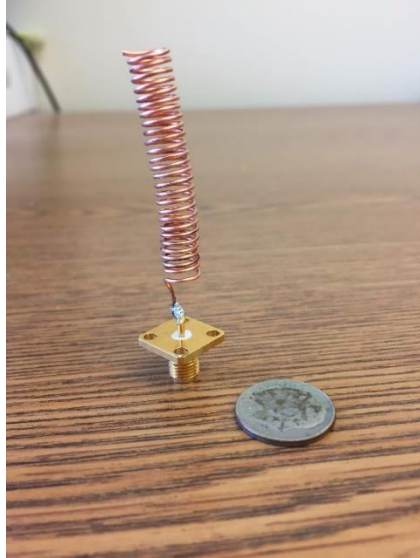
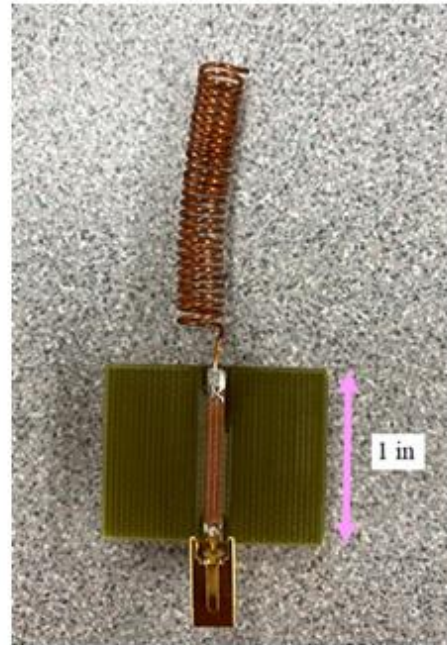


Figure 2.8: Helical antenna connected to a SMA connector.

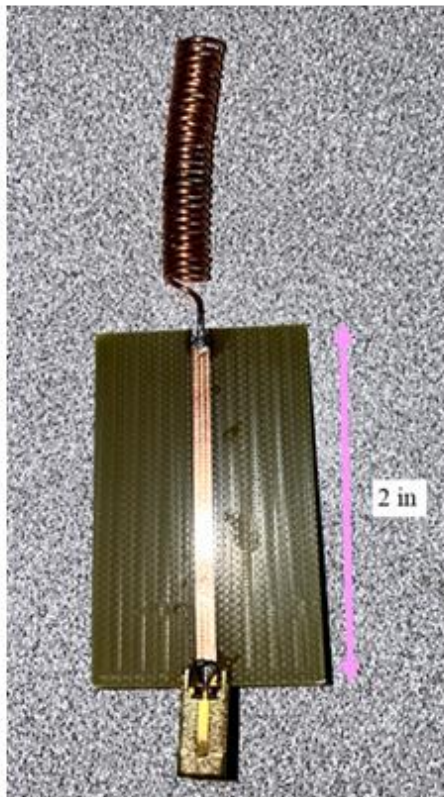
Hence to study the effect of ground plane on the helical structure, 4 different lengths of microstrip structures have been considered to connect to the helical structure “0.5 in, 1 in, 2 in and 3 in”. all these microstrip plates were 32 mm wide. Figure 2.9 shows the 4 different microstrip structures connected to the helical structure fabricated to operate around 300MHz. The response of the antenna with respect to the microstrip lines is discussed later in chapter 3 and 4.



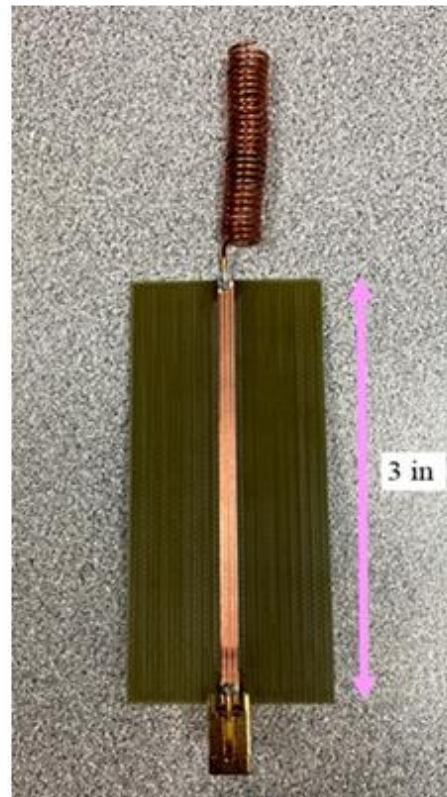
(a)



(b)



(c)



(d)

Figure 2.9: Four different microstrip structures connected to helical structure.

To reduce the current flowing on the outer conductor of the coaxial cable, a balun was introduced between the input of the microstrip line and the SMA connector. The importance of a balun is to connect an unbalanced coaxial cable to the unbalanced antenna structure. Although the microstrip is an unbalanced line, the ground plane of the microstrip integrated with the helix makes the NMHAS antenna, which is treated as a balanced structure. The balun implemented is further discussed in Chapter 4.

2.5 Conclusions

This chapter discussed the existing theory of Normal Mode Helical Antenna described by Krauss in [58]. The chapter defines the notation used in later chapters and which is somewhat different and complementary from that used in [53]. The connection of helical structure directly to an SMA connector was discussed and it was observed that the current was flowing on the outer sheath of the coaxial cable, since touching or changing the conducting environment around the coaxial accessing the structure significantly change the antenna impedance response. Microstrip lines of different sizes were introduced to connect the helix and to study the effect of size of the ground plane. A balun was introduced to mitigate the current flowing on the outer conductor of the coaxial cable which will be further discussed in detail in Chapter 4.

CHAPTER 3. NMHAS SIMULATIONS

In this chapter two commercially available software platforms are used to simulate the NMHAS and determine its S-parameter responses on a $50\ \Omega$ system. These software platforms are WIPL-D Pro V17 (WIPL-D, Serbia), which utilizes method of moments (MoM) techniques and HFSS v21 (ANSYS, USA), which relies on finite element method (FEM) analysis. The simulation responses of the NMHAS on these platforms is discussed in Section 3.1 and Section 3.2. Furthermore, a comparison of the structure's response on these different platforms is presented in Section 3.3, while Section 3.4 delves into the sensitivity of the NMHAS frequency response to various structural parameters using WIPL-D.

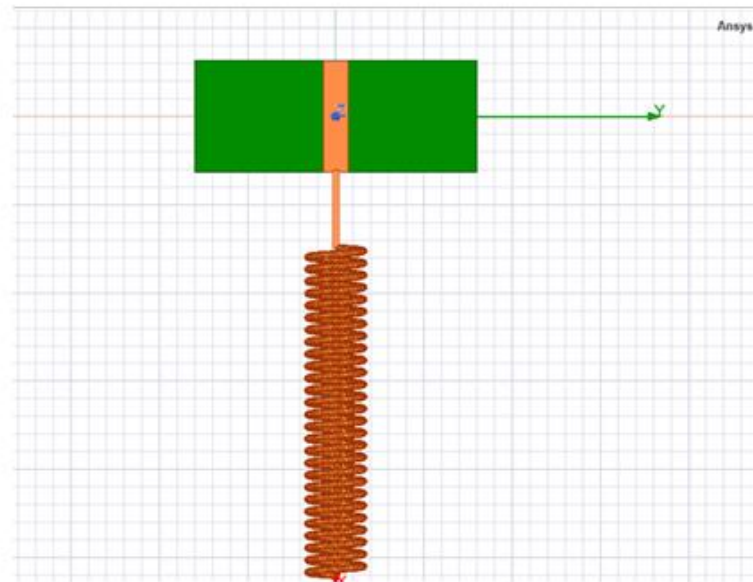
3.1 Simulation of NMHAS on HFSS

As discussed in Section 2.5, helical structure is connected to microstrip lines of varying lengths. Specifically, the helix structure is sequentially connected to four different microstrip lines measuring 0.5", 1", 2", and 3". In each of the subsections, simulation results are presented for NMHAS employing microstrips with the different lengths mentioned above. For simulation purposes in HFSS, a rectangular radiation box with dimensions of $25\text{cm} \times 25\text{cm} \times 30\text{cm}$ is utilized and FR-4 substrate properties mentioned in Section 2.3 are assumed.

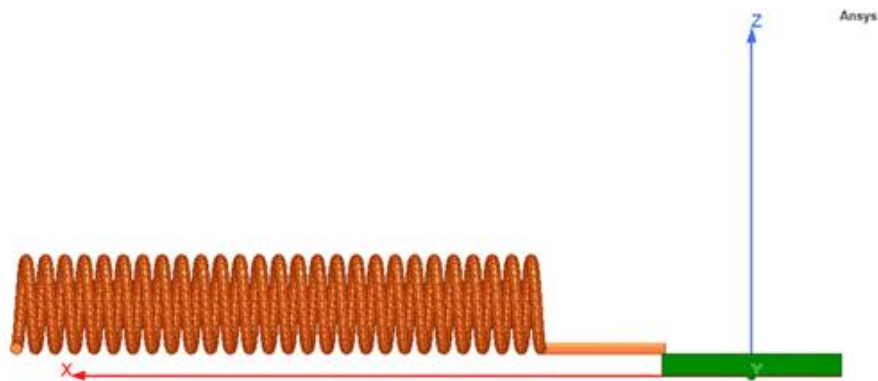
3.1.1 Half-inch Microstrip Line

The helical structure is connected at one end of a half-inch microstrip line, and the $50\ \Omega$ generator input is connected at the other end of the microstrip line. The ground plane of the microstrip line serves as the ground plane for the helix structure, thus composing the NMHAS. Figure 3.1 displays the top-view and side-view of the structure simulated on ANSYS-HFSS (the radiation box is not depicted in the figure). Figure 3.2 shows the computed frequency response of Helix connected to

the half-inch microstrip line. Specifically, Figure 3.2a displays the magnitude of the reflection coefficient ($|S_{11_Simulated}|$), while Figure 3.2b and Figure 3.2c show the real and imaginary parts of the input impedance, respectively.



(a)



(b)

Figure 3.1: (a) Top-view of helix connected to half-inch microstrip line; (b) Side-view of helix connected to half-inch microstrip line.

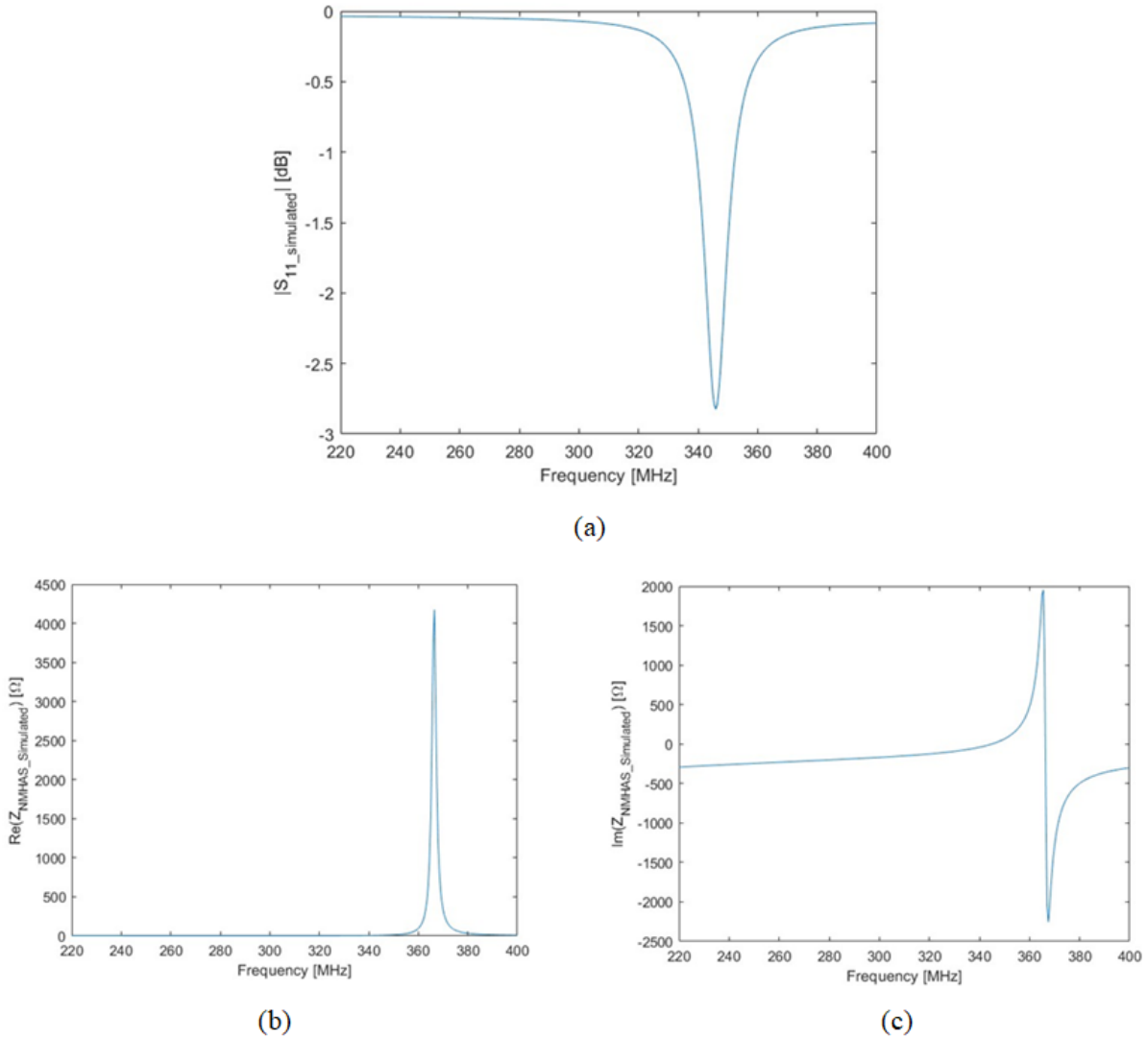


Figure 3.2: Frequency response of helix connected at the end of half-inch microstrip line: a) magnitude of reflection coefficient [dB]; b) real part of impedance [Ω]; c) imaginary part of the impedance [Ω].

3.1.2 One-inch Microstrip Line

The helical structure is connected to one end of a one-inch microstrip line, while the signal input is connected to the other end of the microstrip line, similarly to subsection 3.1.1. Figure 3.3 depicts both top-view and side-view of the structure are displayed simulated on ANSYS-HFSS. The frequency response of Helix connected to the one-inch microstrip line is shown in Figure 3.4.

Figure 3.4a plots $|S_{11_Simulated}|$, while Figure 3.4b and Figure 3.4c plots the real and the imaginary parts of the input impedance.

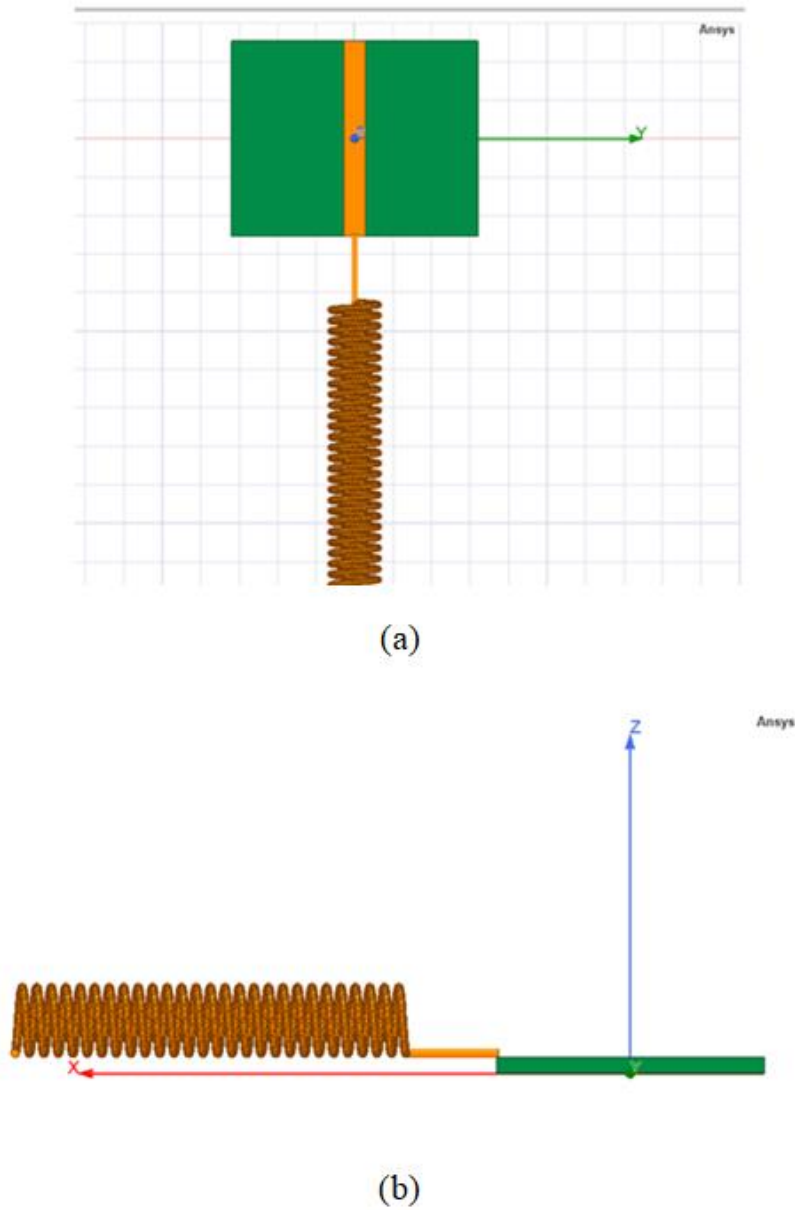
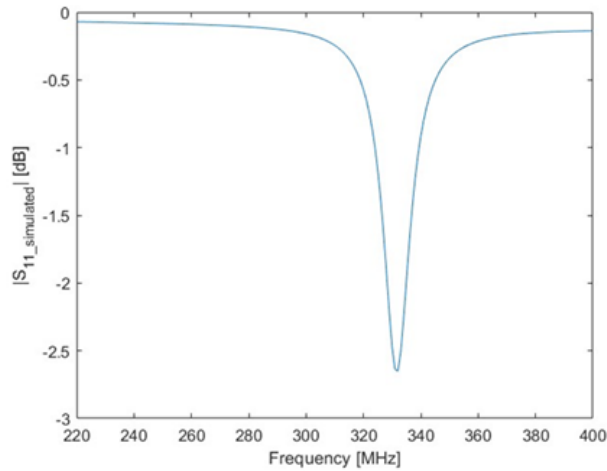
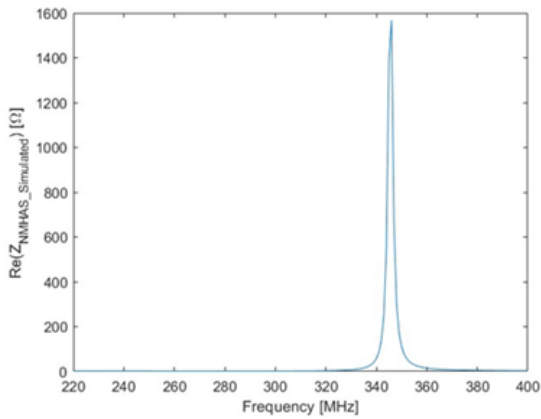


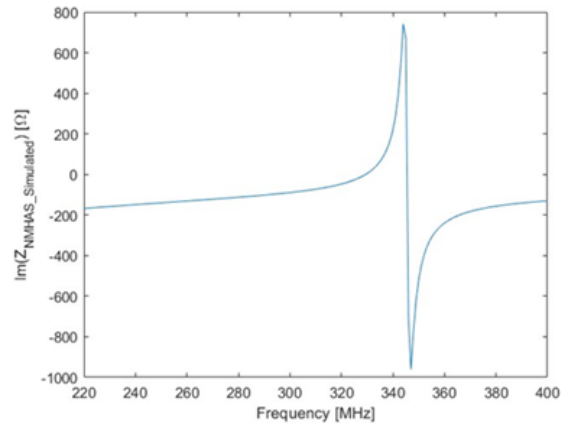
Figure 3.3: a.) Top-view of the helix connected to one-inch microstrip line; b.) Side-view of the helix connected to one-inch microstrip line.



(a)



(b)

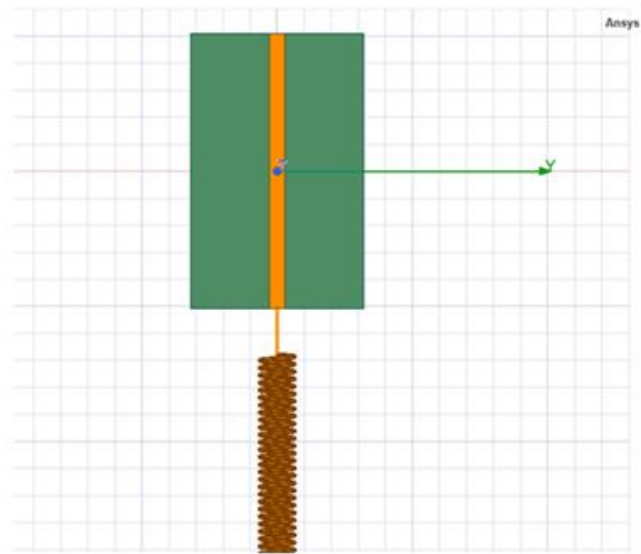


(c)

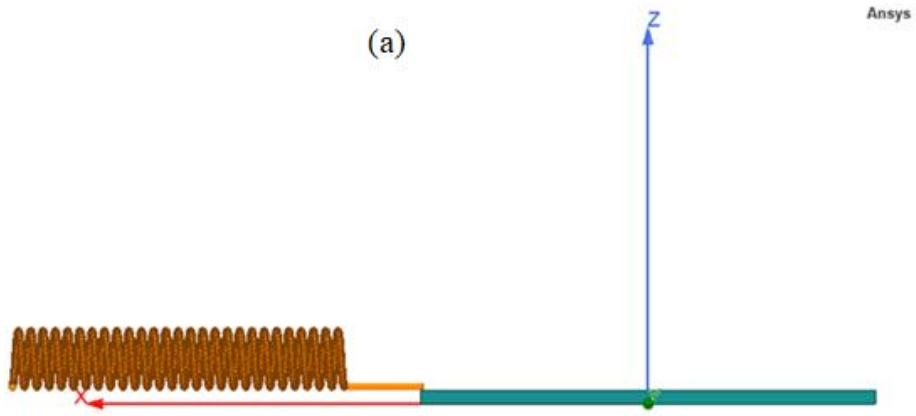
Figure 3.4: Frequency response of helix connected at the end of one-inch microstrip line: a) magnitude of reflection coefficient [dB]; b) real part of impedance [Ω]; c) imaginary part of the impedance [Ω].

3.1.3 Two-inch Microstrip Line

Helical structure is connected at one end of a two-inch microstrip line, while the signal input is located at the other end of the microstrip line. Figure 3.5 shows both top-view and side-view of the structure simulated on ANSYS-HFSS. The frequency response of helix connected to the two-inch microstrip line is shown in Figure 3.6. Figure 3.6a displays $|S_{11_Simulated}|$, Figure 3.6b shows the real part of input impedance, and Figure 3.6c shows the imaginary part of input impedance.

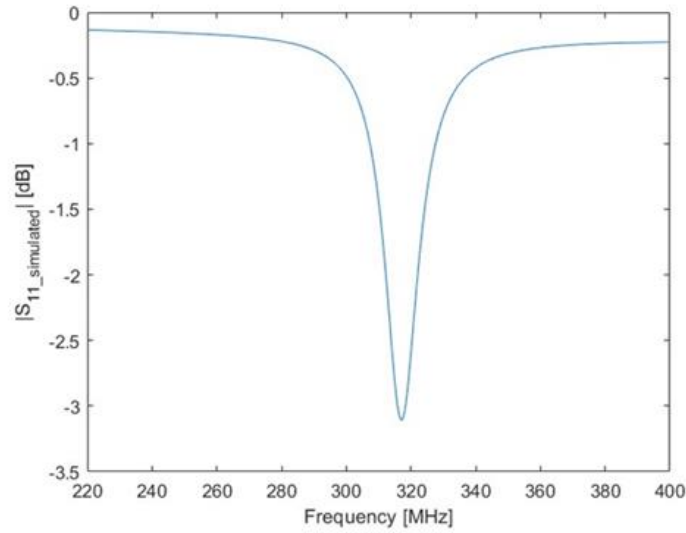


(a)

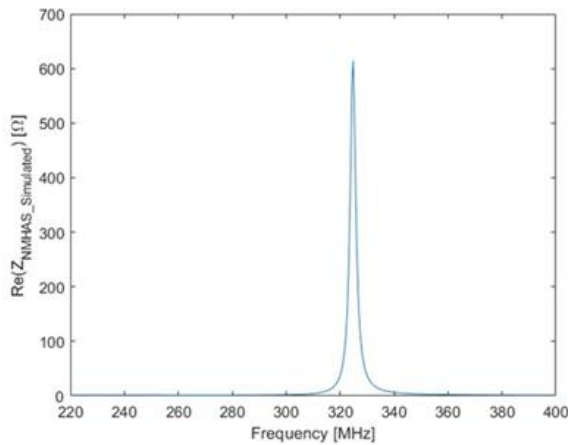


(b)

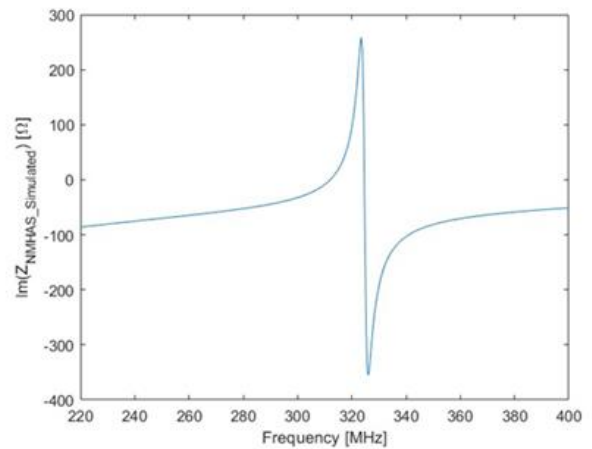
Figure 3.5: a.) Top-view of the helix connected to two-inch microstrip line; b.) Side-view of the helix connected to two-inch microstrip line.



(a)



(b)



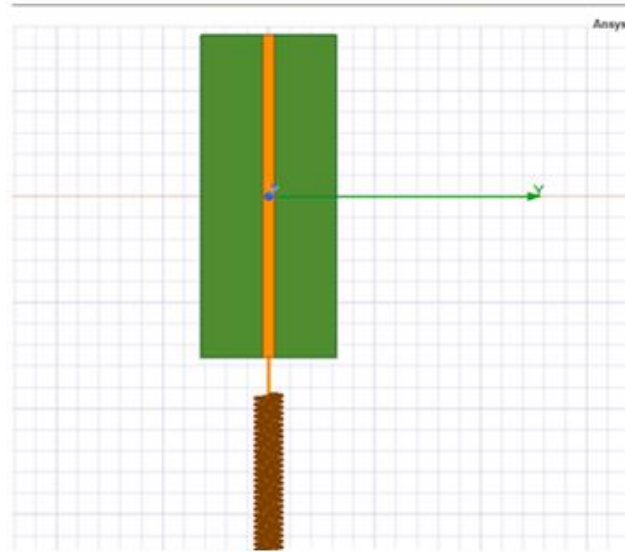
(c)

Figure 3.6: Frequency response of helix connected at the end of two-inch microstrip line: a) magnitude of reflection coefficient [dB]; b) real part of impedance [Ω]; c) imaginary part of the impedance [Ω].

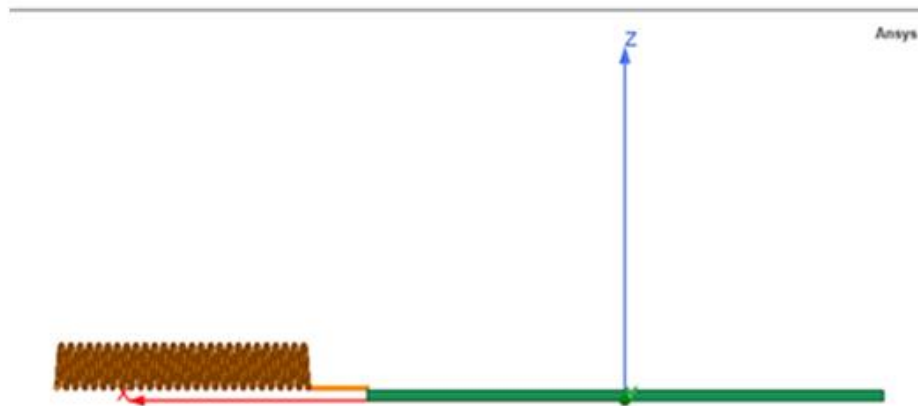
3.1.4 Three-inch Microstrip Line

Helical structure is connected at one end of a three-inch microstrip line, while the signal input is located at the other end of the microstrip line. Figure 3.7 illustrates both the top-view and side-view of the structure simulated on ANSYS-HFSS. Figure 3.8 shows the frequency response of Helix connected to the three-inch microstrip line, where Figure 3.8a displays $|S_{11_Simulated}|$,

Figure 3.8b shows the real part of input impedance, and Figure 3.8c shows the imaginary part of input impedance.



(a)



(b)

Figure 3.7: a.) Top-view of the helix connected to three-inch microstrip line; b.) Side-view of the helix connected to three-inch microstrip line.

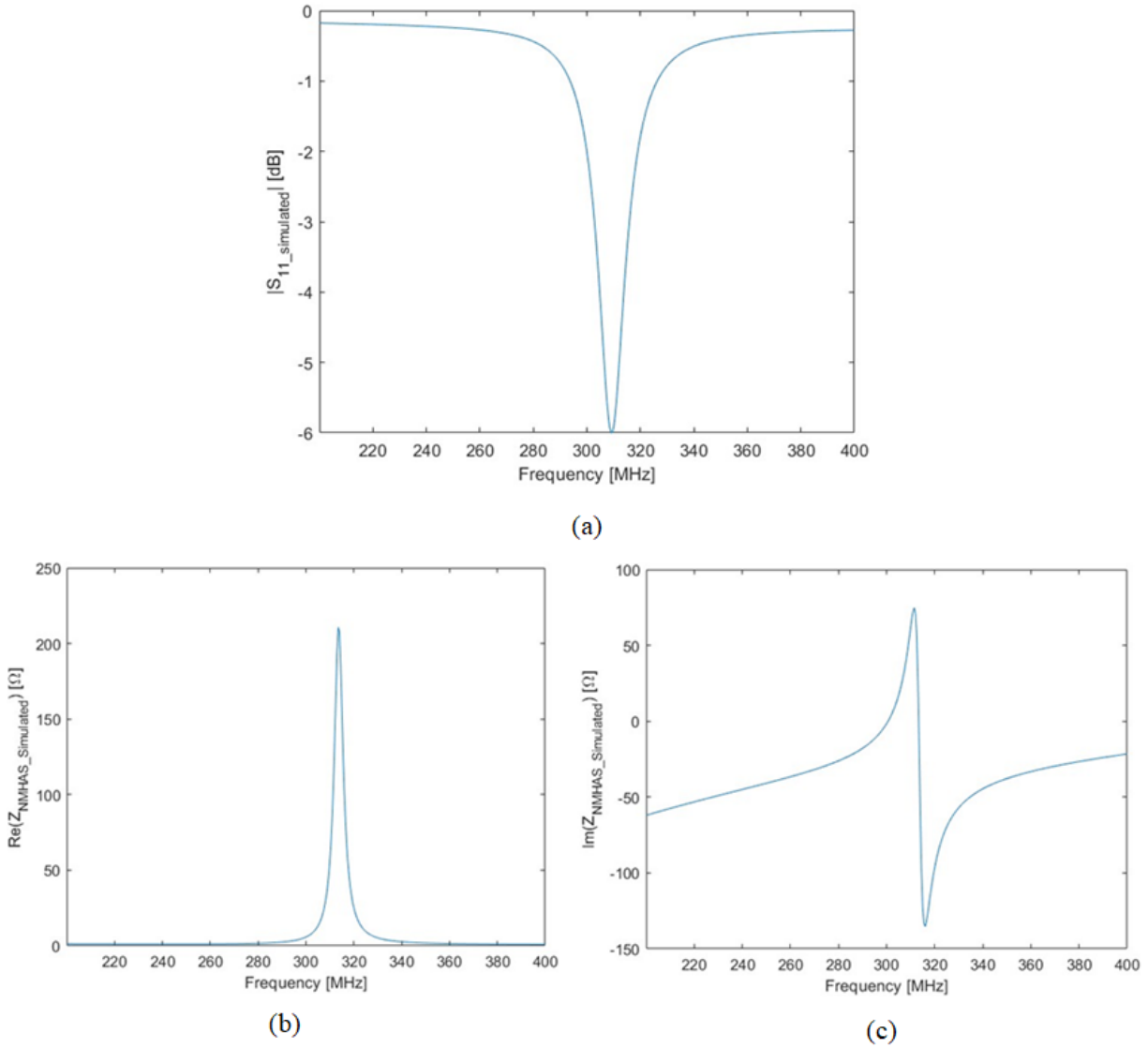


Figure 3.8: Frequency response of helical structure connected at the end of three-inch microstrip line: a) magnitude of reflection coefficient [dB]; b) real part of impedance [Ω]; c) imaginary part of the impedance [Ω].

3.1.5 Consideration of the Microstrip Length on the Calculations of the NMHAS

Impedance using HFSS

The comparison of $\text{Re}(Z_{\text{NMHAS}})$ is done by transferring the simulated $Z_{\text{NMHAS_Simulated}}$ of each different microstrip line to the end of each respective line where the helix structure is connected, that is transferring the impedance from point I to point L, as shown in Figure 3.9. The phase delay

on the lines are given by βd_i , where β is the wavenumber for the microstrip line and d_i are the different microstrip line lengths. The wavelength for the microstrip line is calculated using LineCalc tool on Keysight ADS at 300 MHz and using the FR-4 substrate parameters, $\lambda = 54$ cm.

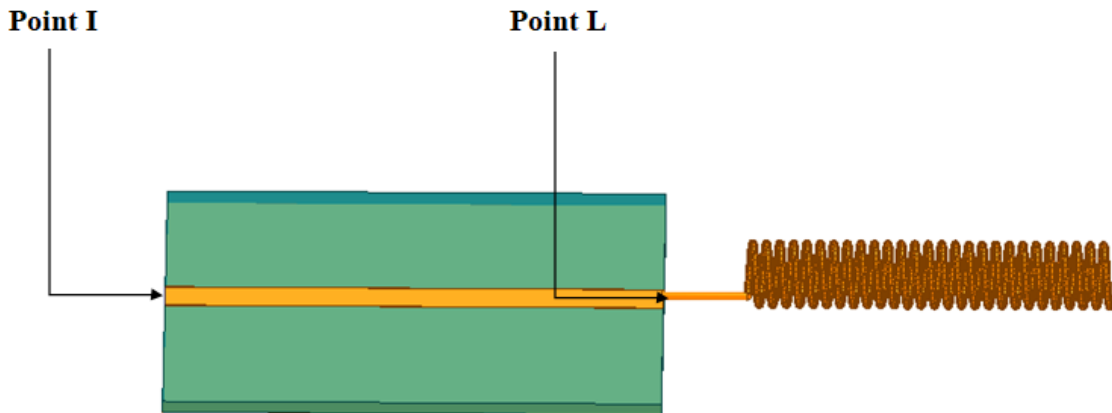


Figure 3.9: Reference points for transferring the impedance.

The impedances at Point L, also labeled transferred impedances from this point on in the text, at the resonant frequencies for different lengths of microstrip lines 0.5 inch, 1 inch, 2 inches and 3 inches are labelled as Z_A , Z_B , Z_C and Z_D respectively. Table 3.1 presents the simulated input impedance and transferred input impedance and Table 3.2 presents the percentage change of the resonant frequency (f_{r1}) with respect to three-inch microstrip line. Figure 3.10 plots the simulated input impedance and transferred input impedance for different microstrip lines on the Smith Chart.

Length of microstrip line	Simulated input impedance ($Z_{NMHAS_Simulated}$) [Ω] (Point I, Figure 3.9)	Transferred input impedance (Z_{NMHAS}) [Ω] (Point L, Figure 3.9)
Half-inch	4180-j691	$Z_A = 6.97+j165.0$
One-inch	1570-j704	$Z_B = 4.46+j76.7$
Two-inch	615-j96	$Z_C = 4.67+j21.0$
Three-inch	211-j15	$Z_D = 12.20-j8.7$

Table 3.1: Input impedance simulated on HFSS and transferred input impedance.

Length of microstrip line	Resonant frequency (f_{r_i}) [MHz]	Change in f_r [%]
Half-inch	366.5	16.9
One-inch	346.0	10.3
Two-inch	324.8	3.6
Three-inch	313.5	-

Table 3.2: Change in resonant frequency with increase in length of microstrip line on HFSS

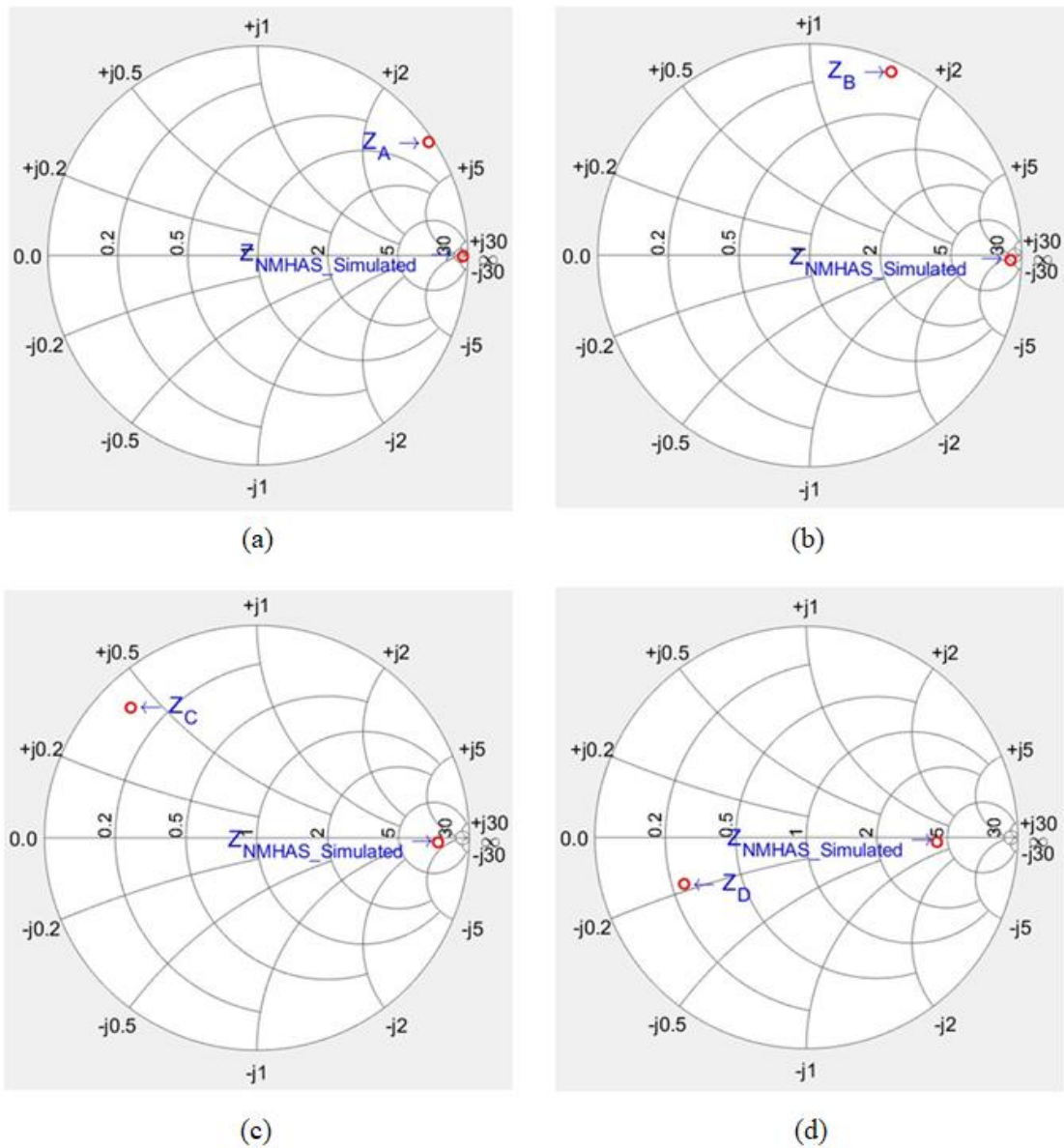


Figure 3.10: Smith plots of simulated and transferred impedance presented in Table 3.1 for: a.) half-inch microstrip line; b.) one-inch microstrip line; c.) two-inch microstrip line; d.) three-inch microstrip line

From Table 3.1, Table 3.2 and Figure 3.10 it can be observed that with the increase in size of the ground plane from 0.5 inch to 3 inch the resonant frequency decreases and the reactance goes from inductive towards capacitive around the 300 MHz operating frequency. Figure 3.11 presents transferred impedances (Point L in Figure 3.9) Z_A , Z_B , Z_C and Z_D for the different microstrip lengths in a single Smith Chart for convenience.

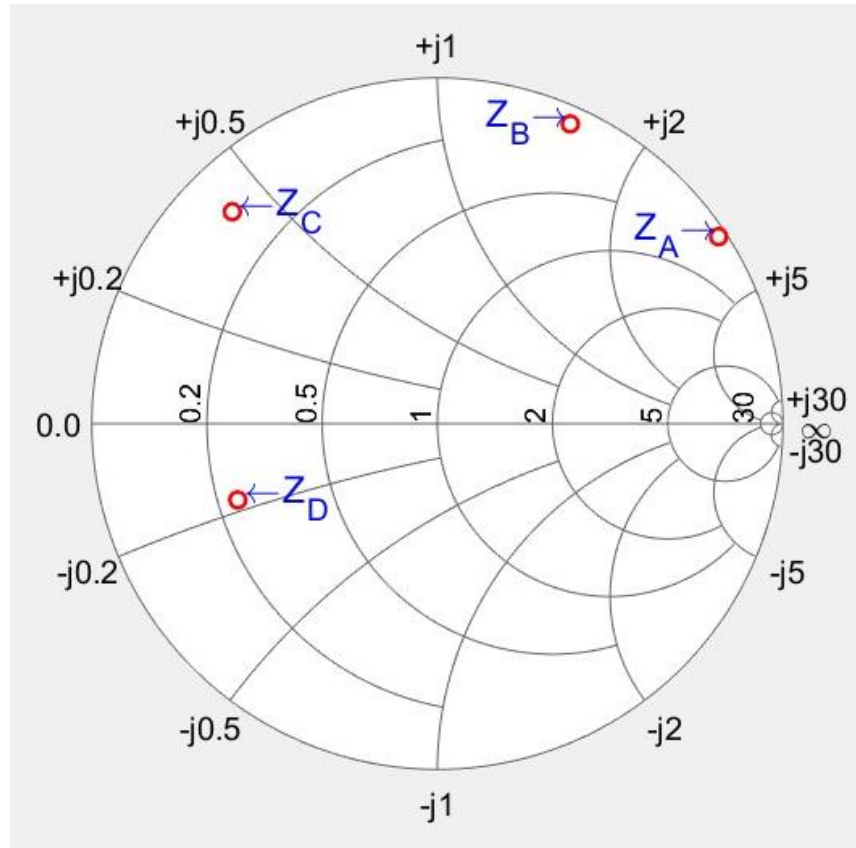


Figure 3.11: Transferred impedances to Point L in Figure 3.9 for different microstrip lengths plotted on Smith Chart calculated from HFSS simulations.

3.2 Simulations of NMHAS on WIPL-D

This section discusses the simulations using WIPL-D of helix connected to different lengths of microstrip line. The dimensions of the structure used for the WIPL-D simulations are the same used in the ANSYS-HFSS simulations.

WIPL-D uses quasi realistic feeder as the wire connecting the ground plane and the top transmission line can never be on dielectric surface. So, the substrate is extended by $0.1l_s$ (where l_s is the length of the substrate as mentioned in Section 2.3) and two trapezoidal metallic plates are immersed in the substrate (Figure 3.12b). A wire with generator is connected between these trapezoidal plates. This works as a feeder network for microstrip. Figure 3.12a shows the NMHAS

simulated on WIPL-D and Figure 3.12b shows the trapezoidal plates connection at points AA'(Figure 3.12a) with the wire and generator connected between them.

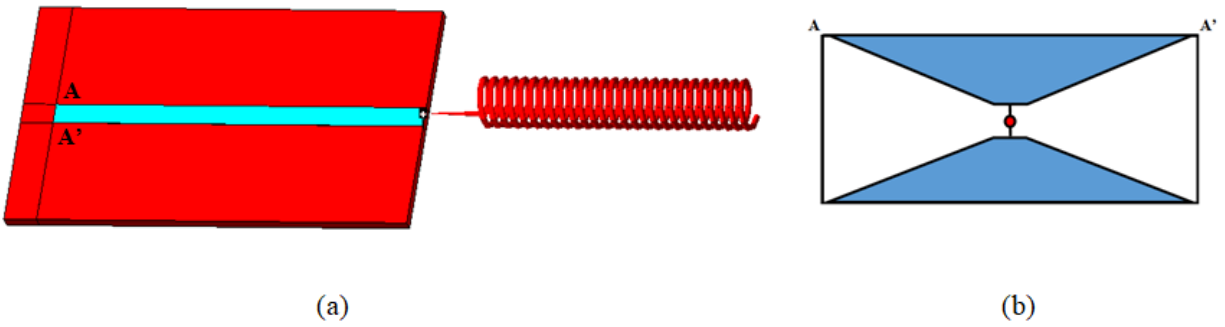


Figure 3.12: a.) NMHAS design simulated on WIPL-D; b) Trapezoidal plates with wire and generator connected between them.

3.2.1 Half-inch Microstrip Line

Figure 3.13 shows the NMHAS implemented on WIPL-D platform. The figure shows helix connected to a half-inch microstrip line.

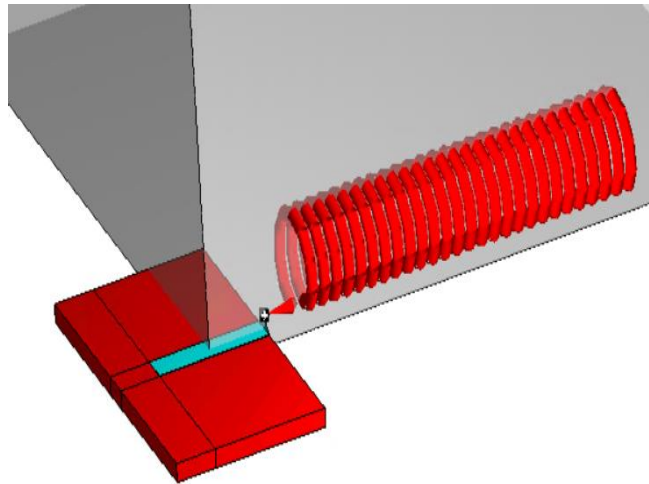
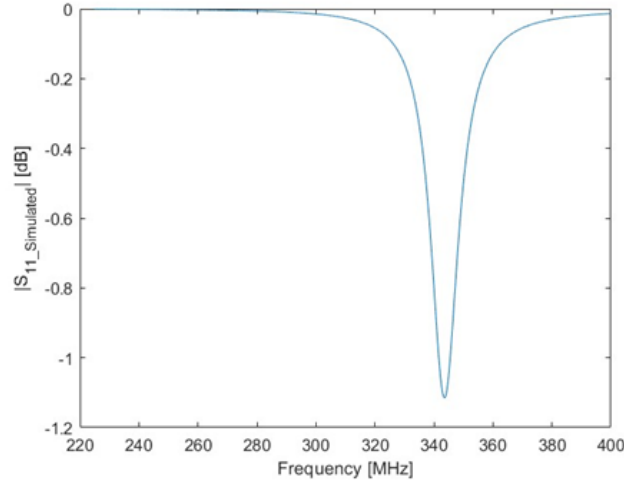
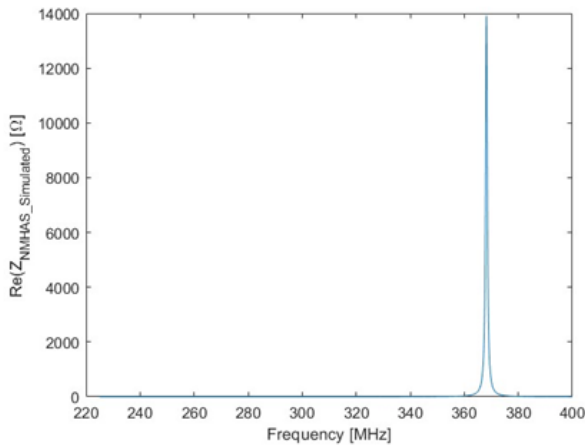


Figure 3.13: Helix connected to half-inch microstrip line simulated on WIPL-D. The gray area is the axes on WIPL-D.

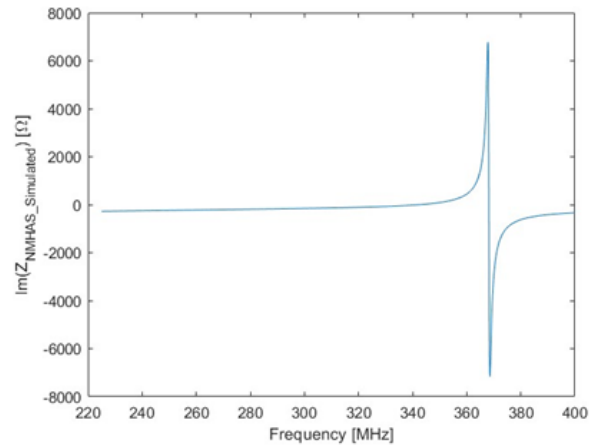
Figure 3.14 shows the frequency response of helix connected to half-inch microstrip line. Figure 3.14a shows the magnitude of reflection coefficient ($|S_{11}|$), Figure 3.14b shows the real part of input impedance and Figure 3.14c shows the imaginary part of input impedance.



(a)



(b)



(c)

Figure 3.14: Frequency response of helix connected at the end of half-inch microstrip line: a) magnitude of reflection coefficient [dB]; b) real part of impedance [Ω]; c) imaginary part of the impedance [Ω].

3.2.2 One-inch Microstrip Line

Figure 3.15 shows the NMHAS implemented on WIPL-D platform. The figure shows helix connected to a one-inch microstrip line.

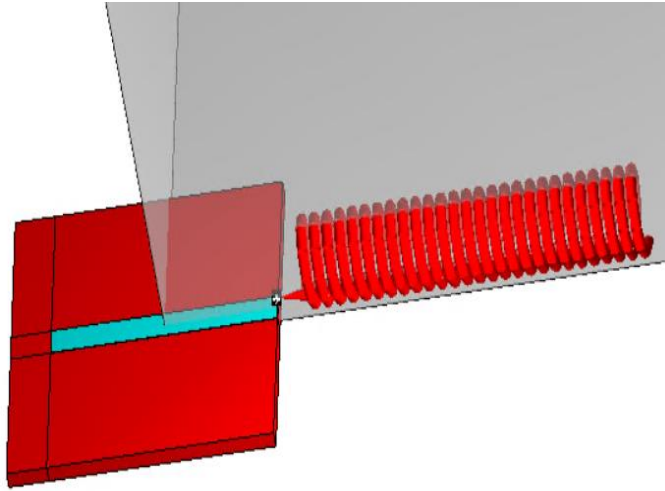


Figure 3.15: Helix connected to one-inch microstrip line simulated on WIPL-D. The gray area is the axes on WIPL-D.

Figure 3.16 shows the frequency response of helix connected to one-inch microstrip line. Figure 3.16a shows the magnitude of reflection coefficient ($|S_{11}|$), Figure 3.16b shows the real part of input impedance and Figure 3.16c shows the imaginary part of input impedance.

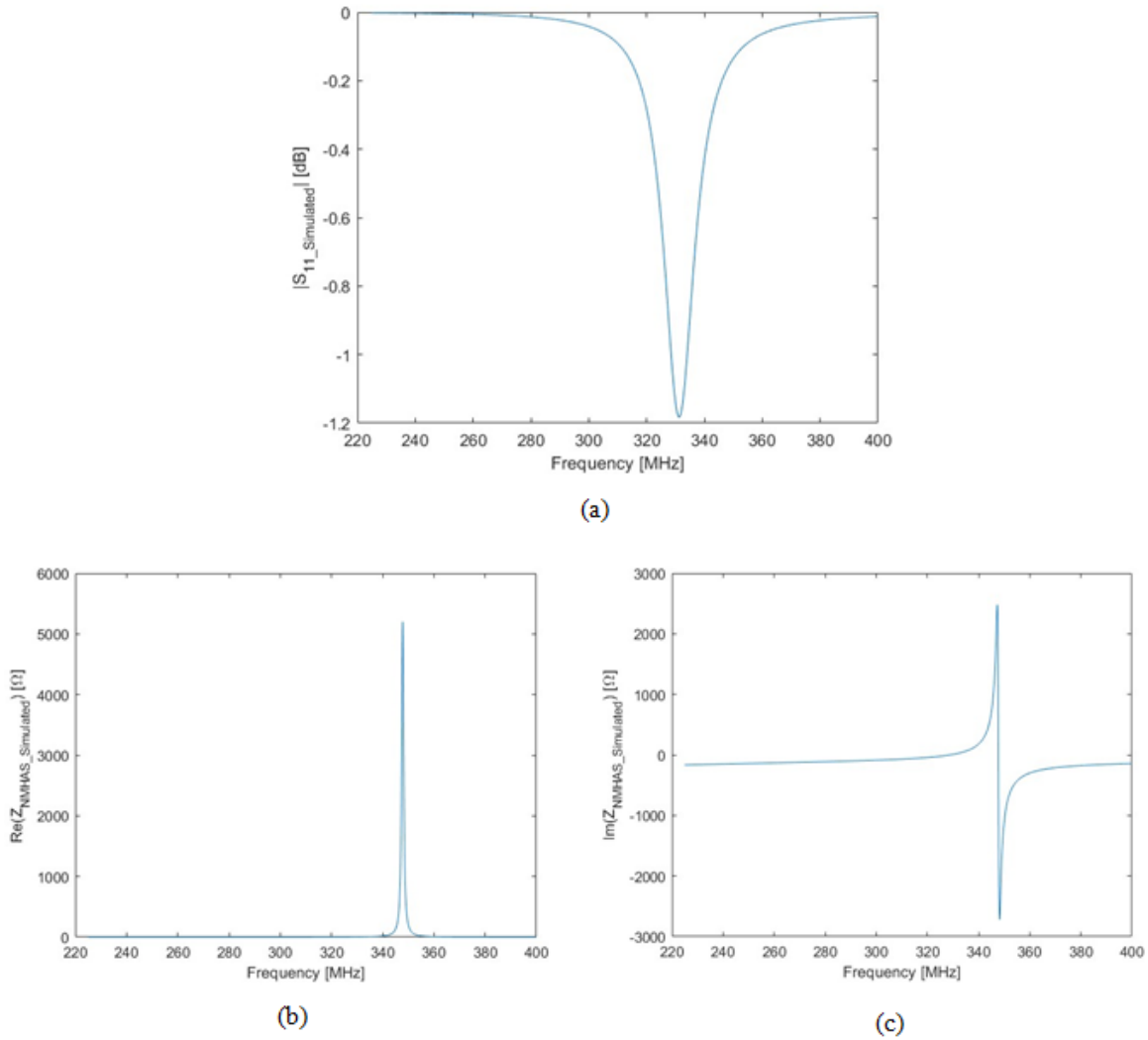


Figure 3.16: Frequency response of helix connected at the end of one-inch microstrip line: a) magnitude of reflection coefficient [dB]; b) real part of impedance [Ω]; c) imaginary part of the impedance [Ω].

3.2.3 Two-inch Microstrip Line

Figure 3.17 shows the NMHAS implemented on WIPL-D platform. The figure shows helix connected to a two-inch microstrip line.

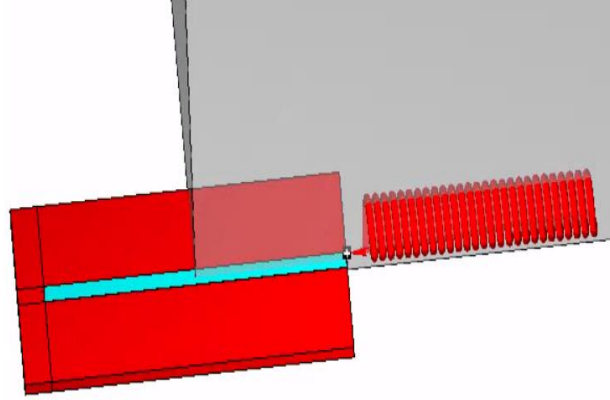


Figure 3.17: Helix connected to two-inch microstrip line simulated on WIPL-D. The gray area is the axes on WIPL-D.

Figure 3.18 shows the frequency response of helix connected to two-inch microstrip line. Figure 3.18a shows the magnitude of reflection coefficient ($|S_{11}|$), Figure 3.18b shows the real part of input impedance and Figure 3.18c shows the imaginary part of input impedance.

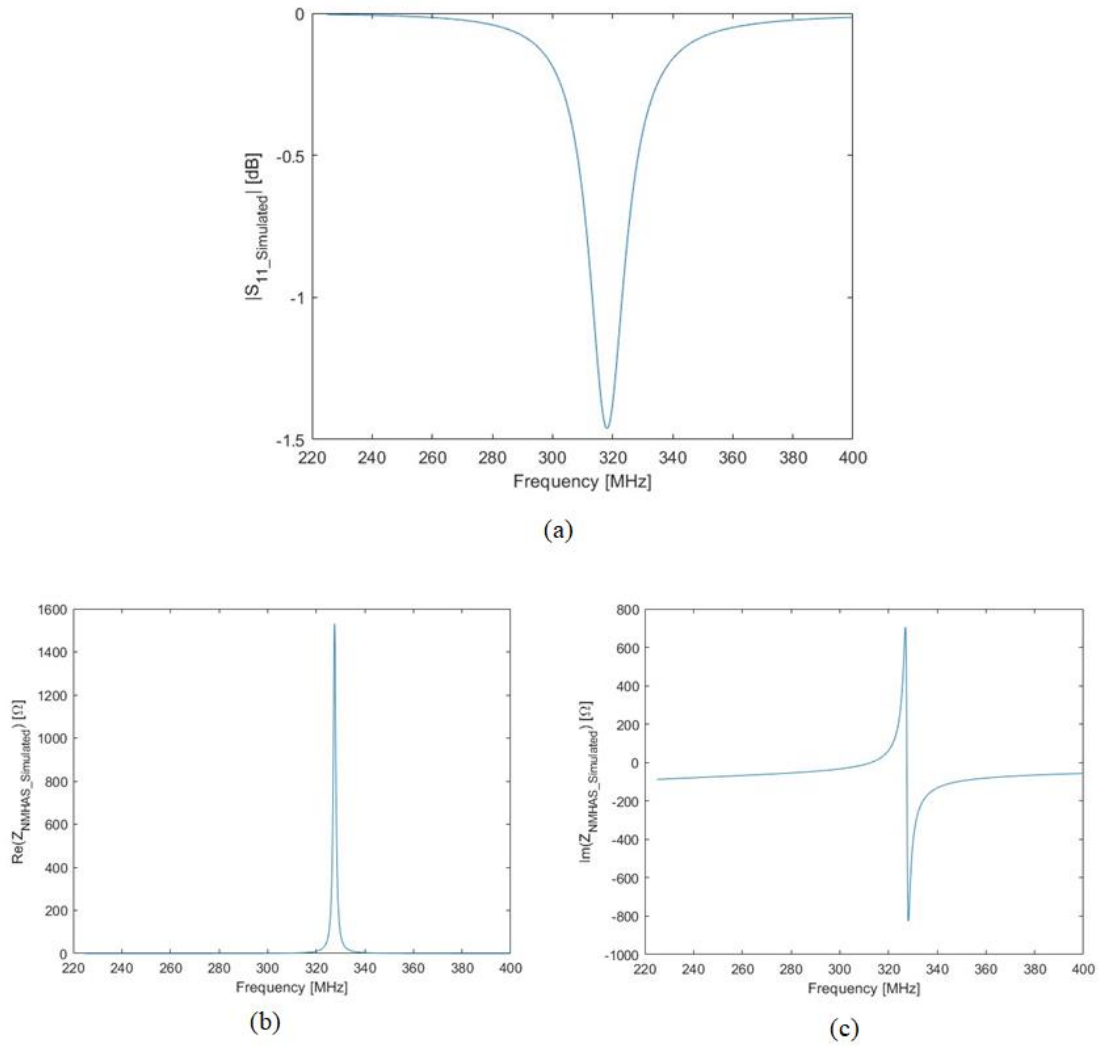


Figure 3.18: Frequency response of helix connected at the end of two-inch microstrip line: a) magnitude of reflection coefficient [dB]; b) real part of impedance [Ω]; c) imaginary part of the impedance [Ω].

3.2.4 Three-inch Microstrip Line

Figure 3.19 shows the NMHAS implemented on WIPL-D platform. The figure shows the helix connected to a three-inch microstrip line.

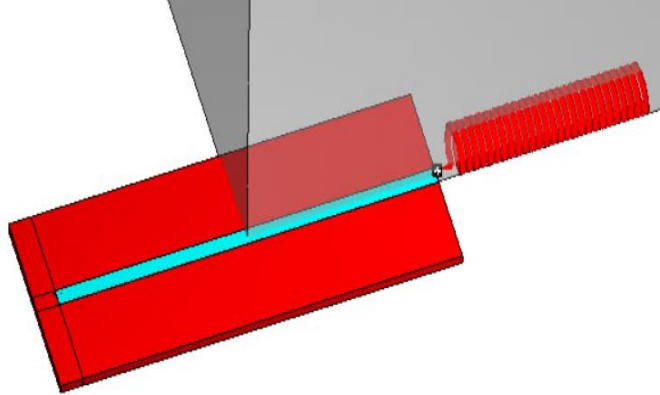


Figure 3.19: Helix connected to three-inch microstrip line simulated on WIPL-D. The gray area is the axes on WIPL-D.

Figure 3.20 shows the frequency response of helix connected to three-inch microstrip line. Figure 3.20a shows the magnitude of reflection coefficient ($|S_{11}|$), Figure 3.20b shows the real part of input impedance and Figure 3.20c shows the imaginary part of input impedance.

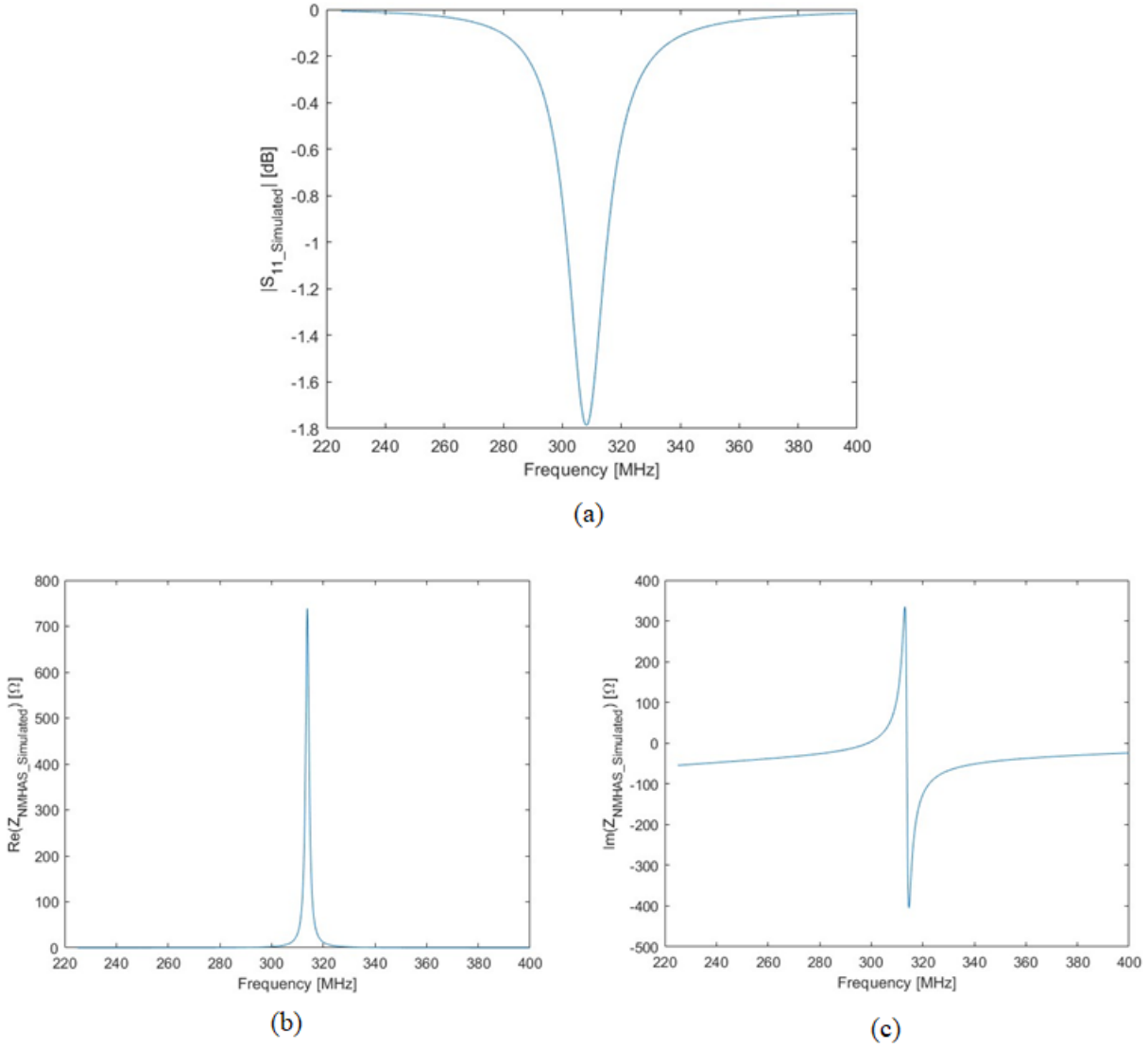


Figure 3.20: Frequency response of helix connected at the end of three-inch microstrip line: a) magnitude of reflection coefficient [dB]; b) real part of impedance [Ω]; c) imaginary part of the impedance [Ω].

3.2.5 Discussion of Microstrip Length Effect on the NMHAS Impedance Calculation using WIPL-D

As discussed in Section 3.1.5, the input impedances simulated $Z_{NMHAS_Simulated}$ using WIPL-D for different microstrip lines are transferred to the end of each respective line. The Table 3.3 presents the simulated input impedance and transferred input impedance and Table 3.4 presents the percentage change of the resonant frequency (f_{r1}) with respect to three-inch microstrip line

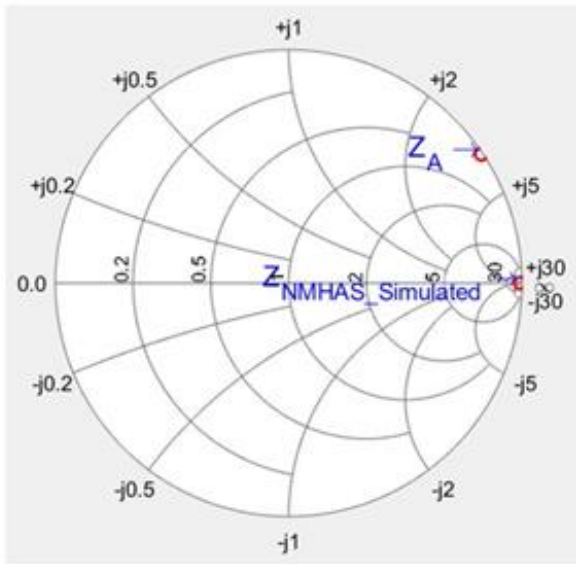
simulated on WIPL-D. Figure 3.21 plots the simulated input impedance and transferred input impedance for different microstrip lines on smith chart.

Length of microstrip line	Simulated input impedance ($Z_{NMHAS_Simulated}$) [Ω]	Transferred input impedance (Z_{NMHAS}) [Ω]
Half-inch	13780+j368	$Z_A = 2.0+j164.7$
One-inch	5203-j48	$Z_B = 1.6+j74.6$
Two-inch	1525-j28	$Z_C = 1.9+j20.5$
Three-inch	737-j19	$Z_D = 3.5-j10.0$

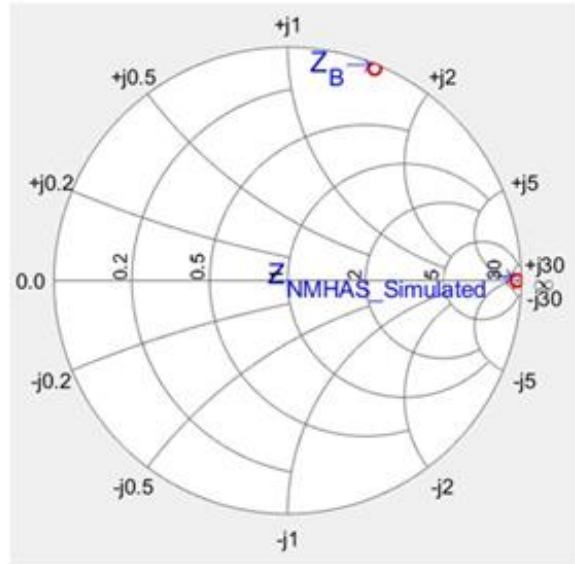
Table 3.3: Input impedance simulated on WIPL-D and transferred input impedance.

Length of microstrip line	Resonant frequency (f_{r_i}) [MHz]	Change in f_r [%]
Half-inch	368.2	17.3
One-inch	347.8	10.8
Two-inch	327.5	4.3
Three-inch	313.9	-

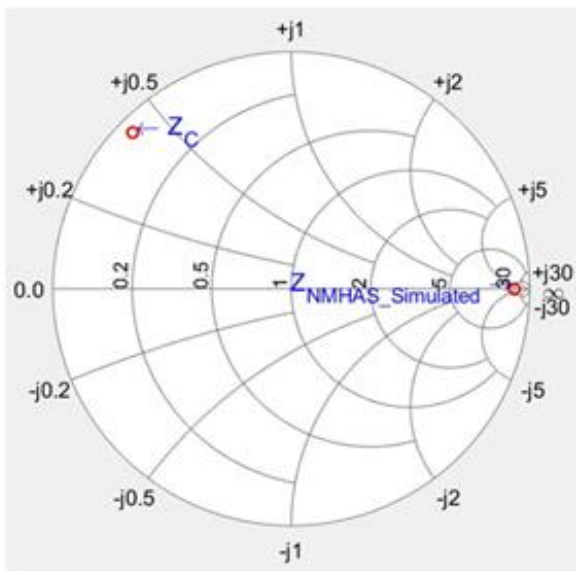
Table 3.4: Change in resonant frequency and input impedance with increase in length of microstrip line on WIPL-D.



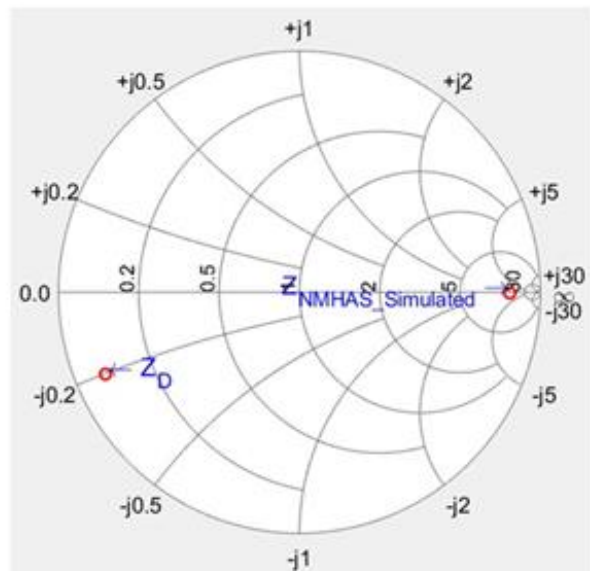
(a)



(b)



(c)



(d)

Figure 3.21: Smith plots of simulated and transferred impedance presented in Table 3.3 for: a.) half-inch microstrip line; b.) one-inch microstrip line; c.) two-inch microstrip line; d.) three-inch microstrip line

From Table 3.3, Table 3.4 and Figure 3.21 it can be concurred that similarly to what was observed with HFSS with the increase in size of the ground plane from 0.5 inch to 3 inch the resonant

frequency decreases and the reactance goes from inductive towards capacitive around the 300 MHz operating frequency. Figure 3.22 presents transferred impedances (Point L, Figure 3.9) Z_A , Z_B , Z_C and Z_D for the different microstrip lengths in a single Smith Chart for convenience.

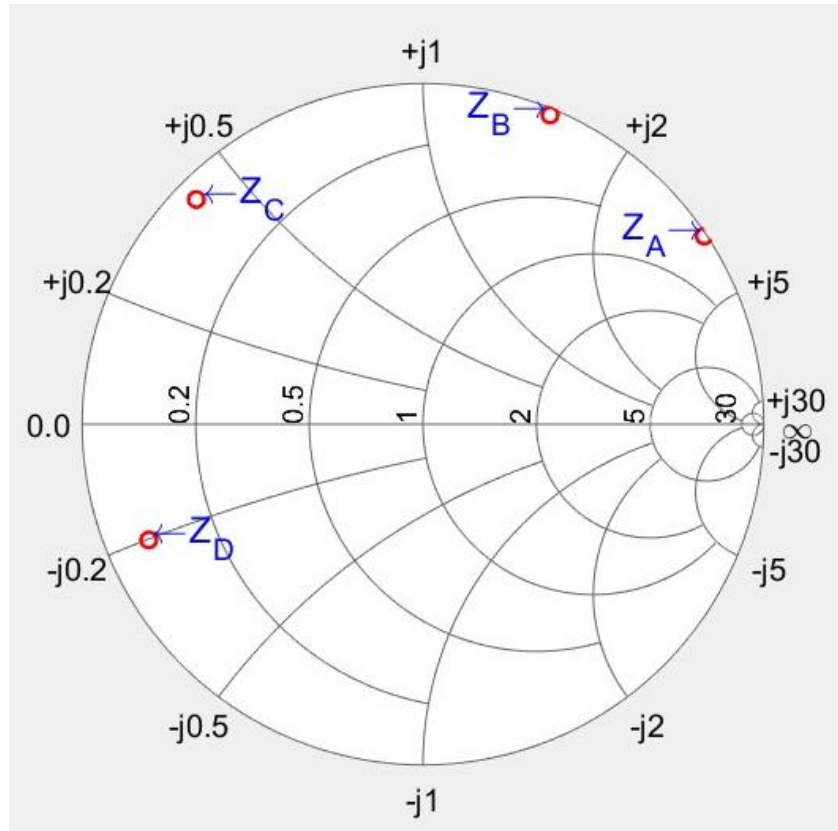


Figure 3.22: Transferred impedances to Point L in Figure 3.9 for different microstrip lengths plotted on Smith Chart calculated from WIPL-D simulations.

From the simulations on HFSS and WIPL-D of helix connected to different microstrip lengths, it is observed that the imaginary part of input impedance of the NMHAS goes from inductive to capacitive at 300 MHz as increased the line lengths and thus the respective ground planes increased from 0.5 inch to 3 inch. And as noted before, with the increase in length of the ground plane, the resonant frequency diminishes. Next section compares the variations between the HFSS simulations and the WIPL-D simulations.

3.3 Comparison of HFSS and WIPL-D Simulations:

In this section the frequency response impedances of the NMHAS simulated using HFSS and WIPL-D are compared for the two-inch microstrip line, since this length was selected for the measurements reported in Chapter 4 and Chapter 5. For microstrip length \geq two-inch, the measured $\text{Re}(Z_{\text{NMHAS}})$ was close to 50Ω . The two-inch length was selected for compactness. Figure 3.23a and Figure 3.23b plot the simulated real and imaginary part of the NMHAS input impedance at the input of the microstrip line, that is at Point I in Figure 3.9.

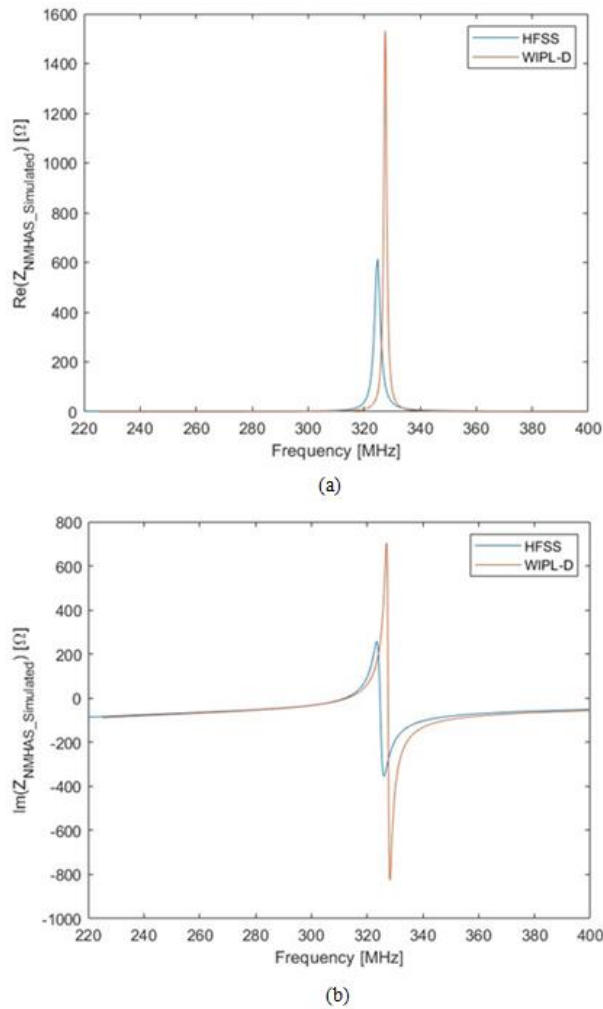


Figure 3.23: Simulated NMHAS input impedance utilizing both WIPL-D and HFSS: a.) real part input impedance [Ω]; b.) imaginary part of input impedance [Ω].

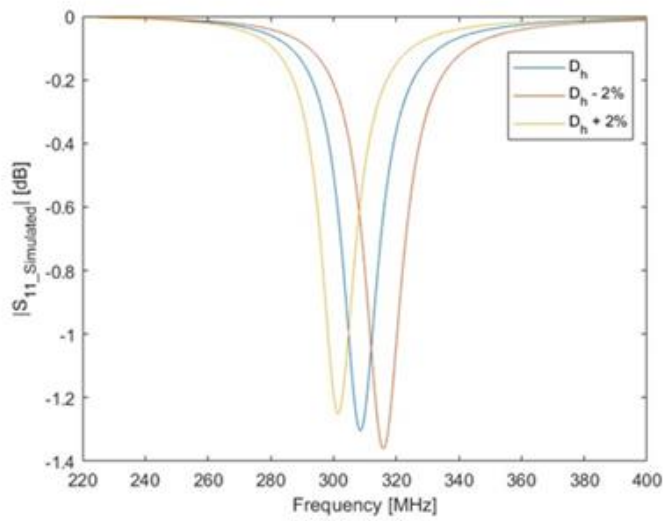
As can be seen from Figure 3.23, the NMHAS resonant frequency predicted by HFSS and WIPL-D are in agreement within 0.6%. Since the WIPL-D model does not include material losses in substrate and conductors, the values of input impedance calculated using both software packages cannot be meaningfully compared.

3.4 Sensitivity of NMHAS

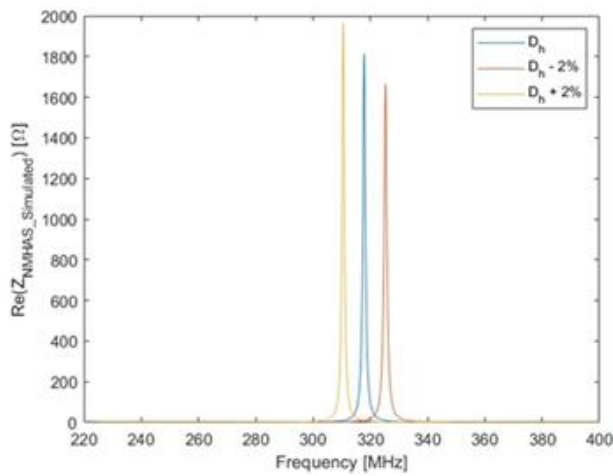
This section focuses on the investigation of the NMHAS frequency sensitivity with respect to variations in different parameters of the helix using WIPL-D simulations. WIPL-D was selected for the frequency response simulations, since it allowed timely simulations for the NMHAS varying dimensions. Regarding impedance responses, WIPL-D is not amenable to the inclusion of conductor and dielectric losses and thus further modelling or software improvement will be required to better model the NMHAS impedance. The diameter of the helix and height of the helix were varied by 2% and the change in NMHAS response was observed. Although the helix dimensions cannot be controlled tightly around 2%, this value was chosen to study the sensitivity of the NMHAS frequency response to small variations in dimensions.

3.4.1 Variation of D_h

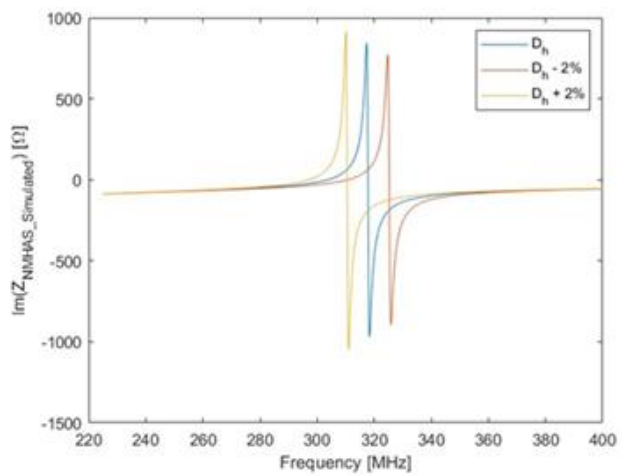
This section discusses the effect of diameter (D_h) of the helical structure on the frequency response. The helical structure is modelled and simulated on WIPL-D using three different values for diameter of helix with other parameters being constant: $H = 35.59$ mm, $h = 8$ mm, $N = 27$ and two-inch microstrip line. Figure 3.24 compares the response of the NMHAS when the radius of the helix is increased by 2% and decreased by 2% with respect to the original parameter value.



(a)



(b)



(c)

Figure 3.24: Frequency response of NMHAS with two-inch microstrip line with respect to variation in D_h : a.) $|S_{11}|$ [dB]; b.) real part of input impedance [Ω]; c.) imaginary part of input impedance [Ω].

Table 3.5 shows the percentage change in resonant frequency with respect to the percentage change in diameter of the helix (D_h). From Table 3.5 it can be inferred that 2% change in diameter of the helix, effects the resonant frequency by approximately 2.3%. With the increase in diameter of the helix, the resonant frequency decreases. In later chapters, this information is used to explain the

discrepancies between the measured and simulated response of the NMHAS. With $\Delta D_h = 0.12$ mm a $\Delta f_r = 7.35$ MHz was observed.

Parameter	Parameter Value [mm]	Resonant Frequency (f_{r_i}) [MHz]	change in f_r [%]
$D_h - 2\%$	6.23	325.24	-2.31
D_h	6.35	317.89	-
$D_h + 2\%$	6.48	310.53	+2.31

Table 3.5: Change in resonant frequency with respect to change in diameter of helix.

3.4.2 Variation of H

This section discusses the effect of the height (H) of the helical structure on the frequency response. The helical structure is modelled and simulated on WIPL-D using three different values for height of helix with other parameters kept constant: $D_h = 6.35$ mm, $h = 8$ mm, $N = 27$ and two-inch microstrip line. Figure 3.25 compares the response of the NMHAS when the height of helix is increased by 2% and decreased by 2% with respect to the original parameter value.

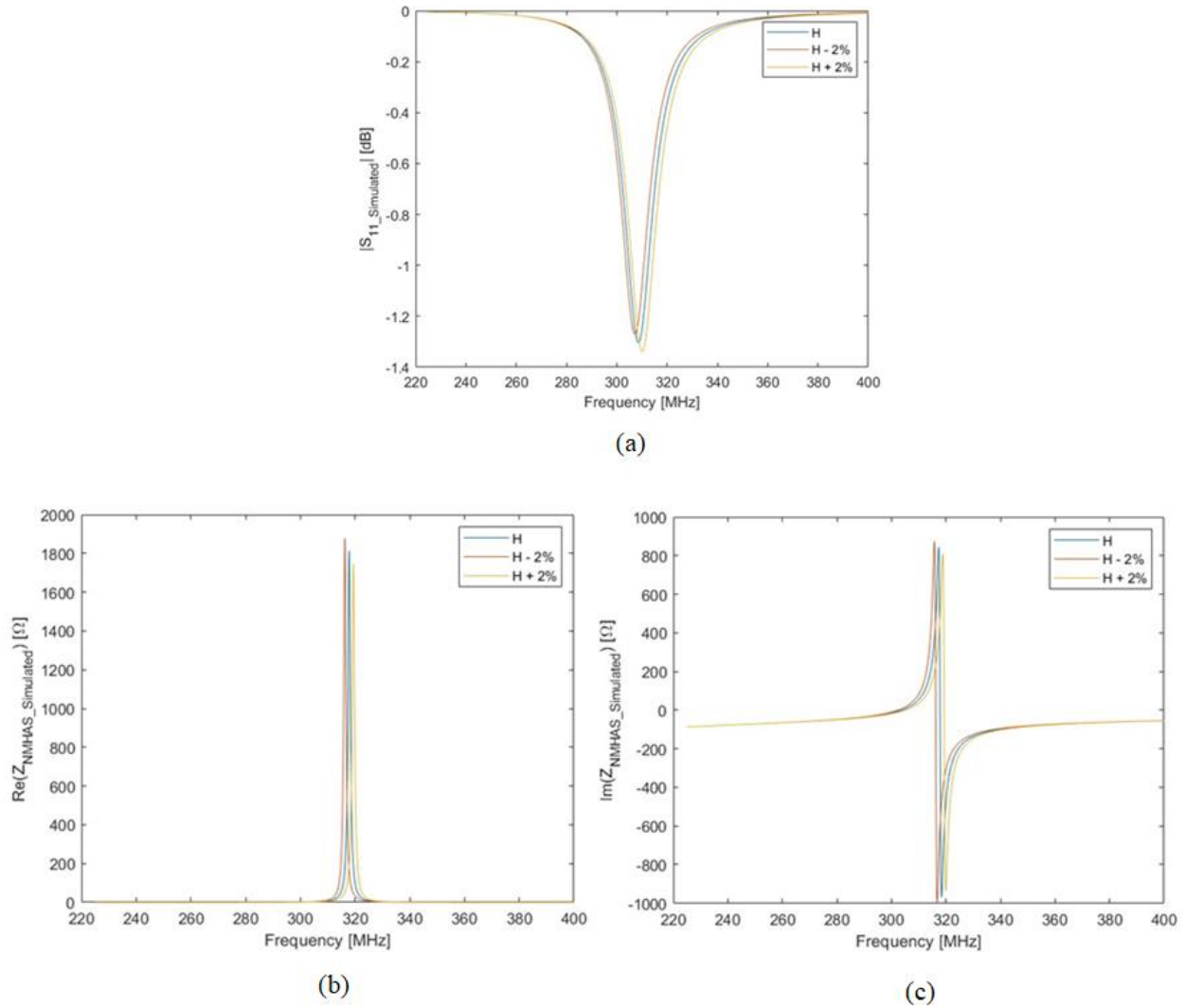


Figure 3.25: Frequency response of NMHAS with two-inch microstrip line w.r.to variation in H: a.) $|S_{11}|$ [dB]; b.) real part of input impedance [Ω]; c.) imaginary part of input impedance [Ω].

Table 3.6 shows the percentage change in resonant frequency with respect to the percentage change in height of the helix (H). From Table 3.6 it can be inferred that with 2% change in height of the helix, the resonant frequency changes by 0.48%. With the increase in height of helix, the resonant frequency increases. With $\Delta H = 0.71$ mm a $\Delta f_r = 1.54$ MHz was observed.

Parameter	Parameter Value [mm]	Resonant Frequency (f_{r_i}) [MHz]	change in f_r [%]
H - 2%	34.88	316.35	-0.48
H	35.59	317.89	-
H + 2%	36.30	319.43	+0.48

Table 3.6: change in resonant frequency with respect to change in height of helix.

3.3 Conclusions

This chapter discussed the S_{11} simulation of NMHAS in a 50Ω system using two commercially available software platforms: HFSS and WIPL-D. The NMHAS was simulated with four different microstrip lengths: 0.5 inch, 1 inch, 2 inch, 3 inch. With the increase in size of ground plane the resonant frequency diminishes. At resonance, the input impedance was transferred from the input to the end of the microstrip lines to allow for comparison, and it was observed that the reactance of transferred impedance goes from inductive towards capacitive. The sensitivity of NMHAS to various structural parameters was also discussed with the aid of WIPL-D simulations and it was observed that the response of the NMHAS is highly sensitive to the diameter of helix.

CHAPTER 4. NMHAS FABRICATION AND EXPERIMENTAL SETUP IMPLEMENTATION

In this chapter mounting fixtures, equipment setup and data analysis are presented which target the measurement and characterization of the NMHAS discussed in the previous chapter. First, the balun introduced in Chapter 2 and utilized to measure the NMHAS with the VNA coaxial cable is introduced. Then network modelling of the balun structure is performed with the aid of the software ADS (Keysight, CA, USA). Finally, the testing assembly is used to demonstrate the measurement of the NMHAS.

4.1 Introduction of Balun

This section discusses the need for introduction of a balun. A balun is a device used to interface an unbalanced line to a balanced line. The NMHAS structure consists of the helix mounted on a microstrip line, which serves both as a connection to the helix and as the ground plane for the radiating structure. It was found that the connection of the microstrip line directly to the NMHAS resulted in a significant participation of the coaxial cable connecting the VNA to the NMHAS in the antenna radiation through the current flowing in the outer coaxial cable shield. Hence, a balun was placed between the cable and the NMHAS in an attempt to mitigate the participation of the coaxial cable shield in the radiation of the NMHAS.

4.2 Modeling of the Balun Mounted between the Coaxial Cable and the NMHAS

This section details the network modeling of the balun and its respective mounting through measurements of different loads connected to one of the terminals of the balun. In this work, a TC1-1-13M+ RF transformer (mini-circuits, USA) was used as balun [77]. Figure 4.1 shows the RF balun transformer used.

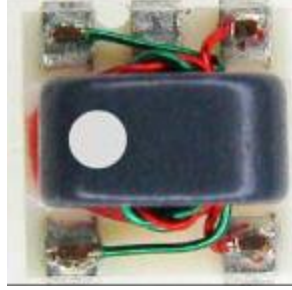


Figure 4.1: TC1-1-13M+ RF Transformer [77].

To assist in the balun modeling, different resistive loads shown in Figure 4.2 and listed in Table 4.1 were connected to the balanced terminal of the balun and a SMA connector was connected to the unbalanced terminal and the impedance of this setup is measured using a VNA. In addition to the resistive loads back-to-back baluns were connected to measure the phase delay in the overall structure. Figure 4.2a shows four 100 Ω resistors connected in parallel to form a 25 Ω resistance. Figure 4.2b shows 50 Ω directly connected at the end of the balun. In Figure 4.2c a 100 Ω is directly connected at the end of the balun. In Figure 4.2d a 100 Ω resistor and a 50 Ω resistor are connected in series to form 150 Ω . In Figure 4.2e two identical baluns are connected end to end. These values of resistance were chosen due to the availability of 50 Ω and 100 Ω RF resistors in the lab.

Table 4.1 gives the measured impedance for the different loads connected to the balun. The reflection coefficient and the input impedance were calculated from the S-parameter response measured at 300 MHz using Equation 4.1 below.

$$Z_{in} = 50 \times \frac{(1 + S_{11})}{(1 - S_{11})} \quad (4.1)$$

This frequency was selected for the modeling of the balun since the NMHAS is supposed to operate around 300 MHz. DC resistance in Table 4.1 is measured using a multimeter.

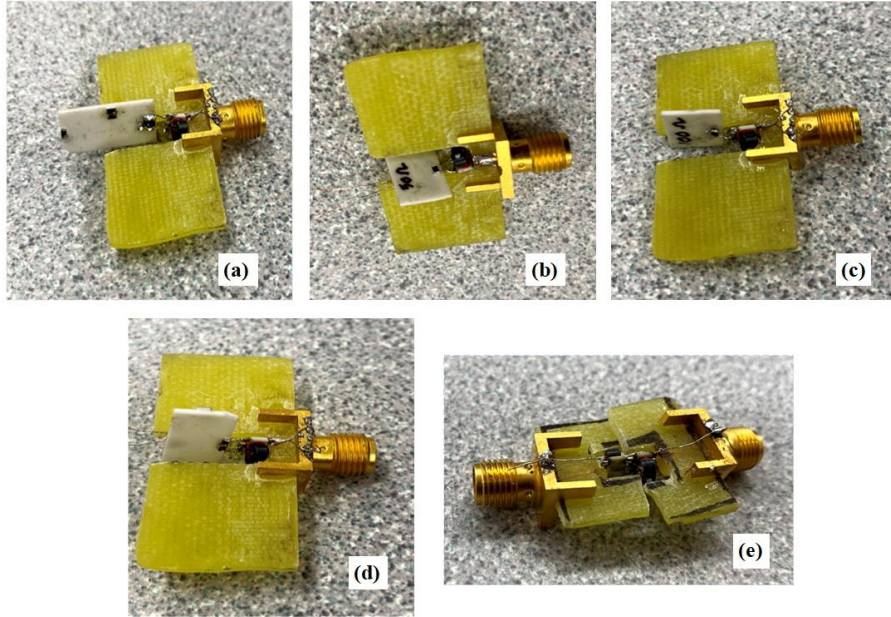


Figure 4.2: Different loads connected to balun: a) 25 Ω ; b.) 50 Ω ; c.) 100 Ω ; d) 150 Ω ; e) baluns connected end to end.

Fixture	DC Resistance [Ω]	Measured S_{11} $ S_{11} , \angle S_{11}$	Measured $\text{Re}(Z_{in})$ [Ω]	Measured $\text{Im}(Z_{in})$ [Ω]
Four 100 Ω resistors connected in parallel	25.6	$ S_{11} = 0.40$ $\angle S_{11} = 97.6$	33.16	31.0
50 Ω	50.2	$ S_{11} = 0.15$ $\angle S_{11} = 57.4$	56.95	15.3
100 Ω	100.1	$ S_{11} = 0.31$ $\angle S_{11} = 27.4$	82.16	-25.8
50 Ω and 100 Ω in series	150.2	$ S_{11} = 0.47$ $\angle S_{11} = 35.4$	85.73	-59.16
Balun to balun connection	N/A	$ S_{11} = 0.29$ $\angle S_{11} = 25.3$ $ S_{22} = 0.29$ $\angle S_{22} = 25.6$	$Z_{11} = 82.60$ $Z_{22} = 82.72$	$X_{11} = 22.93$ $X_{22} = 23.44$

Table 4.1: Measured S_{11} and input impedance for the fixtures shown in Figure 4.2.

4.3 Extraction of Equivalent Network Circuit Components for Parasitics in the Balun Equivalent Fixture

This section uses the measured impedance values from Table 4.1 to network model the balun using a scalar network. The network was selected to model the parasitic capacitance at SMA connector terminal the inductive wire connection between the SMA connector and the balun and the electrical delay imposed by the balun, Tuning tool on ADS and Smith v4.1 [78] were used to adjust the values of L, C and the phase delay to adjust the fitted network to the measured impedance values. Smith v4.1[78] is a Smith Chart based linear circuit simulation program used to design the network of the balun parasitic components. Table 4.2 shows the fitted values of inductances and capacitances for the different loads used. Figure 4.3 shows the resulting balun equivalent circuit.

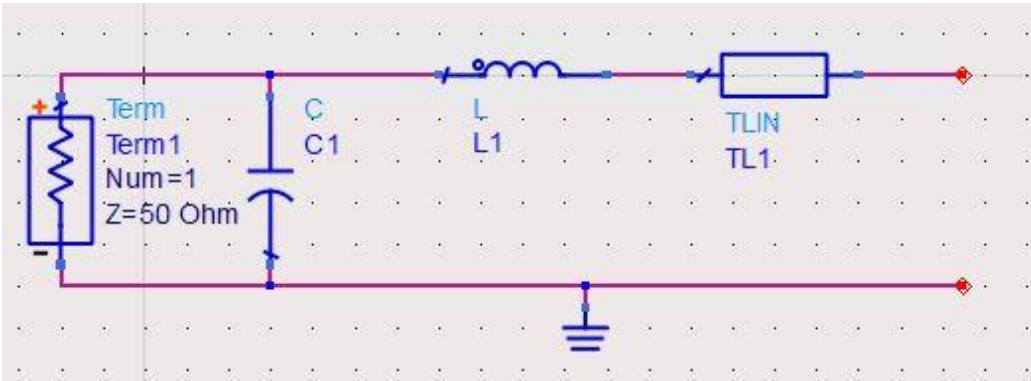


Figure 4.3: Balun equivalent circuit

Case	Load [Ω]	Circuit	L [nH]	C [pF]	Φ [°]	ADS input impedance [Ω]	VNA measured input impedance [Ω]
1	25		13	2.2	10	33.1+j31.3	33.16+j31.0
2	50		13	2.2	10	58.5+j14.0	58.3+j14.8
3	100		16.2	2.1	12	80.5-j25.0	82.1-j25.8
4	150		16.2	2.1	10	80.6-j53.5	85.3-j59.2
5	Balun to balun		13.6	2	22	83.2+j23.5	Port1 : 82.6 + j22.9 Port 2: 82.7+j23.4

Table 4.2: Optimized values of L, C and Φ for different loads

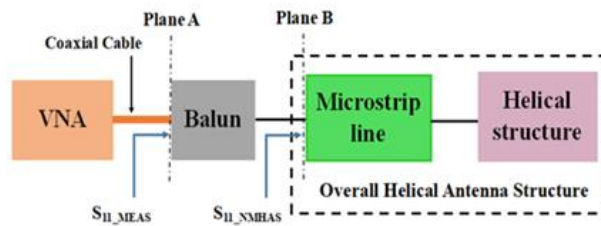
Based on the results presented in Table 4.2 and the balun setup from Figure 4.2a to Figure 4.2e modeled in Table 4.2, the following parasitic modeling values have been adopted, considering that the final implementation of the balun with the NMHAS (Figure 4.4) closely resembles Case 2 in terms of the bonding wire lengths and SMA mounting:

- C = 2.2 pF
- L = 13 nH
- Φ = 10°

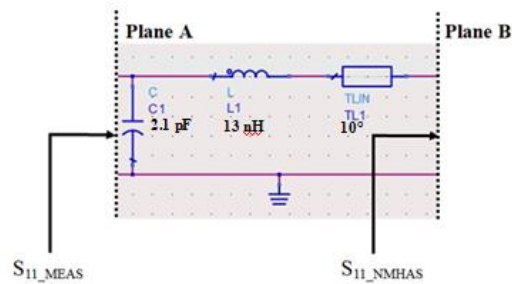


Figure 4.4: NMHAS balun connected at input.

Figure 4.5a shows the block diagram of the experimental setup used for measuring the impedance response of the NMHAS connected to the balun shown in Figure 4.4. The VNA calibration was performed at the end of the connecting coaxial cable, which is referred to as Plane A in Figure 4.5, and thus the measured S_{11} , S_{11_MEAS} , includes the balun.



(a)



(b)

Figure 4.5: a) NMHAS measurement block diagram; b.) Balun equivalent circuit: parameters obtained through measurement and error minimization.

To obtain the input impedance of the antenna structure without the balun (S_{11_NMHAS} in Figure 4.5), the circuit model developed for the balun experimental fixture developed in this section is used.

The impedance at Plane B (as shown in Figure 4.5) is calculated from the measured S-parameter response at Plane A using the circuit components established in the last section and a MATLAB code. The S_{11_NMHAS} (Plane B) is used in Chapter 5 for the discussion of NMHAS.

The MATLAB code (APPENDIX D) calculates the impedance from the measured S_{11} at Plane A (S_{11_MEAS}) using Equation 4.1. Then the equivalent impedance of the capacitor (C), inductor (L) and calculated impedance at Plane A is determined. Then S_{11} is calculated using this equivalent impedance and the phase Φ is added to the phase of the calculated S_{11} making the resultant S_{11_NMHAS} .

4.4 NMHAS Impedance Response Variation due to Fabrication Procedure

4.4.1 Comparison of Four Similarly Fabricated Helices

This section investigates variations of the structure response when 4 similar helices are connected at the end of the same two-inch microstrip line using the structure shown in Figure 4.4. Figure 4.6 depicts the four similar helices connected to the same two-inch microstrip line and balun structure. The S_{11} measurements at Plane A (Figure 4.5) were taken in the anechoic chamber and translated to Plane B, as discussed in the previous section. Figure 4.7 compares the S-parameter and impedance responses at Plane B for the four helices connected at the end of the same microstrip line.

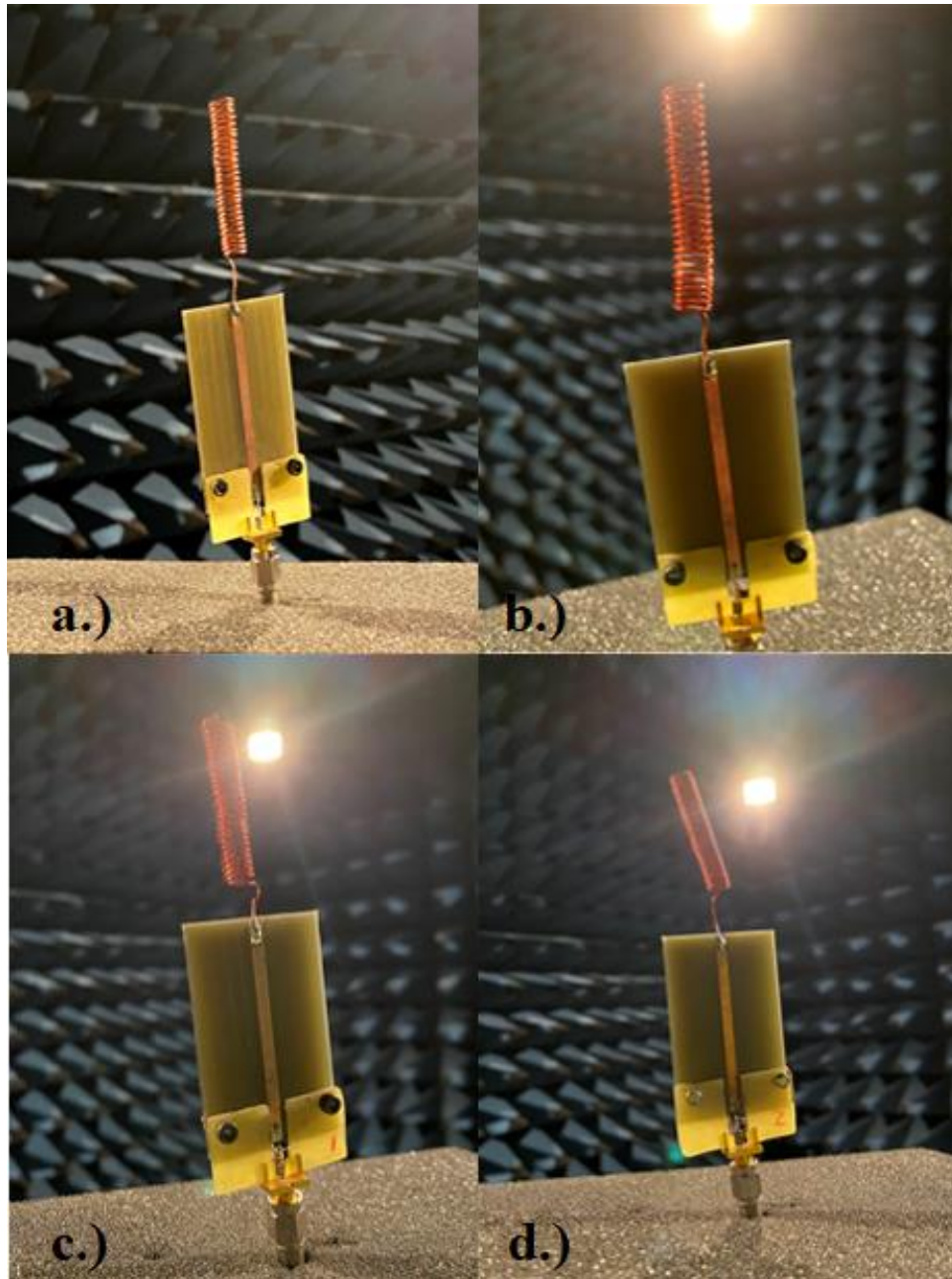


Figure 4.6: Four similarly wound helices connected to same two-inch microstrip line: (a.) Helix 1; (b.) Helix 2; (c.) Helix 3; and (d.) Helix 4.

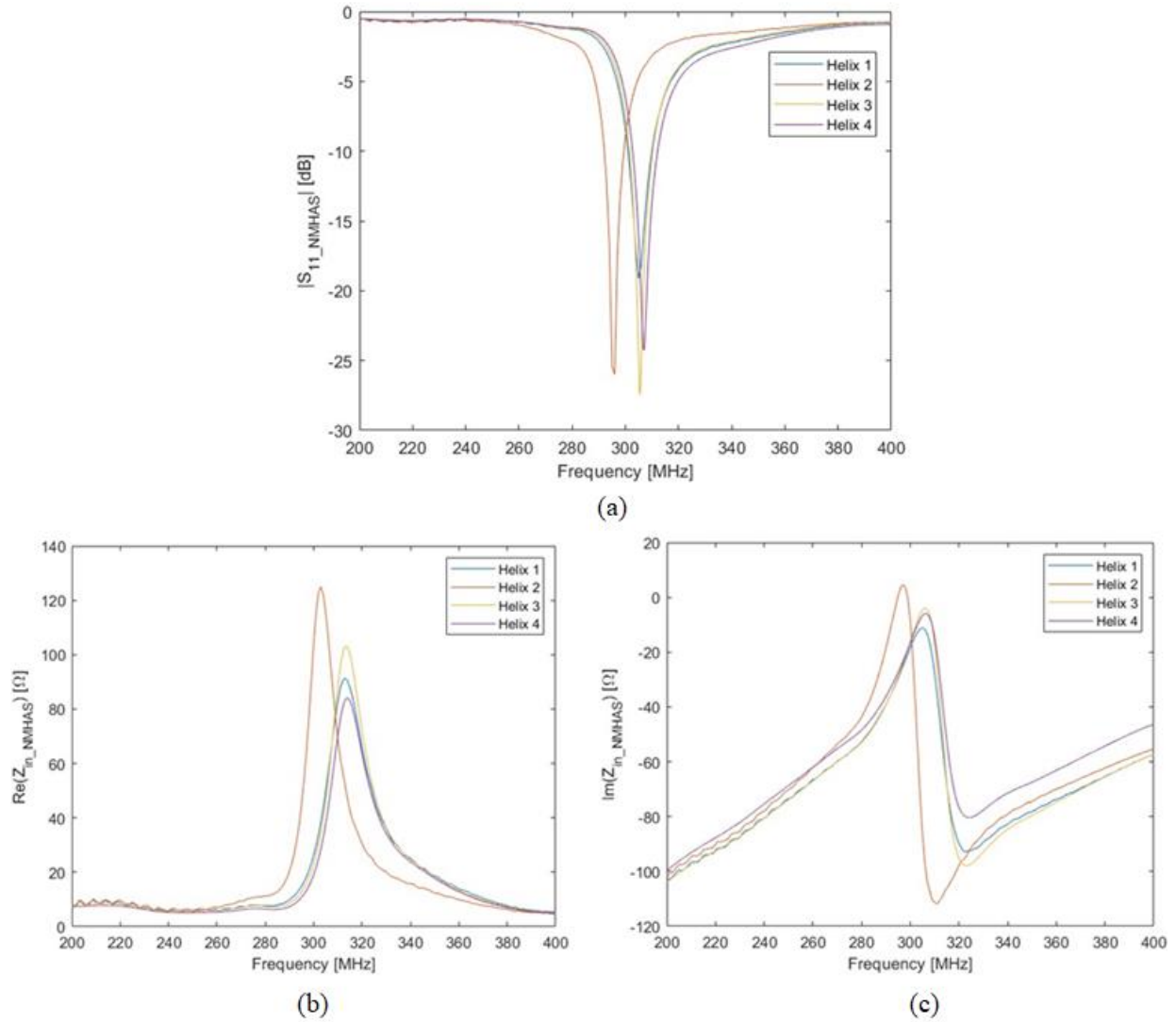


Figure 4.7: Frequency response of four similarly wound helices connected to same two-inch microstrip line: a) $|S_{11_NMHAS}|$ [dB]; b) $\text{Re}(Z_{in_NMHAS})$ [Ω]; c) $\text{Im}(Z_{in_NMHAS})$ [Ω].

Conferring the simulation results reported in Chapter 3, the resonant frequency of the structure is more sensitive to changes in the radius of the helix. From Figure 4.7, it can be observed that there is variation of around 3% in the resonant frequency for the similarly fabricated helices. Based on the measured Δf of 11 MHz and the sensitivity $\Delta D_h / \Delta f$ of 0.016 simulated in Chapter 3, one would expect a ΔD_h of 0.176 mm, which is under the fabrication uncertainty associated with the process of winding the helices by hand. The change in response among the different helices can be

attributed to fabrication variations in dimensions and helix positioning with respect to the microstrip line.

4.4.2 Comparison of Balun Jigs

This section compares the response of two similar balun Jigs 1 and 2. The same helix is connected at the end of two-inch microstrip line for both the balun Jigs 1 and 2 shown in Figure 4.8. The S-parameter measurements are performed in the anechoic chamber. Figure 4.9 shows the S-parameter response calculated at Plane B.

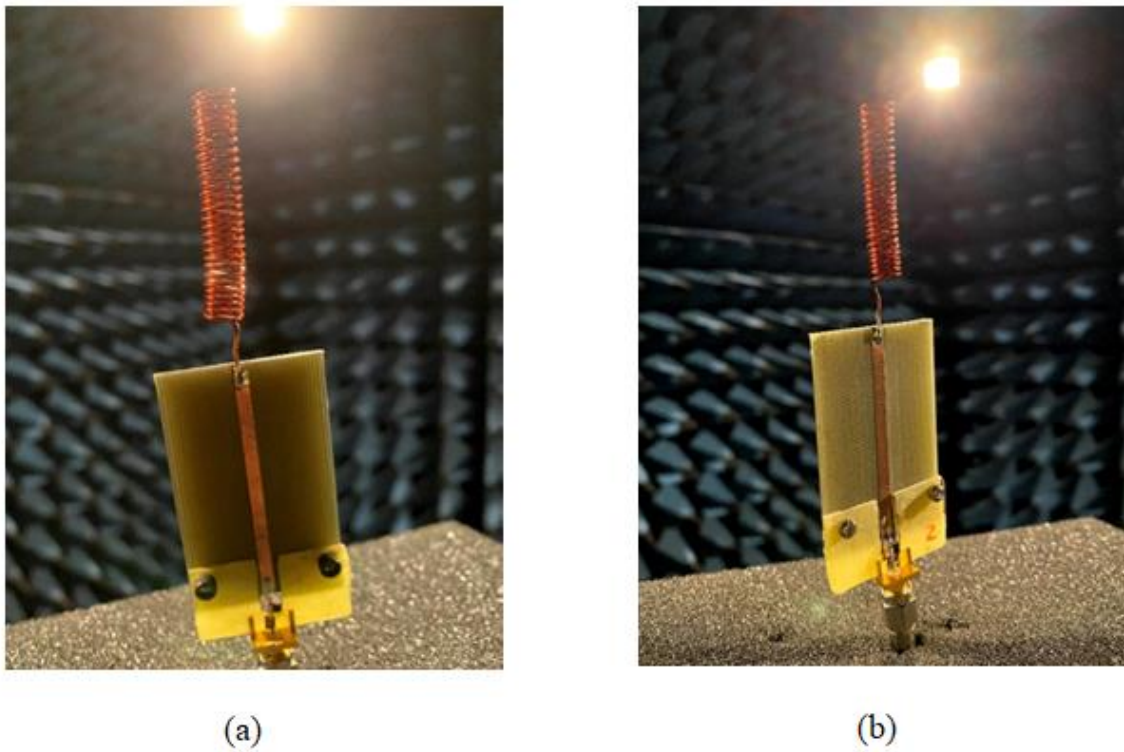


Figure 4.8: Two-inch microstrip line connected to: a.) Balun Jig 1; b.) Balun Jig 2.

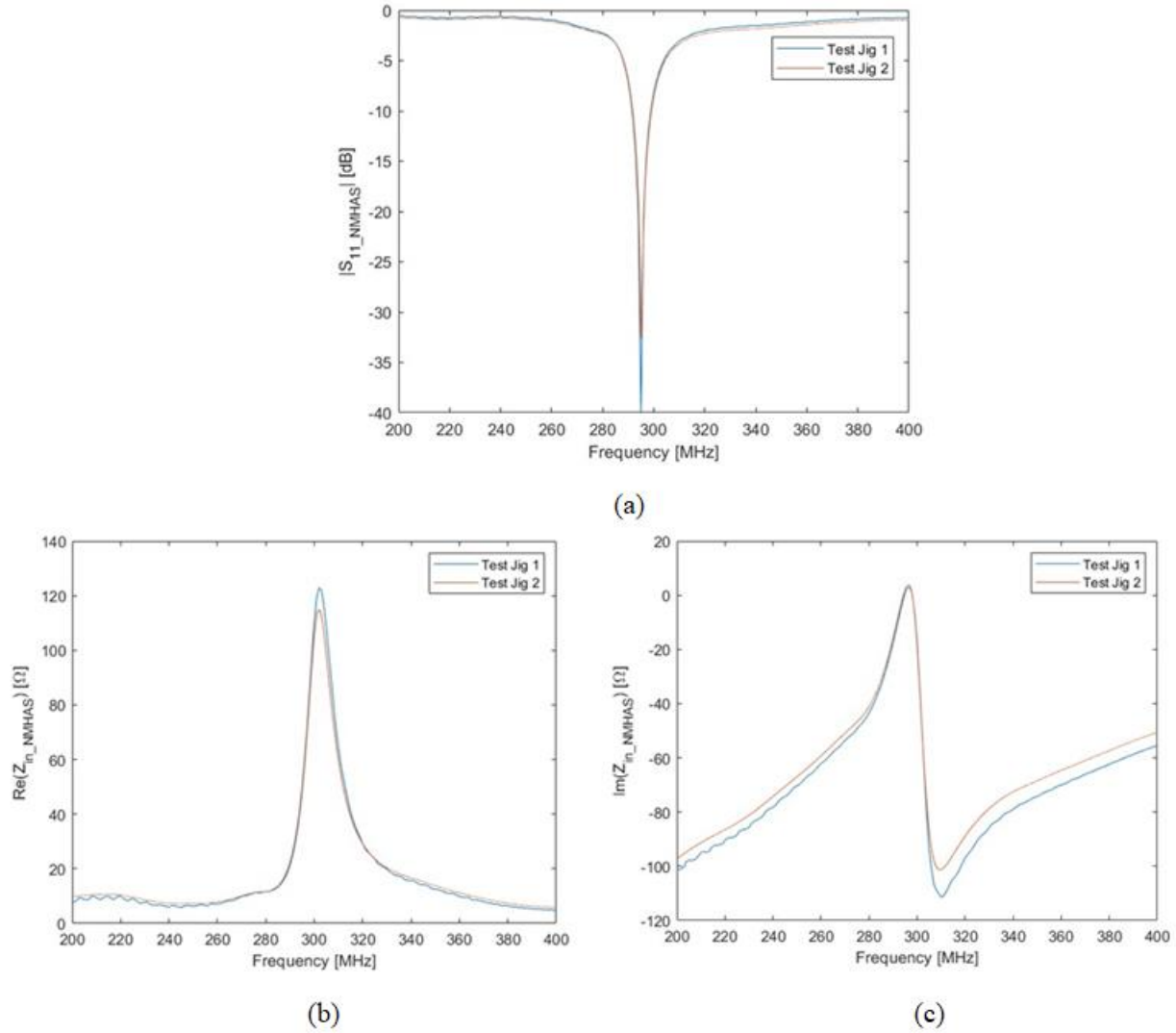


Figure 4.9: S-parameter response of balun Jigs 1 and 2 connected to same helix at the end of two-inch microstrip line: a) $|S_{11_NMHAS}|$ [dB]; b) $\text{Re}(Z_{in_NMHAS})$ [Ω]; c) $\text{Im}(Z_{in_NMHAS})$ [Ω]

From Figure 4.9 it can be observed that the resonant frequency for Jig 1 and Jig 2 is 302MHz and 302.2MHz respectively. The variation in resonant frequency is 0.06%. Therefore, the two fabricated jigs perform very similarly. These two balun jigs were used in Chapter 5 to measure the transmission response of two similar NMHAS.

4.5 Implementation of Impedance Matching Network

An LC impedance matching circuit was used between the balun and the SMA connector to match the measured NMHAS impedance at Plane A to 50Ω . This matching circuit was calculated based on full two port S-parameter measurements of two NMHAS facing each other at 44 inches. The reflection coefficients at both ports were used to calculate the input impedances at ports 1 and 2, which were then matched to 50Ω . Further, the impedance matching circuits were optimized using ADS Tuning tool for the LC circuits based on the measured S-parameter shown as SNP component in Figure 4.10.

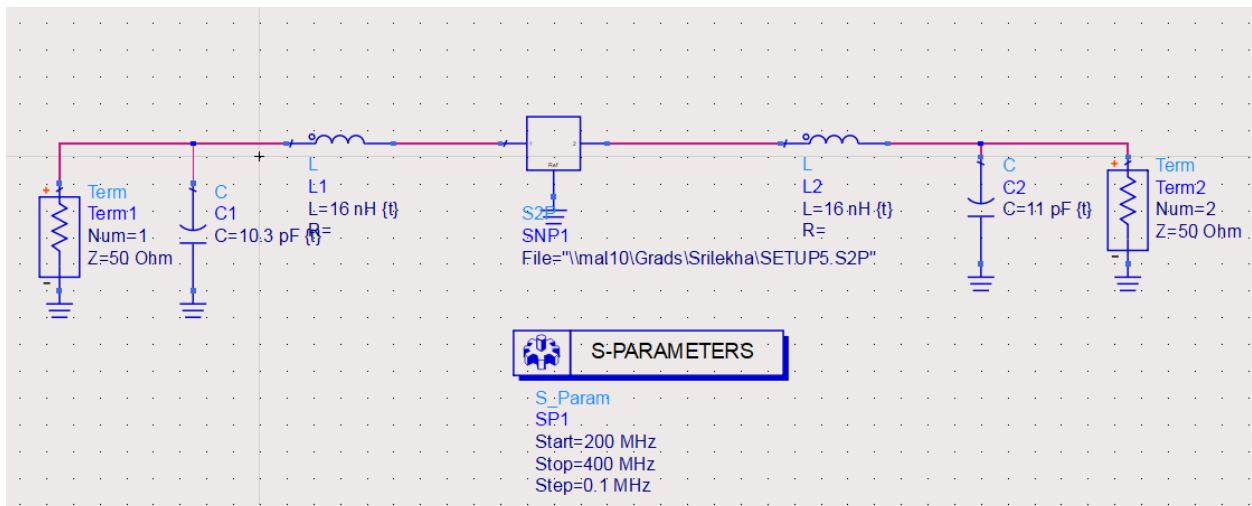


Figure 4.10: Impedance matching network implemented on ADS.

Figure 4.11 shows the fabricated FR-4 board outline to house the inductor and the capacitor used to match one of the NMHAS. The top and bottom copper patches represented in black in the figure act as ground, while the gaps in the center line were designed to allow the soldering of the components to be placed in series. The length of the center line patches connected to each other with copper tape soldered between them was enough to achieve the targeted inductance values shown in Figure 4.10, For Structure 1, a variable capacitor (trimmer) of capacitance ranging from

8.5pF to 40pF was used. For Structure 2, a variable capacitor of capacitance ranging from 3pF to 20pF was used. The trimmers were connected between the center conductor and the ground, close to the SMA connectors. The trimmer capacitances for both NMHASs were adjusted to reduce SWR around the 300MHz resonant frequency. The response of the structures with the impedance matching network is discussed in Chapter 5.

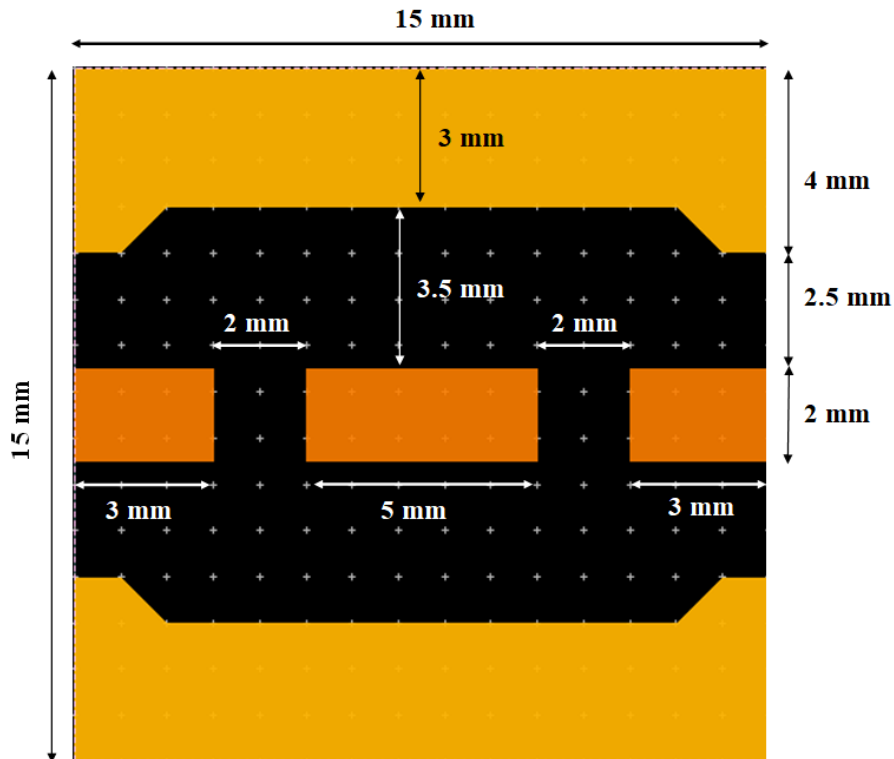


Figure 4.11: FR-4 board outline fabricated to hold the LC matching circuit.

4.6 Conclusions

This chapter discusses the NMHAS fabrication and preparation for the testing reported in Chapter 5. A balun was introduced between the SMA connector and NMHAS in an attempt to mitigate the participation of the coaxial cable shield in the radiation of the NMHAS. A balun network model was defined and optimized using ADS. The impedance at the input of the microstrip was calculated by transferring the measured impedance at input of the balun.

The NMHAS impedance response variation was reported due to the fabrication procedure by observing the response of four similarly fabricated helices connected to the same two-inch microstrip line and it was observed that the variation in input impedance and resonant frequency was due to changes in diameter and spacing of the helix when wounding using the screw. The NMHAS impedance response connected to two similar balun jigs was reported and it was observed that both the fabricated jigs perform consistently.

An LC impedance matching network was modeled and optimized with the aid of ADS to match the measured NMHAS impedance at Plane A to 50Ω . The values of L and C are optimized by using the measured NMHAS S-parameter response. The response of the NMHAS with impedance matching network will be discussed in Chapter 5.

CHAPTER 5. NMHAS MEASUREMENTS AND ANALYSIS

In this chapter measured responses of the NMHAS are compared with the simulation results presented in Chapter 3. The NMHAS measurements utilize the different experimental setups and techniques discussed in Chapter 4. The effect of orientation of helix with respect to the microstrip line ground plane on the response of the NMHAS is investigated. The transmission measurements of two similar NMHAS with and without the presence of matching network is also discussed.

5.1 Experimental Setups

As discussed in previous chapters, the impedance and radiation properties of the NMHAS are dependent on the helical structure geometry and on the neighboring metallic plane which serves as a ground plane. To confirm that the laboratory set up was not compromising the response of the antenna structure, the measurements were performed in two different laboratory setups: a laboratory test jig (Figure 5.1a) and an anechoic chamber (Figure 5.1b).

Figure 5.1a shows two similar NMHAS assembled on an antenna mounting fixture and connected to the VNA (Keysight Model E5061B) through coaxial cables. Figure 5.1b displays NMHAS mounted on antenna support fixture on a tripod inside the anechoic chamber and connected to the VNA (Model N5230C) through a coaxial cable.

The VNAs were calibrated before recording the measurements using a calibration kit consisting of standard electrical passive devices: short, open, load and through, at the end of the connecting coaxial cables.

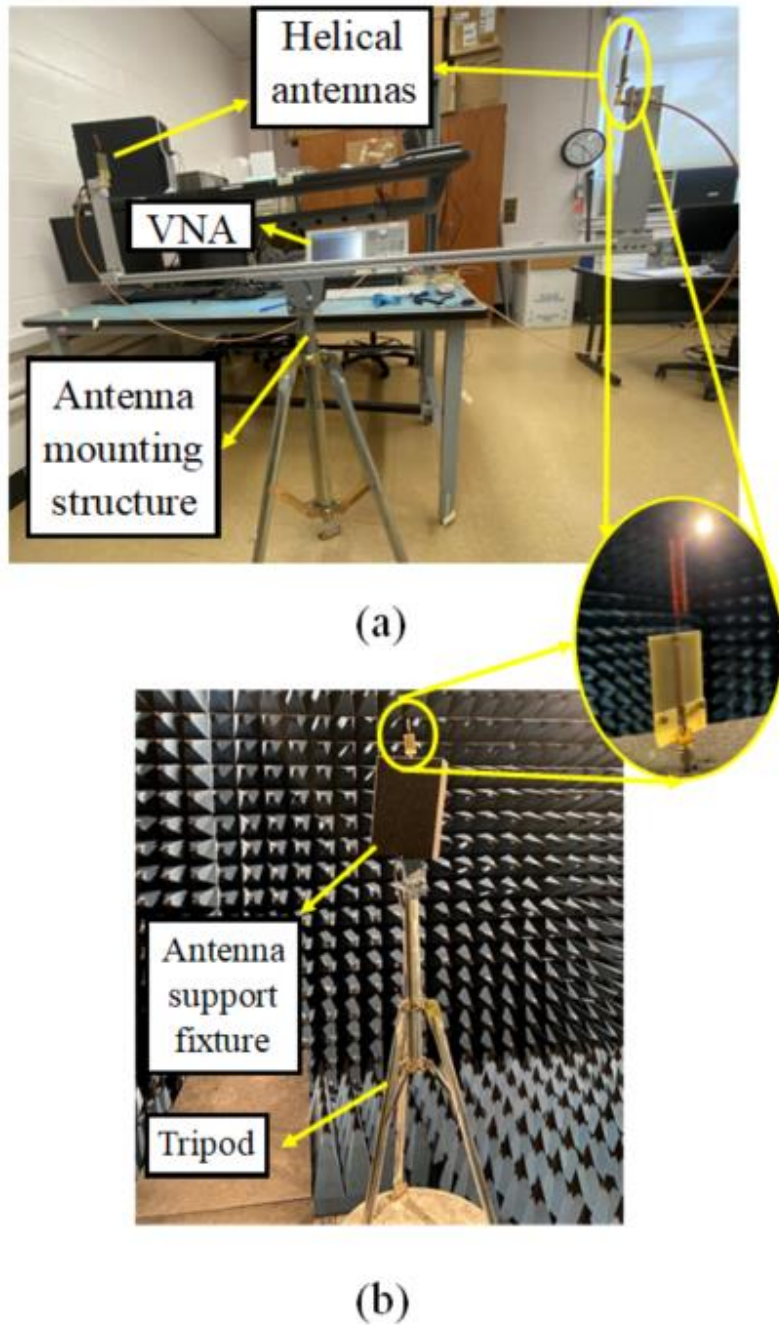


Figure 5.1: Test setups used: a.) microwave engineering lab test bench; b.) anechoic chamber.

5.2 Measurements in Laboratory Setup

The measured NMHAS S_{11} and respective impedance response in the laboratory setup of Figure 5.1a utilizing the VNA Model E5061B (Agilent, CA, USA) is shown in Figure 5.2. The solid line

represents the actual measurement at Plane A discussed in Chapter 4 (Figure 4.5), whereas the dashed line shows the NMHAS impedance transferred to Plane B (Figure 4.5).

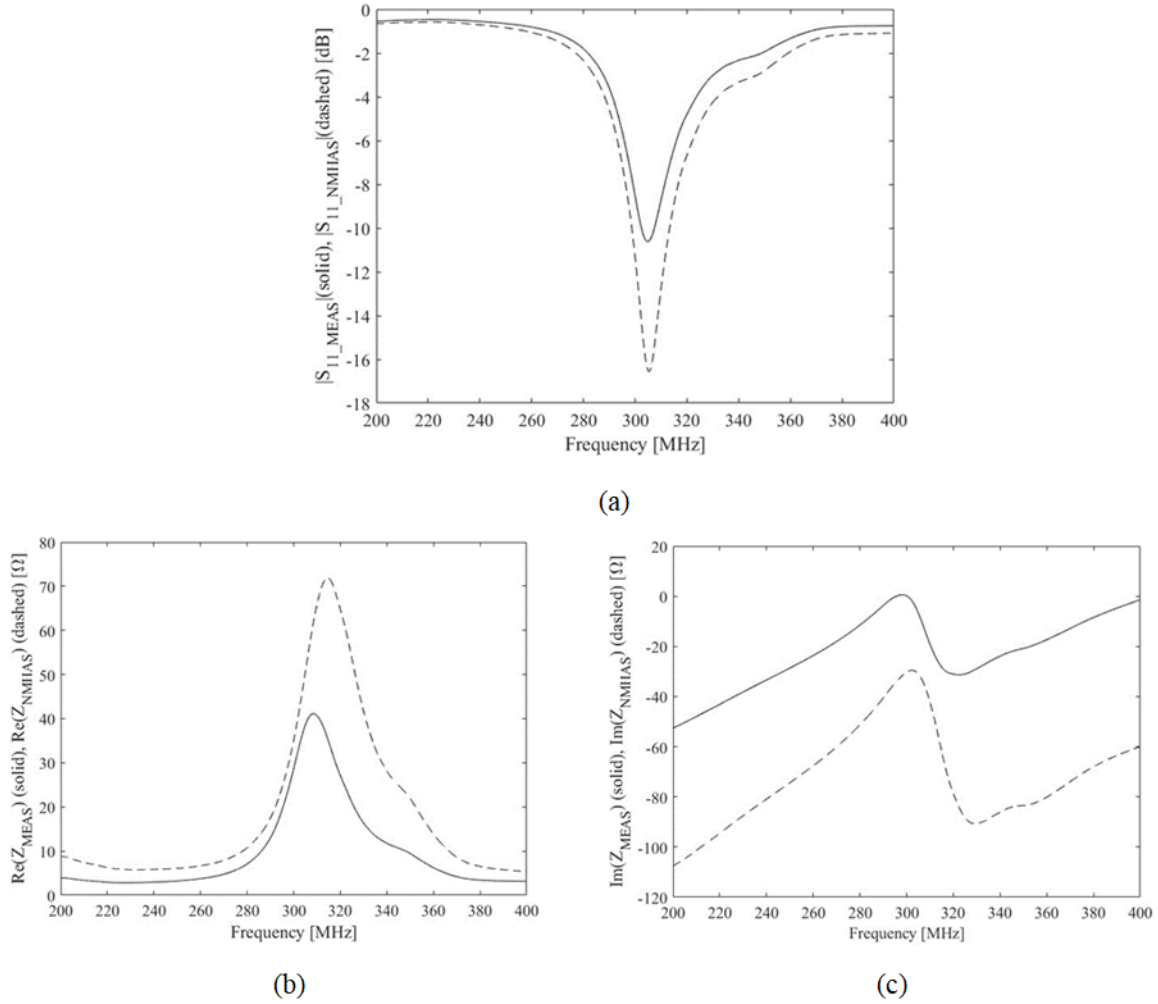


Figure 5.2: Measured S_{11} , S_{11_MEAS} utilizing the measurement setup of Figure 5.1a at the balun input-plane A (solid line) and translated S_{11} , S_{11_NMHAS} , at the input of the integrated microstrip and helical structure input-plane B (dashed line) displayed as: a.) $|S_{11}|$ [dB]; b.) real part of the impedance [Ω]; c.) imaginary part of the impedance [Ω].

From Figure 5.2 it can be observed that the input impedance of NMHAS changes significantly after taking into account the balun and the parasitics, with the real and imaginary parts of the impedance at resonance changing by 73% and 300% respectively, and the resonant frequency increased by 2%.

5.3 Measurements in Anechoic Chamber

This section presents the NMHAS S_{11} measurements taken at the University of Maine anechoic chamber (Figure 5.1b). Figure 5.3 shows the measured S_{11} and respective impedance response of the NMHAS. Consistent with the measurements reported in the previous section, the input impedance of the NMHAS changes significantly after taking into account the balun and the parasitics, with the real and imaginary parts of the impedance at resonance changing by 50% and 300% respectively, and the resonant frequency increased by 1.4%.

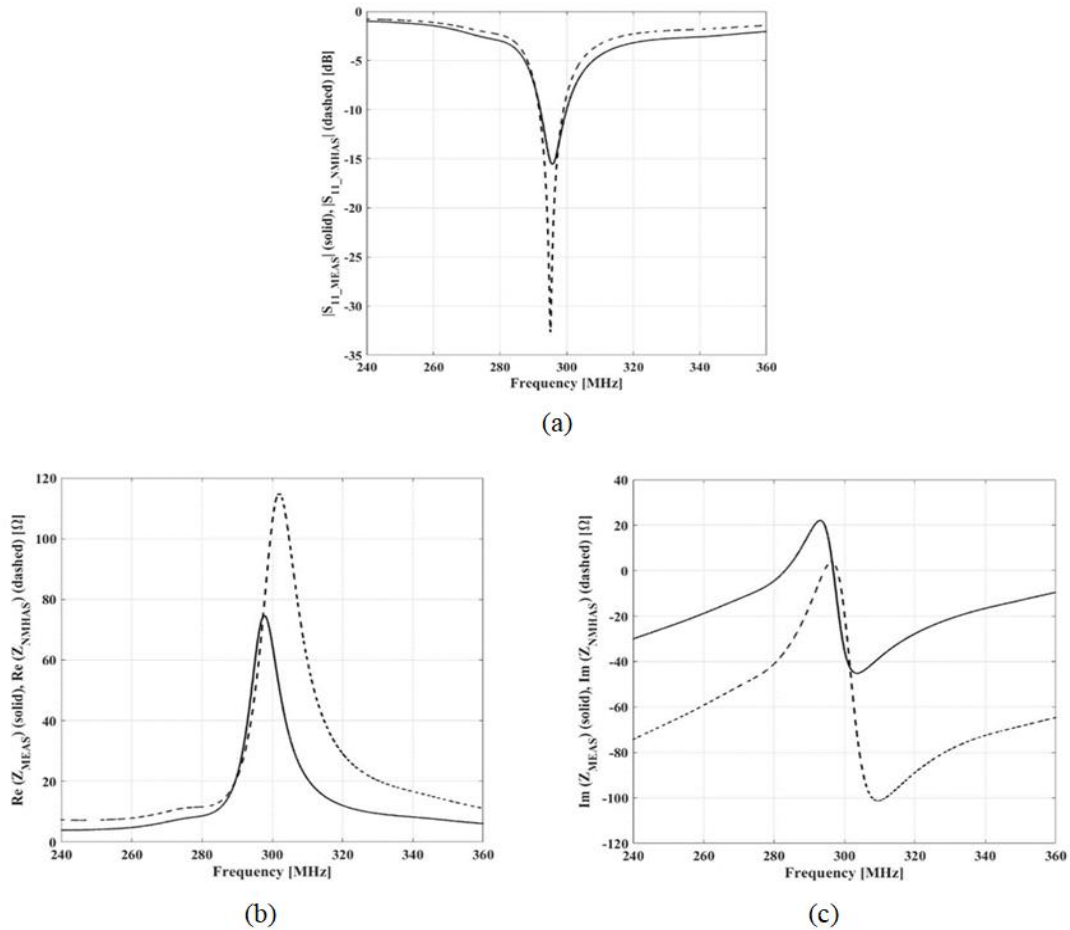


Figure 5.3: Measured S_{11} , S_{11_MEAS} utilizing the measurement setup of Figure 5.1b at the balun input-plane A (solid line) and translated S_{11} , S_{11_NMHAS} , at the input of the integrated microstrip and helical structure input-plane B (dashed line) displayed as: a.) $|S_{11}|$ [dB]; b.) real part of the impedance [Ω]; c.) imaginary part of the impedance [Ω].

5.4 Comparing Measurements using the Laboratory Fixture and the Anechoic Chamber

Figure 5.4 compares the impedance responses of NMHAS measured using the laboratory fixture and the anechoic chamber. The solid line represents the response as measured using the laboratory fixture and the dashed line represents the response as measured in the anechoic chamber. The responses shown in Figure 5.4 are the NMHAS responses at plane B, S_{11_NMHAS} and Z_{in_NMHAS} (Figure 4.5), that is after removing the balun and parasitics effects.

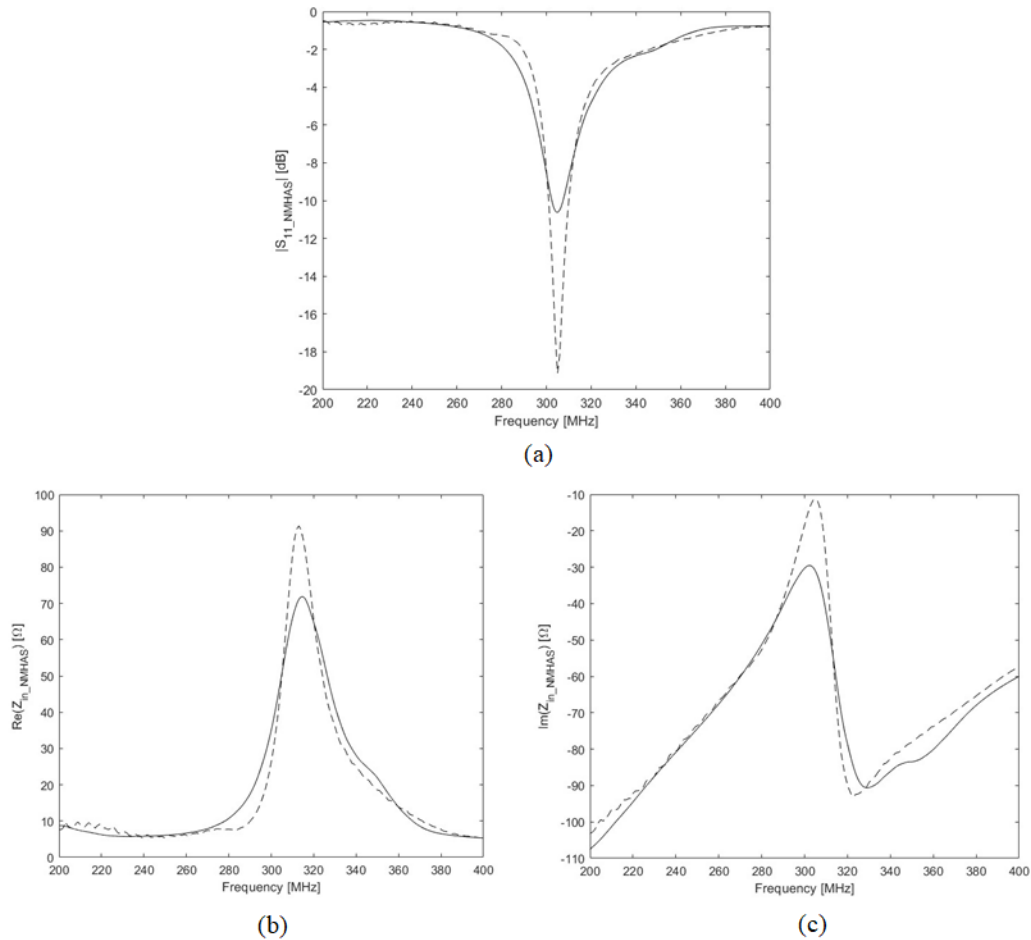


Figure 5.4: Frequency response of NMHAS as measured using laboratory fixture (solid) and in anechoic chamber (dashed) : a) $|S_{11_NMHAS}|$ [dB]; b) real part of impedance [Ω]; c) imaginary part of impedance [Ω]

As can be seen from Figure 5.4, the discrepancy in the resonant frequency between the measurements done in the laboratory fixture and the anechoic chamber is only 0.5%, but the real part and imaginary part of input impedance at resonance change by -23% and 20% respectively in the laboratory fixture when compared to the measurement in the anechoic chamber. This change in impedance is most likely due to the influence of the laboratory environment, where the different metallic structures present in laboratory contribute to the antenna radiation performance and more significantly change the NMHAS impedance.

5.5 Comparison of Measurements and Simulation:

This section discusses the discrepancies between the NMHAS simulations (using HFSS and WIPL-D) and the measured impedance responses using the lab fixture and the anechoic chamber. The curves displayed in this section refer to S_{11_NMHAS} and Z_{in_NMHAS} , that is at Plane B (Figure 4.5) after accounting for the balun fixture parasitics discussed in Chapter 4.

Figure 5.5 shows the measured and simulated $|S_{11}|$ response of the NMHAS and Figure 5.6, Figure 5.7 show the real and imaginary part of measured and simulated NMHAS response respectively. The right y-axis in Figure 5.6 and Figure 5.8 represents the measured impedance responses transformed to Plane B while the left y-axis represents simulated impedance response.

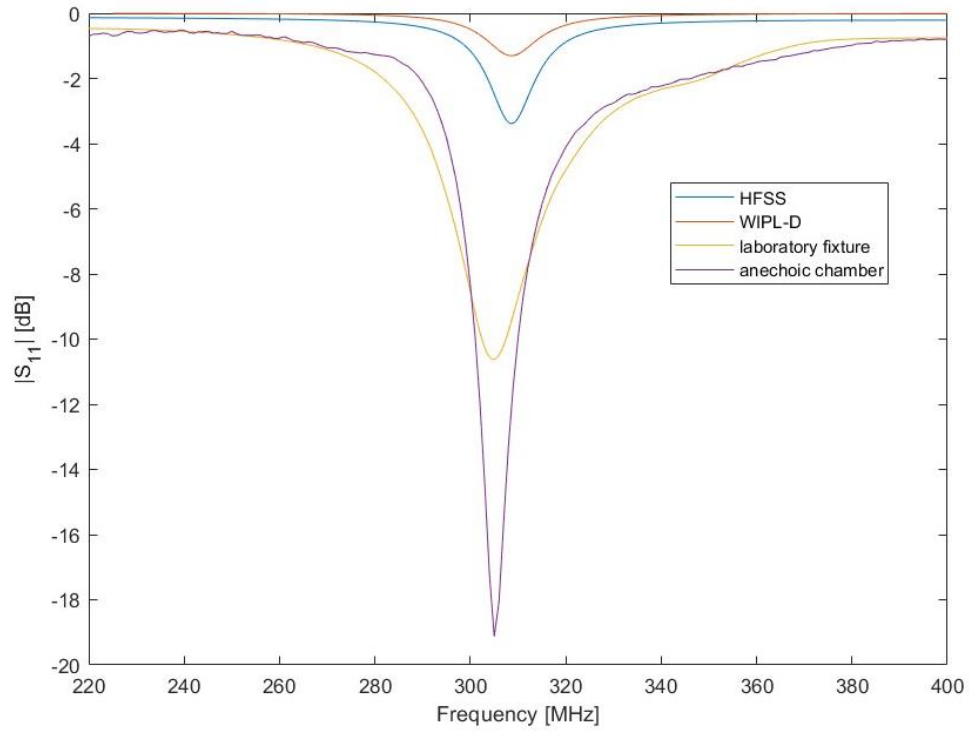


Figure 5.5: Simulated and measured $|S_{11}|$ response of NMHAS.

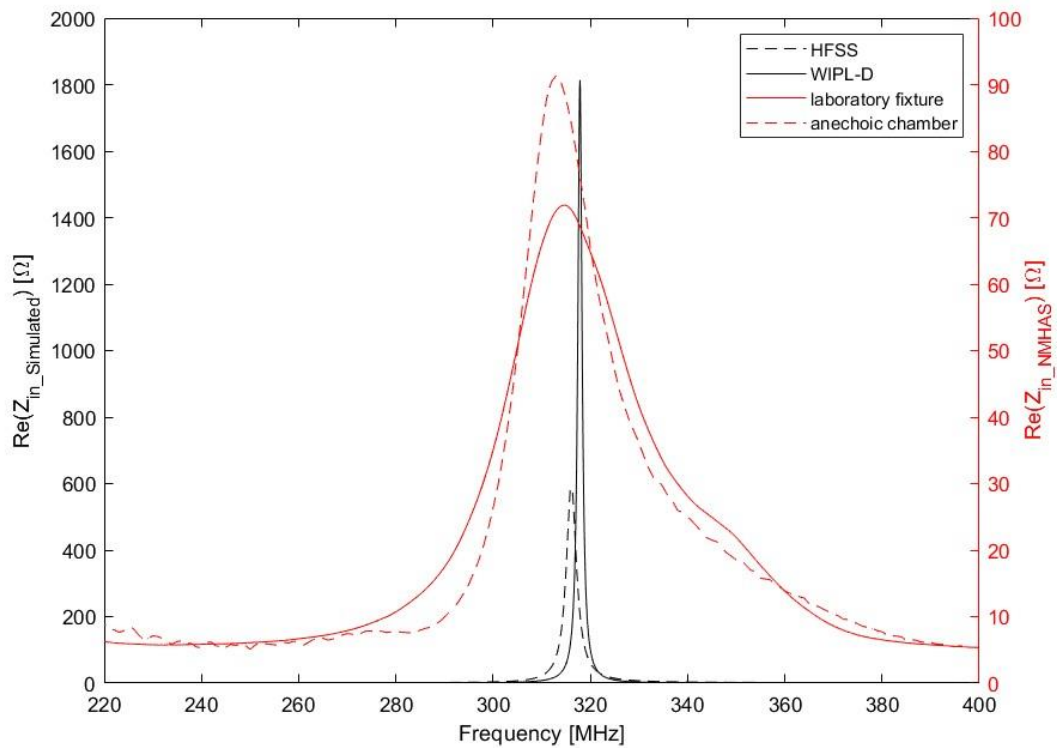


Figure 5.6: Real part of impedance response of simulated and measured NMHAS.

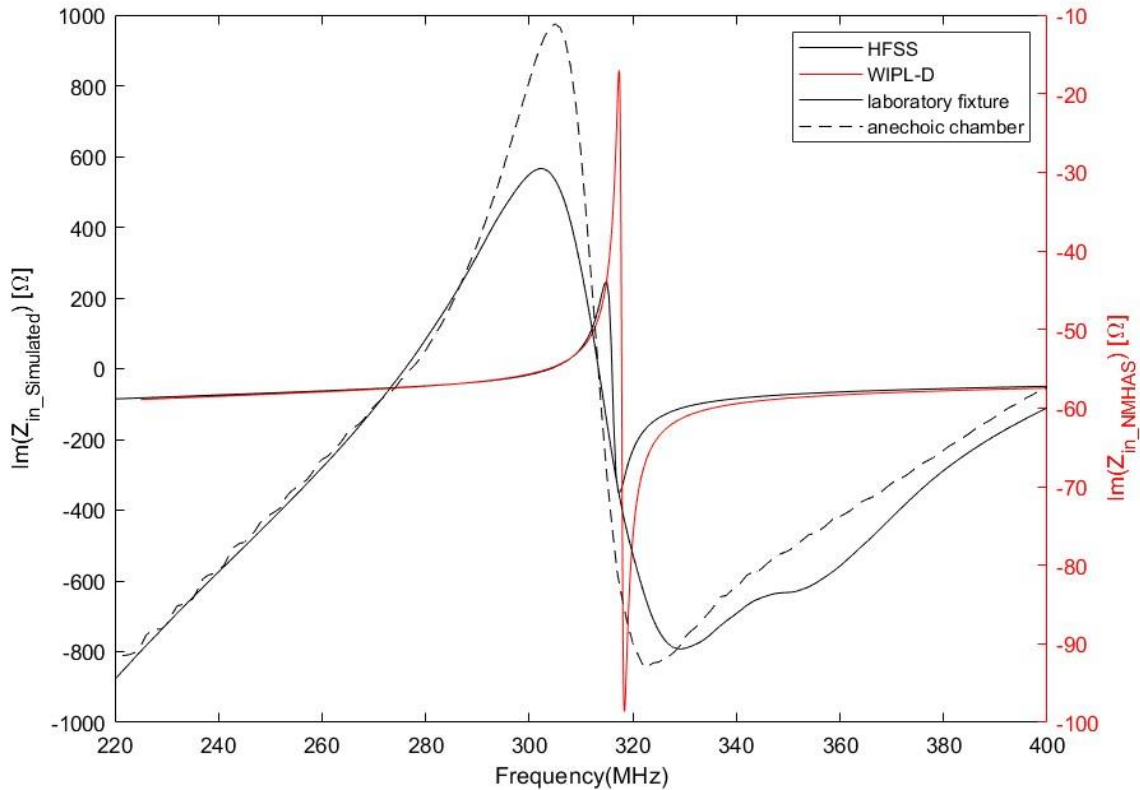


Figure 5.7: Imaginary part of impedance response of simulated and measured NMHAS.

The NMHAS resonant frequency, the measured value is 4.8% lower than the simulated one by HFSS, thus revealing a good agreement. However, comparison between simulated and measured curves (Figure 5.5, Figure 5.6 and Figure 5.7) reveals that the NMHAS modeling using WIPL-D and HFSS needs to be improved for impedance due to significant differences.

5.6 Helix Structure Oriented in Different Directions

This section addresses the effect of orientation of helix with respect to the microstrip line on the response of the NMHAS. The helix was oriented around X, Y, +Z and -Z direction with respect to the microstrip line as shown in Figure 5.8 and the measurements were performed in the anechoic chamber (Figure 5.1b).

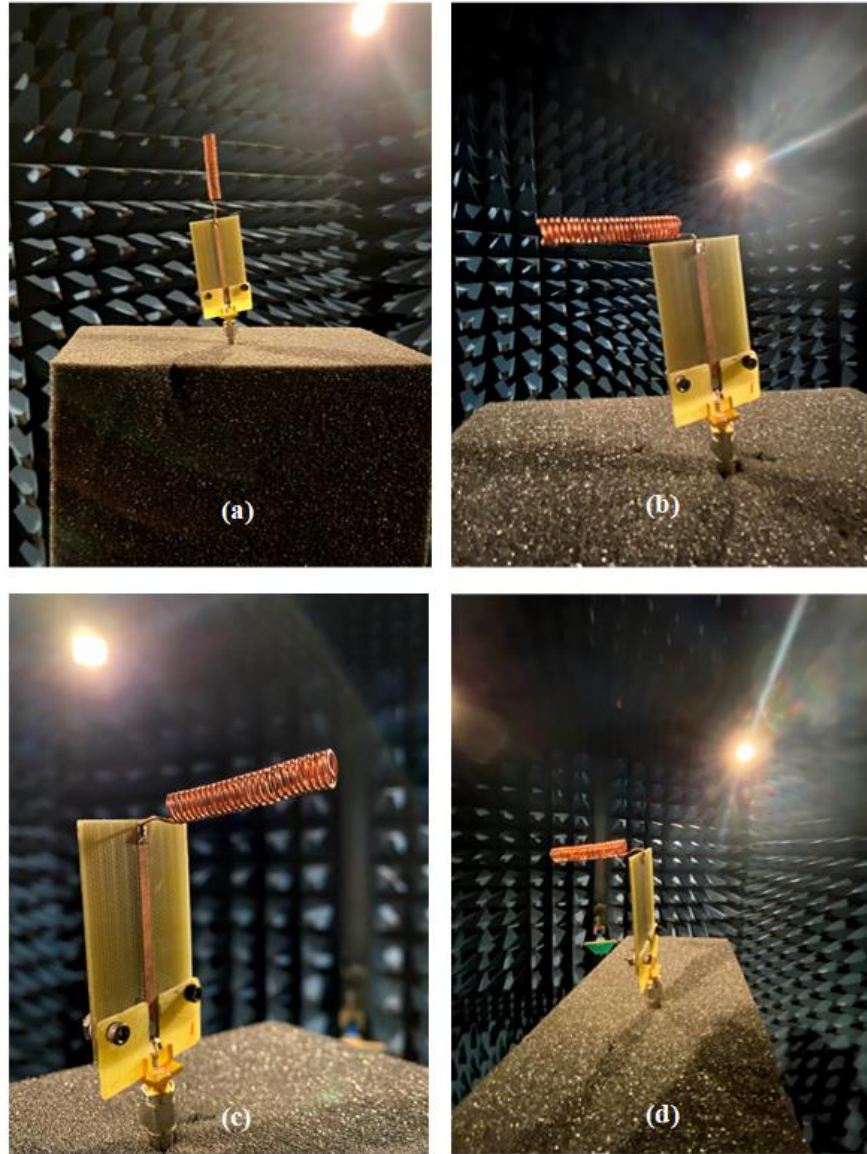


Figure 5.8: Helix oriented along different directions with respect to microstrip line: a.) X-direction; b.) Y-direction; c.) +Z-direction; d) -Z-direction.

Figure 5.9 shows the $|S_{11_NMHAS}|$, Figure 5.10, Figure 5.11 show the real and imaginary part of Z_{NMHAS} when the helical structure connected to the microstrip is positioned along the X-direction, the +Z-direction, the -Z-direction, or the Y-direction, measured in the anechoic chamber (Figure 5.1b) at Plane B (Figure 4.5).

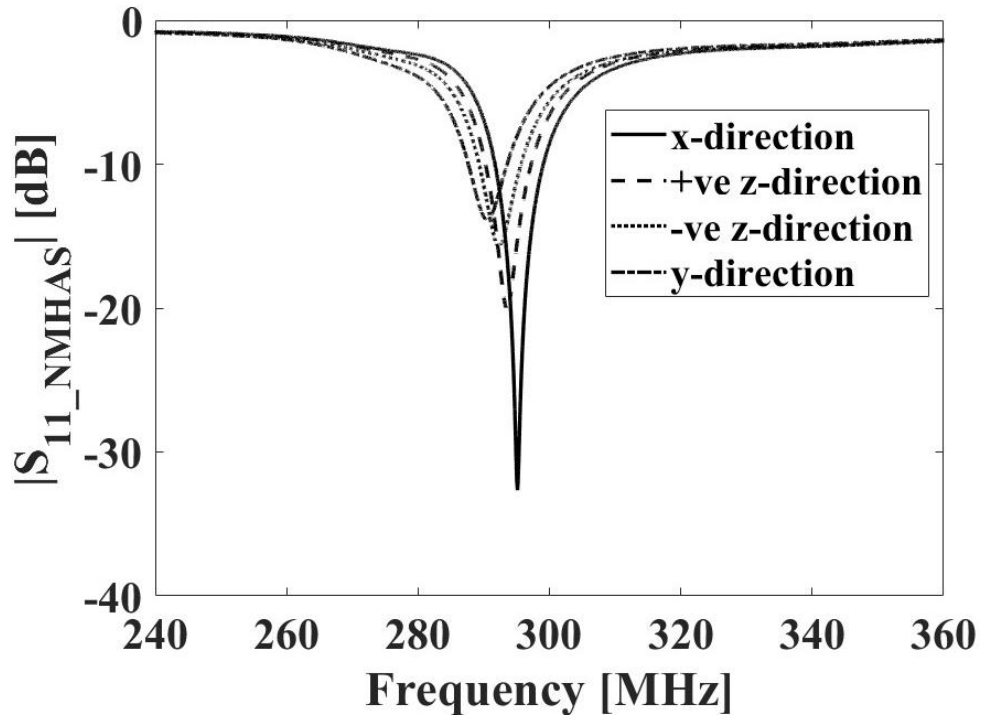


Figure 5.9: S_{11_NMHAS} (at reference Plane B) for the NMHAS structure connected along X-direction, +Z-direction, -Z-direction and Y-direction.

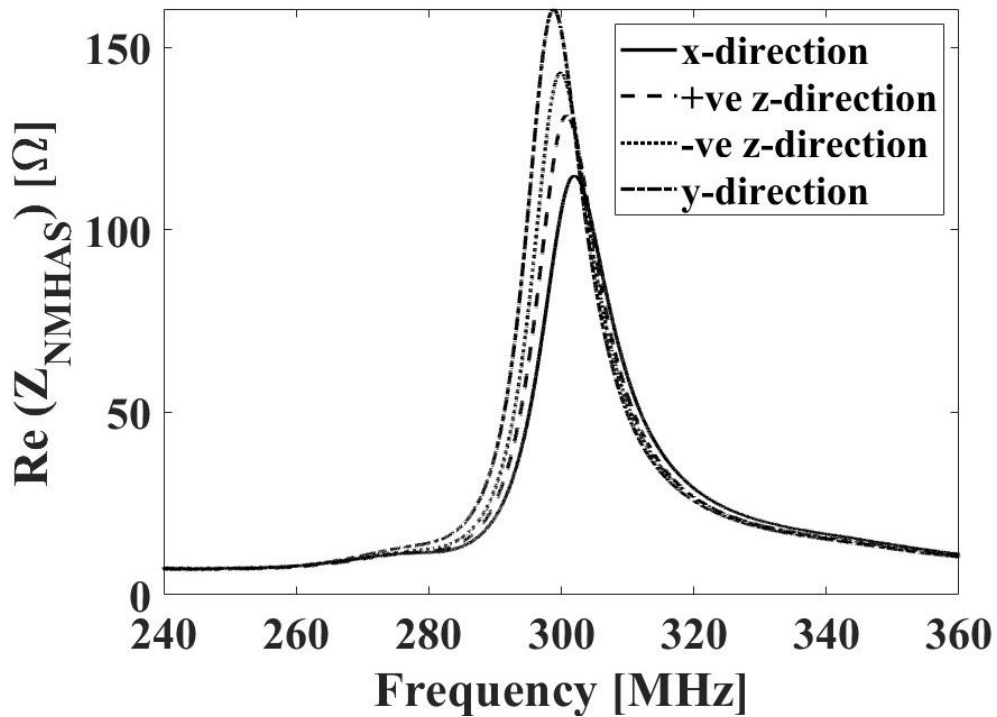


Figure 5.10: Real part of Z_{NMHAS} (at reference Plane B) for the NMHAS structure connected along X-direction, +Z-direction, -Z-direction and Y-direction.

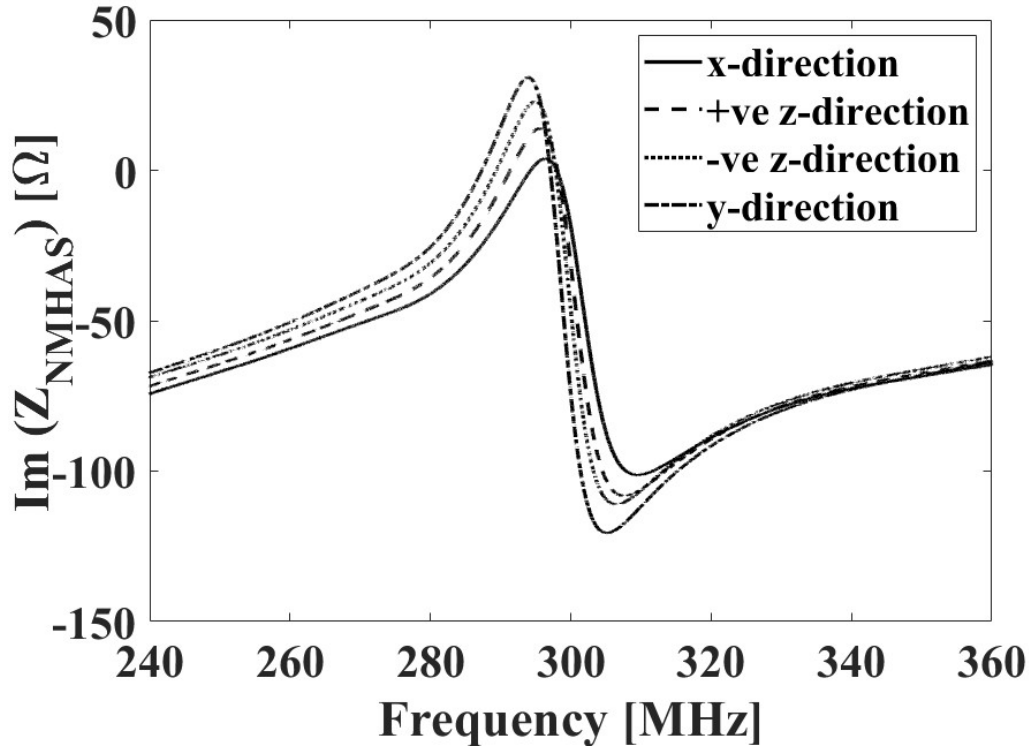


Figure 5.11: Imaginary part of Z_{NMHAS} (at reference Plane B) for the NMHAS structure connected along X-direction, +Z-direction, -Z-direction and Y-direction.

The overall NMHAS resonant frequency of operation varied only about 1% maximum in changing the orientation of the helical structure among different directions. At resonance, the $\text{Re}(Z_{NMHAS})$, however, varied about 28%, from 114.3Ω when the helical structure was aligned along the X-direction to 159.6Ω when aligned along the Y-direction, as shown in Figure 5.9. Around resonance, the imaginary part $\text{Im}(Z_{NMHAS})$ remained around $-j60\Omega$, as can be observed from Figure 5.11. As can be seen from Figure 5.9, Figure 5.10 and Figure 5.11, the variation in impedance due to the different mounting of the helix with respect to the ground plane results in the observed different frequency selectivity in the 50Ω measuring system.

5.7 Full S-parameter Measurements for two NMHAS Facing Each Other

The transmission between two similar NMHAS (Helix 3 and Helix 4 connected to each respective microstrip line Figure 4.6) fabricated with the helical structure positioned along the X-direction and including baluns and the respective impedances were measured using the laboratory structure shown in Figure 5.1a. This section presents transmission measurements between two similar NMHAS when the distance between them is varied. The measurements reported in this section include NMHAS with and without impedance matching circuit.

5.7.1 S-parameter Measurements Without Impedance Matching Network

This section presents the transmission and impedance response of two similar NMHAS without the presence of an impedance matching circuit. The NMHAS were spaced facing each other at several distances.

5.7.1.1 NMHAS placed 44 inches apart

This section presents the transmission and impedance response of the antenna structures spaced 44 inches apart. Figure 5.12 shows the experimental setup of NMHAS assembled on the antenna mounting structure in the microwave laboratory and spaced 44 inches apart.



Figure 5.12: NMHAS mounted on antenna mounting structure and spaced 44 inches apart.

Figure 5.13 shows the impedance and transmission responses of NMHAS obtained at Plane A (Figure 4.5) mounted as shown in Figure 5.12 based on the full two-port S-parameter measurements. Figure 5.13b plots $|S_{21_MEAS}|$ for the two NMHAS mounted 44 inches apart. As can be seen from Figure 5.13b the measured minimum transmission loss for the two identical antennas is about 21dB around 319 MHz.

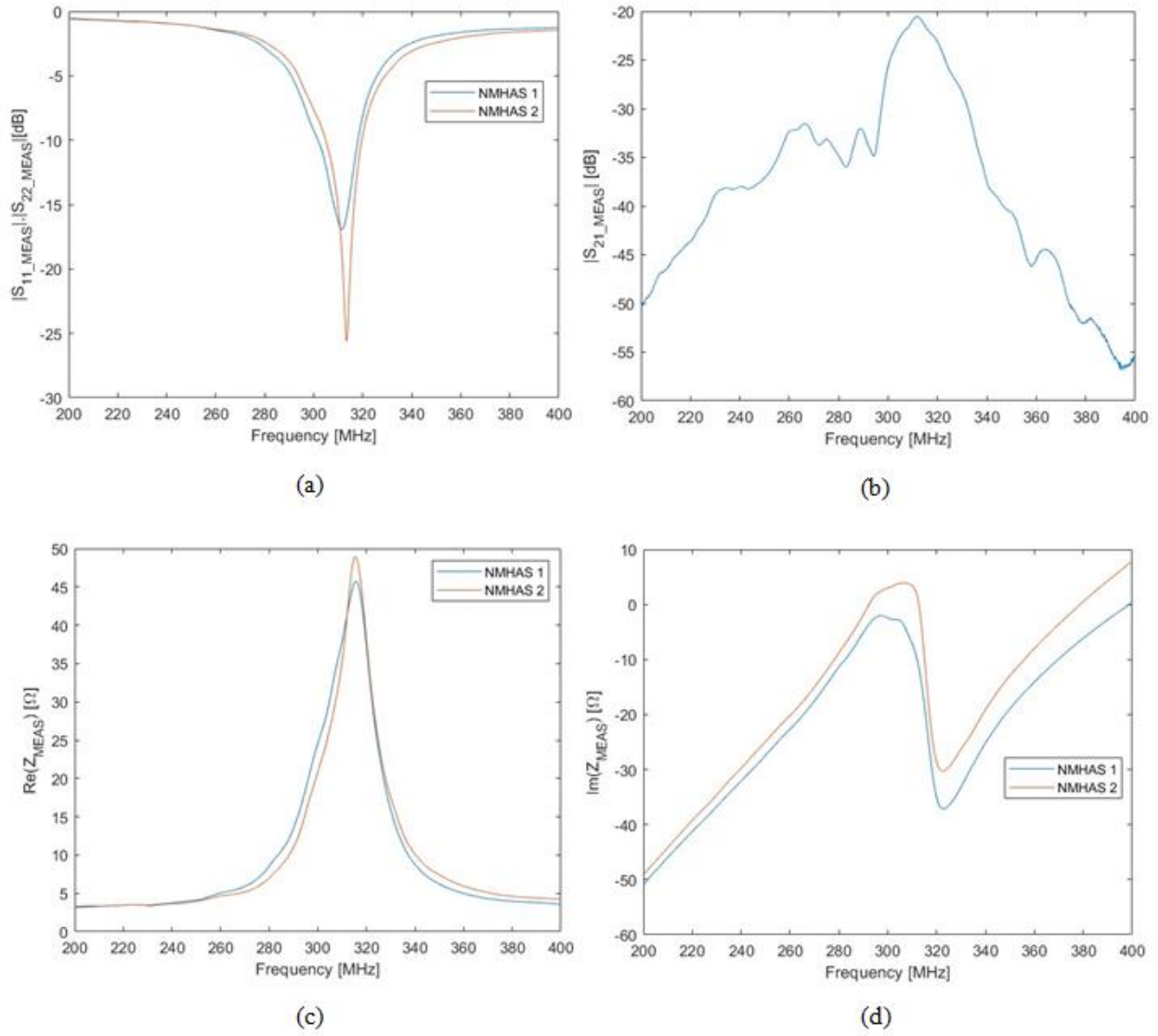


Figure 5.13: Frequency response of the antenna structures spaced 44 inches apart: a.) $|S_{11}|$ and $|S_{22}|$ [dB]; b.) $|S_{12}|$ [dB]; c.) $\text{Re}(Z_{MEAS})$ [Ω]; d.) $\text{Im}(Z_{MEAS})$ [Ω].

5.7.1.2 NMHAS spaced 22 inches apart

This section presents the measured transmission and impedance responses of the NMHAS spaced 22 inches apart. Figure 5.14 shows the NMHAS assembled on the testing fixture in the microwave laboratory and adjusted for a spacing of 22 inches apart by moving the right arm and leaving the left arm stationary.



Figure 5.14: NMHAS mounted on antenna mounting structure and spaced 22 inches apart.

Figure 5.15 shows the impedance and transmission responses of NMHAS mounted as shown in Figure 5.14. Figure 5.15b plots $|S_{21_MEAS}|$ for the two NMHAS mounted 22 inches apart. As can be seen from Figure 5.15b the minimum measured transmission loss for the two identical antennas is 19dB around 314 MHz.

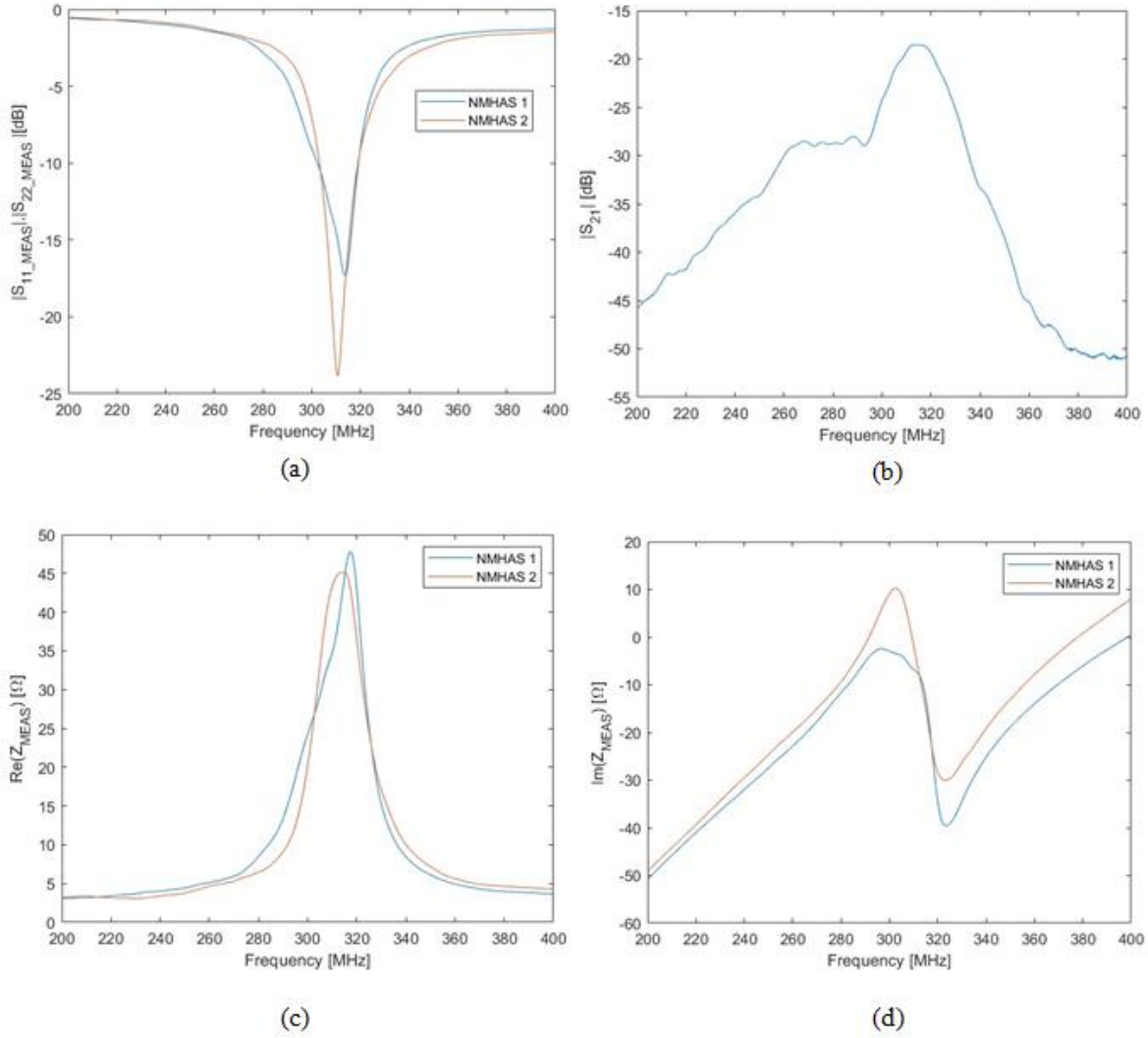


Figure 5.15: Frequency response of the antenna structures spaced 22 inches apart: a.) $|S_{11}|$ and $|S_{22}|$ [dB]; b.) $|S_{21}|$ [dB]; c.) $\text{Re}(Z_{\text{MEAS}})$ [Ω]; d.) $\text{Im}(Z_{\text{MEAS}})$ [Ω].

5.7.1.3 NMHAS spaced 10 inches apart

This section presents the measured transmission and impedance responses of the NMHAS spaced 10 inches apart. Figure 5.16 shows the NMHAS assembled on the testing fixture in the microwave laboratory and adjusted for a spacing of 10 inches by moving the right arm and leaving the left arm stationary.

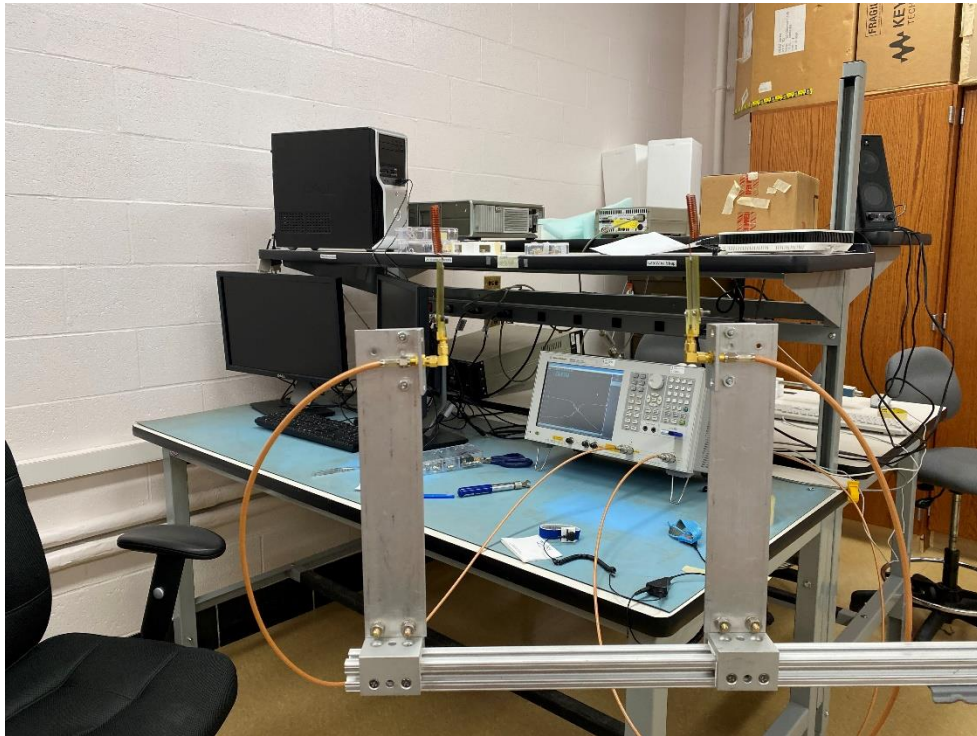


Figure 5.16: NMHAS mounted on antenna mounting structure and spaced 10 inches apart

Figure 5.17 shows the impedance and transmission responses of NMHAS mounted as shown in Figure 5.16. Figure 5.17b plots $|S_{21_MEAS}|$ for the two NMHAS mounted 10 inches apart. As can be seen from Figure 5.17b the measured transmission loss for the two identical antennas is around 18 dB around 310 MHz.

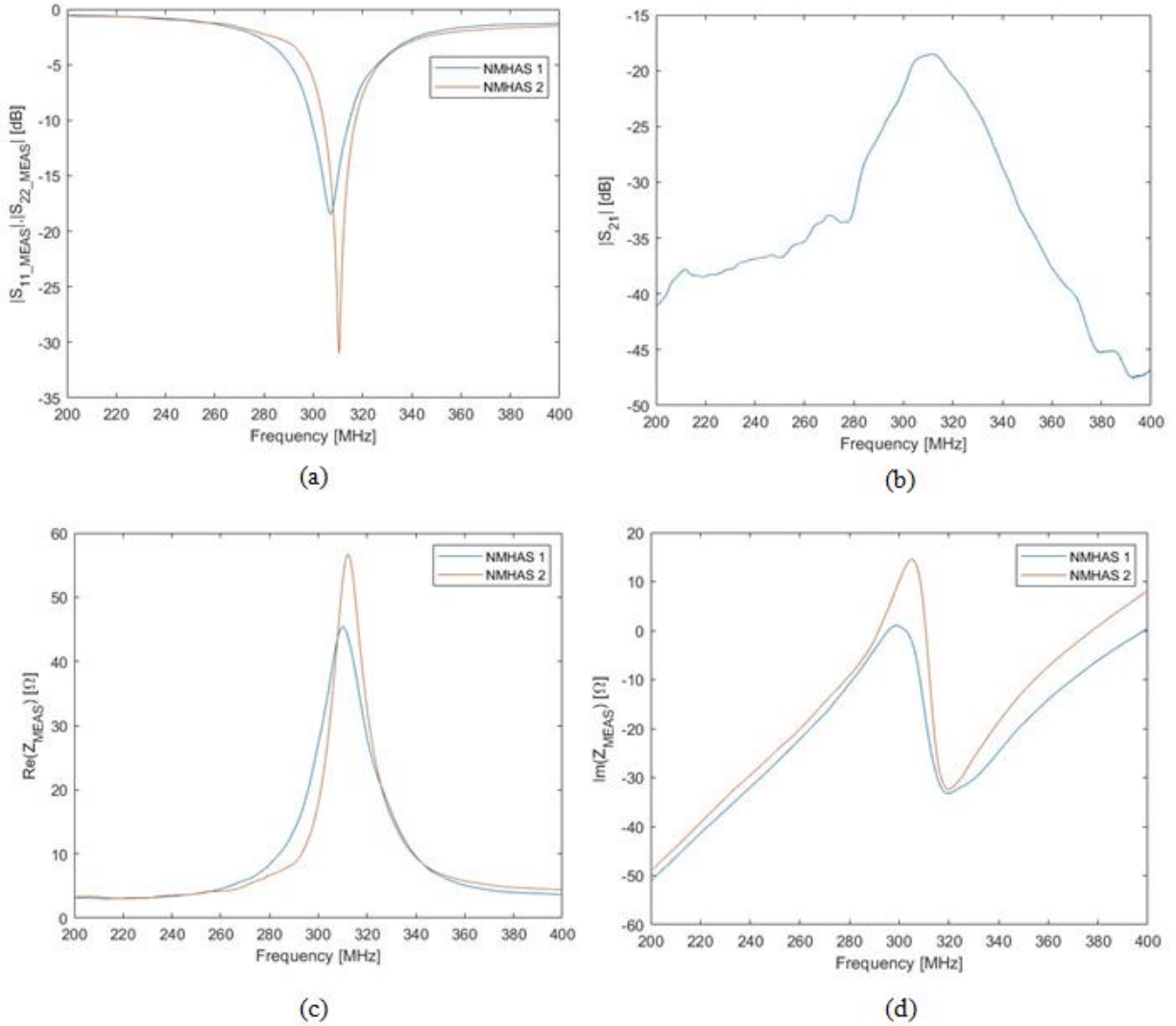


Figure 5.17: Frequency response of the NMHAS spaced 10 inches apart: a.) $|S_{11}|$ and $|S_{22}|$ [dB]; b.) $|S_{12}|$ [dB]; c.) $\text{Re}(Z_{\text{MEAS}})$ [Ω]; d.) $\text{Im}(Z_{\text{MEAS}})$ [Ω].

From Figure 5.13, Figure 5.15 and Figure 5.17 it can be observed that the impedance response of both the NMHAS varies as the distance between the NMHAS is varied. This shows that each of the NMHAS influences the impedance response of the other. Comparing the impedance response of both NMHAS reported above with Figure 4.7 shows that the real part of input impedance at Plane A changed from being in the interval between 80 Ω to 120 Ω , when each antenna was tested separately, to be almost matched to 50 Ω when tested in front of each other. The measured

transmission loss around 300 MHz was about 20 dB. The next section discusses the response of the NMHAS with the presence of an additional impedance matching circuit discussed in Section 4.5.

5.7.2 S-parameters Measurement with Additional Impedance Matching Circuit

This section presents the transmission and impedance response of two similar NMHAS with the presence of an impedance matching network discussed in Chapter 4, Section 4.5. The NMHAS were spaced facing each other at several distances.

5.7.2.1 NMHAS placed 44 inches apart

This section presents the measured transmission and impedance responses of the NMHAS spaced 44 inches apart. Figure 5.18 shows the two NMHAS with impedance matching networks mounted on the testing fixture in the microwave laboratory and spaced 44 inches apart.



Figure 5.18: The NMHAS spaced 44 inches apart with the matching circuit connected.

Figure 5.19 shows the impedance and transmission responses of NMHAS mounted as shown in Figure 5.18. Figure 5.19b plots $|S_{21_MEAS}|$ for the two NMHAS mounted 44 inches apart. As can be seen from Figure 5.19b the measured transmission loss for the two identical antennas is around 22 dB around 310 MHz.

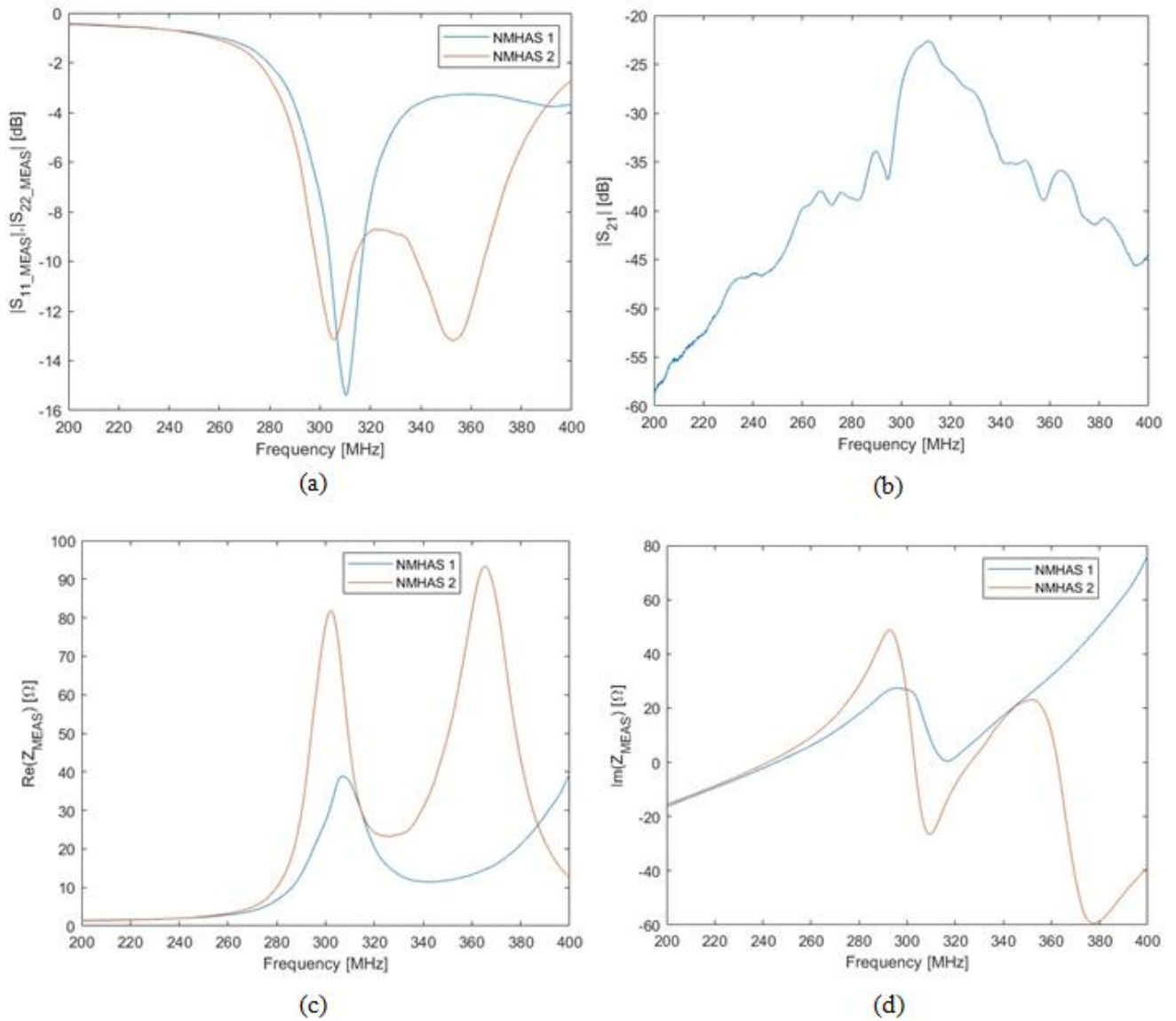


Figure 5.19: Frequency response of the NMHAS with matching network spaced 44 inches apart: a.) $|S_{11}|$ and $|S_{22}|$ [dB]; b.) $|S_{21}|$ [dB]; c.) $\text{Re}(Z_{MEAS})$ [Ω]; d.) $\text{Im}(Z_{MEAS})$ [Ω].

5.7.2.2 *NMHAS placed 22 inches apart*

This section presents the measured transmission and impedance responses of the NMHAS spaced 22 inches apart. Figure 5.20 shows the two NMHAS with impedance matching networks mounted on the testing fixture in the microwave laboratory and spaced 22 inches apart.

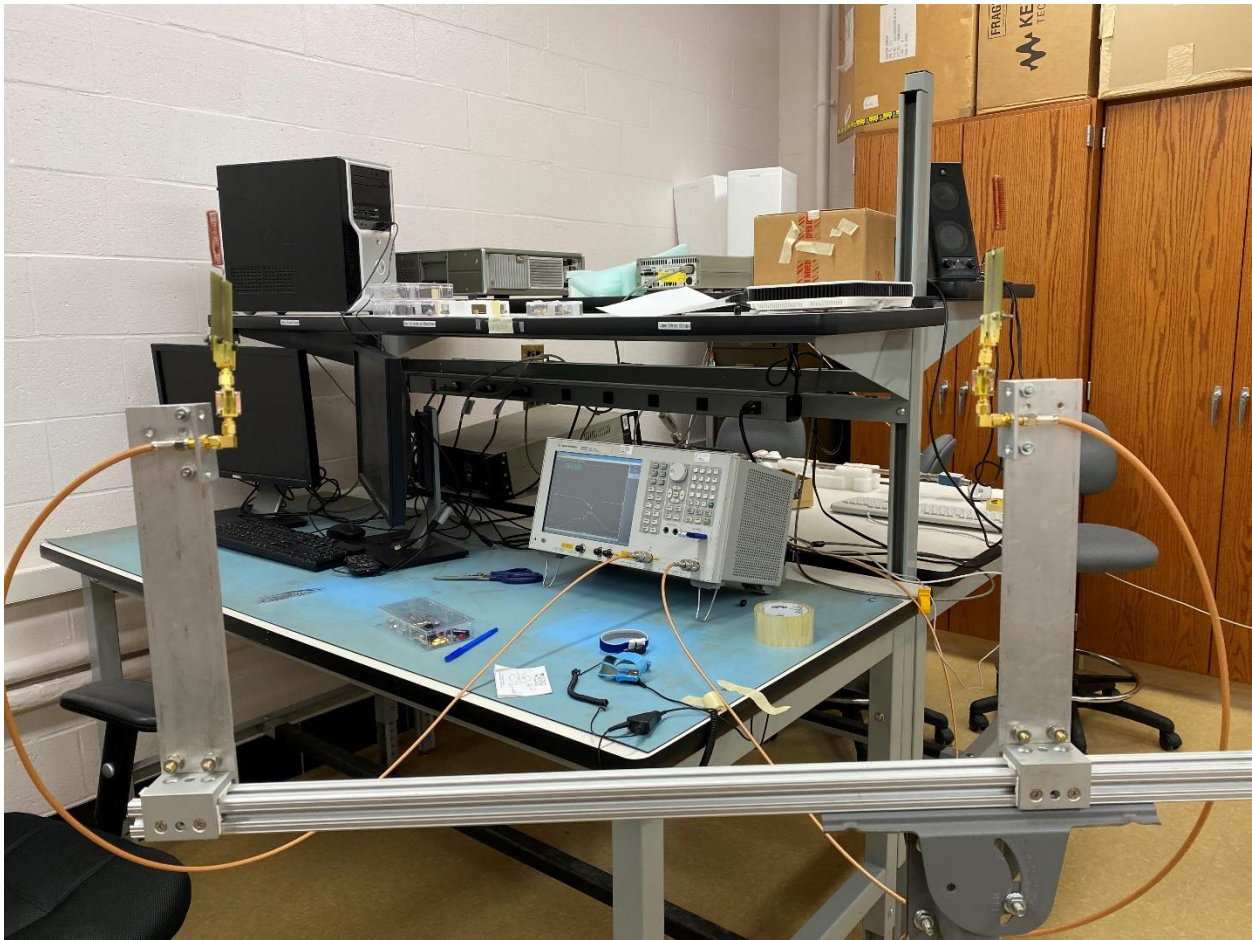


Figure 5.20: The NMHAS spaced 22 inches apart with the matching network connected.

Figure 5.21 shows the impedance and transmission responses of NMHAS mounted as shown in Figure 5.20. Figure 5.21b plots $|S_{21_MEAS}|$ for the two NMHAS mounted 22 inches apart. As can be seen from Figure 5.21b the measured transmission loss for the two identical antennas is around 20 dB around 310 MHz.

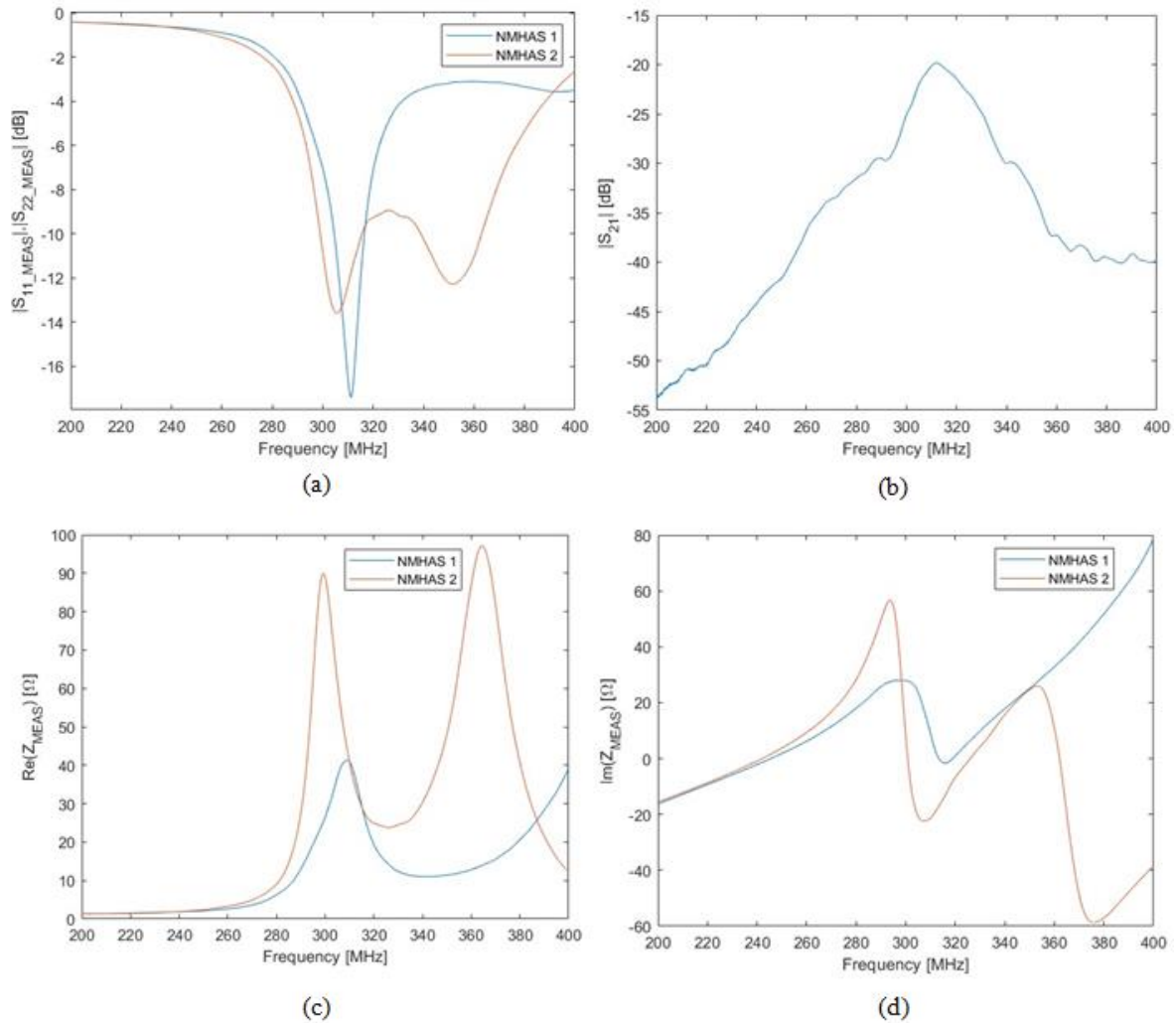


Figure 5.21: Frequency response of the NMHAS with matching network spaced 22 inches apart: a.) $|S_{11}|$ and $|S_{22}|$ [dB]; b.) $|S_{12}|$ [dB]; c.) $\text{Re}(Z_{MEAS})$ [Ω]; d.) $\text{Im}(Z_{MEAS})$ [Ω].

5.7.2.3 NMHAS placed 10 inches apart

This section presents the measured transmission and impedance responses of the NMHAS spaced 10 inches apart. Figure 5.22 shows the two NMHAS with impedance matching networks mounted on the testing fixture in the microwave laboratory and spaced 10 inches apart.



Figure 5.22: The NMHAS spaced 10 inches apart with the matching network connected.

Figure 5.23 shows the impedance and transmission responses of NMHAS mounted as shown in Figure 5.22. Figure 5.23b plots $|S_{21_MEAS}|$ for the two NMHAS mounted 22 inches apart. As can be seen from Figure 5.23b the measured transmission loss for the two identical antennas is around 20 dB around 309 MHz.

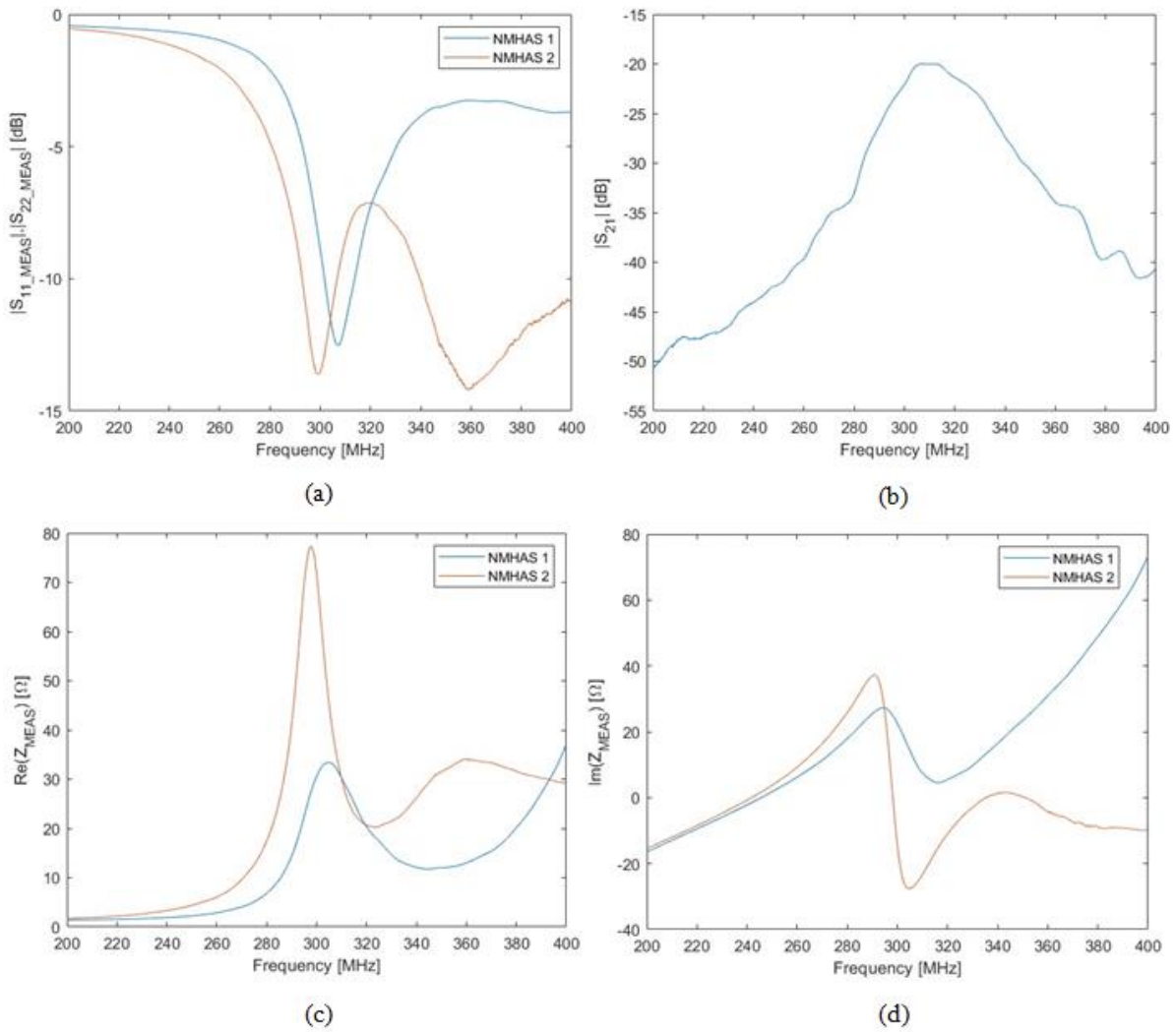


Figure 5.23: Frequency response of the NMHAS with matching network spaced 10 inches apart: a.) $|S_{11}|$ and $|S_{22}|$ [dB]; b.) $|S_{12}|$ [dB]; c.) $\text{Re}(Z_{MEAS})$ [Ω]; d.) $\text{Im}(Z_{MEAS})$ [Ω].

From Figure 5.19, Figure 5.21, and Figure 5.23, it can be observed that the impedance response of both the NMHAS with matching network varies as the distance between the NMHAS is varied as observed in the previous section. It can be observed that the impedance response and S_{21} response of both the NMHASs doesn't improve compared to the results reported in Section 5.7.1, since as discussed in that section the proximity between the two NMHASs changed the input impedances of each antennas to closer to 50Ω , and the length of the center conductor on fabricated FR-4 board and the placement of trimmer capacitor on the board affected the resulting implemented inductance and capacitive values, making them differ from those obtained from ADS shown in Figure 4.10.

The S-parameter response of the NMHAS with impedance matching network in Figure 5.19, Figure 5.21, and Figure 5.23 also report extra peaks in the impedance response which represent the presence of another resonance. This extra resonance in the structure seems to be related to the additional impedance matching circuit, as the additional resonant peaks are not aligned around the same frequency for the two antennas.

5.8 Conclusion

This chapter discussed the S_{11} and impedance response of NMHAS measured in two different laboratory environments and the results were compared. The variation in impedance is most likely due to different metallic structures present in and which influenced the NMHAS impedance. The NMHAS simulations presented in Chapter 3 were compared to the measured response in both laboratory environments and was observed that the measured and simulated resonant frequency were in good agreement. The effect of orientation of helix with respect to the microstrip line on the response of NMHAS was discussed. Finally, the transmission loss of two similar NMHASs placed at different distances apart from each other was measured with and without the presence of an additional matching network. It was found that at the measured distances between 10 inch and

44 inch the two NMHAS interact, thus affecting each other impedance when compared to each NMHAS operating alone. It was observed that when two NMHASs were placed in relatively close proximity to each other (10" to 44") the presence of an additional matching networks caused the appearance of an additional resonant frequency.

CHAPTER 6. CONCLUSIONS

The work in this thesis revolved around the study, design, and implementation of a NMHAS. Simulation of NMHAS was done in ANSYS-HFSS and WIPL-D to determine the S_{11} and therefore the input impedance as a function of frequency. The NMHAS was measured both in lab environment and in an anechoic chamber. The sensitivity of the NMHAS to different physical dimension variations has been discussed.

6.1 Summary of work and Conclusion

Chapter 1 reviewed the motivation for this work, antenna applications and technology and the fundamental antenna nomenclature.

Chapter 2 discussed the existing theoretical background on conventional Normal Mode Helical Antenna based on Krauss [58]. It also referred to the application notes the NMHAS implemented in this work is based on. Chapter 2 also discusses that connecting the helical structure directly to a coaxial cable cause current flow on the outer shield of the coaxial cable which becomes then part of the radiating structure. This result laid groundwork for implementing the helical structure with different type and sizes of ground planes, namely by connecting the helix to microstrip lines of different dimensions.

Chapter 3 presented the simulation of the NMHAS utilizing two commercially available platforms: HFSS and WIPL-D Pro. The NMHAS was simulated with four different microstrip lengths: 0.5 inch, 1 inch, 2 inch, 3 inch. It was verified that increase in size of ground plane the resonant frequency diminishes from 366 MHz to 313 MHz. At resonance, the input impedance simulated at the input of the microstrip line was transferred to the helix connection point and it was found that the reactance of transferred impedance goes from inductive to capacitive. The sensitivity of the NMHAS to its physical design dimensions was also discussed with the aid of WIPL-D

simulations and it was observed that the response of the NMHAS is mostly sensitive to diameter of helix.

Chapter 4 discussed the NMHAS fabrication and experimental setup implementation. A balun was introduced between the SMA connector and NMHAS in an attempt to mitigate the participation of the coaxial cable shield in the radiation of the NMHAS. The balun parasitics network was modeled and simulated with the aid of ADS. The measured impedance at the input of the NMHAS plus balun structure was transferred to the input of the microstrip using the balun modeled circuit. The NMHAS impedance response variation due to the fabrication procedure was discussed based on the response of four similarly fabricated helices connected to the same two-inch microstrip line. Variations of 50% in input impedance and 3% in the resonant frequency were observed. Variations in the diameter and in the spacing when fabricating the helix by winding using the screw. The impedance responses of a NMHAS connected to two similar balun jigs were measured and it was observed that both the fabricated jigs performed very consistently. An LC impedance matching network was designed and optimized using ADS to match the measured NMHAS impedance at the balun input to 50Ω .

Chapter 5 was dedicated to the impedance and transmission responses of NMHAS. The NMHAS impedance was measured and validated in a laboratory environment and in the anechoic chamber. Variations in the measured impedance were credited to the laboratory environment, where metallic structures present in the laboratory affect the NMHAS impedance response. The NMHAS simulations presented in Chapter 3 were compared to the measured responses in both laboratory environments and it was observed that the measured and simulated resonant frequency agree within 4.8%. Comparison between measured and simulated impedance responses revealed that further study and modelling work is necessary for better predicting the NMHAS impedance. The

effect of the helix orientation with respect to the microstrip line plane on the response of NMHAS was also measured and found to have an impact on antenna impedance response. Finally, the transmission loss of two similar NMHASs placed at different distances apart from each other was measured with and without the presence of an additional matching network. It was found that at the measured distances between 10 inch and 44 inch the two NMHASs interact, thus affecting each other impedance when compared to each NMHAS operating alone. Therefore, as an overall conclusion, this work identified the feasibility of implementing compact (with respect to the wavelength) normal mode helical antenna structures using air as dielectric, which is appropriate for high-temperature harsh-environment applications. The simulated and measured frequency and impedance responses of the structures implemented, which used a microstrip line ground plane as part of the radiating structure, showed that this structure is suitable to provide communication between interrogating antennas and sensors in wireless sensor links.

6.2 Major findings and contributions from this work

Key contributions of this thesis are summarized below:

- The direct connection of a helical structure to a coaxial cable causes current flow on the outer shield of the coaxial cable which then becomes part of the radiating structure.
- The connection of a helix to a microstrip line allowed the use of the microstrip ground plane as part of the radiating structure, labelled in this work Normal Mode Helical Antenna Structure.
- The usage of a balun to connect the coaxial cable to the NMHAS, treated as a balanced structure, reduced the participation of the outer coaxial shield in the antenna radiation.
- Simulations of the proposed NMHAS utilizing two software packages showed good agreement between measured and simulated resonant frequencies.

- The helix orientation with respect to the microstrip line plane was found to have an impact in the antenna impedance response.
- Two NMHAS were observed to affect each other's impedance response when connected to the VNA as opposed to each operating alone.
- The frequency response of the NMHAS is more sensitive to the diameter of the helix when compared to the spacing between the turns and the width of the wire.

6.3 Suggested future work

Based on the work presented in this thesis, future investigation topics for the NMHAS includes:

- Integrate NMHAS with a SAW sensor and adjust the structural parameters of the NMHAS dimensions and packaging for optimal performance.
- Implement the NMHAS at high temperatures up to 1000°C.
- Explore additional implementation of baluns for high temperature operation.
- Improve the modelling of NMHAS on HFSS and WIPL-D to better describe the NMHAS impedance response.
- Utilizing COMSOL to investigate the NMHAS impedance response, including the effect of temperature variations.
- Investigate the development of analytical models for the NMHAS based on alternative implementations of the ground plane.

REFERENCES

1. M. Pereira da Cunha. "Wireless sensing in hostile environments". In: IEEE Intl. Ultrasonics Symposium, IUS (2013), pp. 1337–1346. issn: 19485719.
2. P. Davulis. "Characterization of the Elastic , Piezoelectric , and Dielectric Properties of Langatate At High Temperatures Up To 900 C". Ph. D. University of Maine, 2013.
3. M. Werner and W. Fahrner. "Review on materials, microsensors, systems, and devices for high-temperature and harsh-environment applications". In: IEEE Transactions on Industrial Electronics 48.2 (2001), pp. 249–257. issn: 02780046.
4. X. Jiang, K. Kim, S. Zhang, et al. "High-temperature piezoelectric sensing". In: Sensors (Switzerland) 14.1 (2013), pp. 144–169. issn: 14248220.
5. Haitao Cheng, Gang Shao, Siamak Ebadi, Xinhua Ren, Kyle Harris, Jian Liu, Chengying Xu, Linan An, Xun Gong, "Evanescent-mode-resonator-based and antenna-integrated wireless passive pressure sensors for harsh-environment applications", in Sensors and Actuators A: Physical, Volume 220, 2014, Pp 22-33. ISSN: 0924-4247
6. A. Ghazanfari, W. Li, M. Leu, et al. "Advanced ceramic components with embedded sapphire optical fiber sensors for high temperature applications". In: Materials and Design 112 (2016), pp. 197–206. issn: 18734197.
7. S. F. Jilani, D. Leff, A. Maskay, R. J. Lad and M. Pereira da Cunha, "Static Strain Modelling, Calibration, and Measurements for High-Temperature Wireless SAW Resonator Operation," In: 2020 IEEE International Ultrasonics Symposium (IUS), 2020, pp. 1-4. issn: 19485727.
8. R. Loloee, B. Chorpening, S. Beer, et al. "Hydrogen monitoring for power plant applications using SiC sensors". In: Sensors and Actuators, B: Chemical 129.1 (2008), pp. 200–210. issn: 09254005.
9. Tchafa, F. E. M., "Wireless antenna sensors for boiler condition monitoring", Ph. D dissertation, Dept. Elec. Eng., Univ. of Texas, Arlington, TX, 2018.
10. Y. Liu, J. Parisi, X. Sun, et al. "Solid-state gas sensors for high temperature applications-a review". In: Journal of Materials Chemistry A 2.26 (2014), pp. 9919–9943. issn: 20507496.
11. A. Trinchi, S. Kandasamy, and W. Wlodarski. "High temperature field effect hydrogen and hydrocarbon gas sensors based on SiC MOS devices". In: Sensors and Actuators B : Chemical 133 (2008), pp. 705–716.

12. R. Turner, P. Fuierer, R. Newnham, et al. "Materials for high temperature acoustic and vibration sensors: A review". In: *Applied Acoustics* 41.4 (1994), pp. 299–324. issn: 0003682X. 116
13. V. Latini, V. Striano, G. Coppola, et al. "Fiber optic sensors system for high temperature monitoring of aerospace structures". In: *Photonic Materials, Devices, and Applications II*. Ed. by Ali Serpengüzel, Gonçal Badenes, and Giancarlo C Righini. Vol. 6593. International Society for Optics and Photonics. SPIE, 2007, pp. 223–231.
14. R. Fachberger and A. Erlacher. "Monitoring of the temperature inside a lining of a metallurgical vessel using a SAW temperature sensor". In: *Procedia Chemistry* 1.1 (2009), pp. 1239–1242. issn: 18766196.
15. J. Chen, J. Zhang, M. Wang, et al. "High-temperature hydrogen sensor based on platinum nanoparticle-decorated SiC nanowire device". In: *Sensors and Actuators, B: Chemical* 201 (2014), pp. 402–406. issn: 09254005.
16. R. Lewis. "Sax's dangerous properties of industrial materials". In: *Choice Reviews Online* 30.05 (1993), pp. 30–2435–30–2435. issn: 0009-4978.
17. M. Apostol, T. Vuoristo, and V. Kuokkala. "High temperature high strain rate testing with a compressive SHPB". In: *Journal de Physique Archives* 110 (2003), pp. 459–464. issn: 11554339.
18. G. Hunter, J. Wrbanek, R. Okojie, et al. "Development and application of high temperature sensors and electronics for propulsion applications" In: *Sensors for Propulsion Measurement Applications*. Ed. by Valentin Korman. Vol. 6222. Intl. Society for Optics and Photonics. SPIE, 2006, pp. 76–87.
19. French, P., Krijnen, G. & Roozeboom, F. "Precision in harsh environments." *Microsyst Nanoeng* 2, 16048 (2016)
20. C. Mai, S. Pedersen, L. Hansen, K. L. Jepsen and Zhenyu Yang, "Subsea infrastructure inspection: A review study," 2016 IEEE International Conference on Underwater System Technology: Theory and Applications (USYS), Penang, Malaysia, 2016, pp. 71-76, doi: 10.1109/USYS.2016.7893928.
21. Meador, Mary Ann B., Miranda, Felix A., "Design and development of Aerogel-Based Antennas for Aerospace Applications: A Final report to the NARI Seedling", Aug. 2014, Document ID: 20140017756.
22. C.A. Balanis, "Modern Antenna Handbook", 3rd Edition, Hoboken, NJ : John & Wiley Sons, Inc., 2008.

23. R. Raulefs, M. Wirsing and W. Wang, "Increasing Long Range Coverage by Multiple Antennas for Maritime Broadband Communications," OCEANS 2018 MTS/IEEE Charleston, Charleston, SC, USA, 2018, pp. 1-6, doi: 10.1109/OCEANS.2018.8604914.
24. Intikhab Hussain, Frederick Cawood, Rex van Olst, "Effect of tunnel geometry and antenna parameters on through-the-air communication systems in underground mines: Survey and open research areas", Physical Communication, Volume 23, 2017, Pages 84-94, ISSN 1874-4907.
25. Budampati, Ramakrishna, and Soumitri Kolavennu, eds. "Industrial wireless sensor networks: monitoring, control and automation.", Elsevier, 2015.
26. Barrenetxea, G., Ingelrest, F., Schaefer, G., & Vetterli, M., "Wireless sensor networks for environmental monitoring: The sensorscope experience." In 2008 IEEE International Zurich Seminar on Communications (pp. 98-101), IEEE.
27. Karnaushenko, Dmitriy D., Daniil Karnaushenko, Denys Makarov, and Oliver G. Schmidt. "Compact helical antenna for smart implant applications." NPG Asia Materials 7, no. 6 (2015): e188-e188.
28. H. Cheng, X. Ren, S. Ebadi, Y. Chen, L. An and X. Gong, "Wireless Passive Temperature Sensors Using Integrated Cylindrical Resonator/Antenna for Harsh-Environment Applications," in IEEE Sensors Journal, vol. 15, no. 3, pp. 1453-1462, March 2015, doi: 10.1109/JSEN.2014.2363426.
29. Daniel, Justin, Spencer Nguyen, Md Atiqur Rahman Chowdhury, Shaofan Xu, and Chengying Xu. "Temperature and Pressure Wireless Ceramic Sensor (Distance= 0.5 Meter) for Extreme Environment Applications." Sensors 21, no. 19 (2021): 6648.
30. Pirich, Ronald, Kristie D'Ambrosio. "Fiber optics for harsh environments." 2011 IEEE Long Island Systems, Applications and Technology Conference. IEEE, 2011.
31. M. Pereira da Cunha, Lad, R. J., Moonlight, T., Moulzolf, S., Canabal, A., Behanan, R., ... & McCann, D. F. (2011). "Recent advances in harsh environment acoustic wave sensors for contemporary applications" SENSORS, 2011 IEEE, 614-617.
32. M. Pereira da Cunha, R. J. Lad, P. Davulis, A. Canabal, T. Moonlight, S. Moulzolf, D. J. Frankel et al. "Wireless acoustic wave sensors and systems for harsh environment applications." In 2011 IEEE Topical Conference on Wireless Sensors and Sensor Networks, pp. 41-44. IEEE, 2011.
33. M. Pereira da Cunha, R. J. Lad, T. B. Pollard, D. McCann, E. McCarthy, P. Prata, and R. Kelley. "Wireless harsh environment SAW array system for power plant application." In 2014 IEEE International Ultrasonics Symposium, pp. 381-384. IEEE, 2014.

34. Sidén, Johan, and Hans-Erik Nilsson. "An electrically small elliptic PIFA for RFID in harsh metallic environments." 2013 IEEE International Conference on Microwaves, Communications, Antennas and Electronic Systems (COMCAS 2013). IEEE, 2013.
35. M. Pereira da Cunha, "High-Temperature Harsh-Environment SAW Sensor Technology", Proceedings of the 2023 IUS Intern. Ultrason. Symposium, Montreal, Canada, IEEE, ISBN: 979-8-3503-4645-9 2023.
36. M. Hirvonen, P. Pursula, K. Jaakkola and K. Laukkanen, "Planar inverted-F antenna for radio frequency identification," *Electron. Lett.*, Vol. 40, No. 14, pp. 848-850, 2004
37. H. Kwon, B. Lee, "Compact slotted planar inverted-F RFID tag mountable on metallic objects," *Electron. Lett.*, Vol. 41, No. 24, pp. 1308-1310, 2005
38. Watson, J. and G. Castro, "A review of high-temperature electronics technology and applications," *Journal of Materials Science: Materials in Electronics*, Vol. 26, No. 12, 9226-9235, 2015.
39. K. T. Keddy, "High-Temperature Ceramic Materials for Antenna Applications," *Microwave Journal*, vol. 50, no. 10, pp. 126-138, October 2007.
40. M. Y. A. Rahman and A. F. M. Yusof, "A Review on High-Temperature Materials for Antenna Applications," *International Journal of Engineering Research and Applications*, vol. 3, no. 6, pp. 935-947, November-December 2013.
41. H. Kim, H. Choi, and Y. Kim, "Carbon/Carbon Composites for High-Temperature Antenna Applications," *Materials Science Forum*, vol. 544-545, pp. 867-870, 2007.
42. H. Li, G. Xue, and X. Li, "High-Temperature Polyimide Materials for Antenna Applications: A Review," *Journal of Materials Science: Materials in Electronics*, vol. 27, no. 4, pp. 3384-3397, April 2016.
43. Chu, Q. X., Werner, D. H., & Young, B. R. "Antenna performance at high temperatures: effect of dielectric materials.", 2002 *IEEE Transactions on Antennas and Propagation*, 50(8), 1109-1115.
44. Talukdar, A., Thakur, N. K., & Bhattacharyya, A. K. "Design and performance analysis of high-temperature patch antennas.", 2013 *IEEE Transactions on Antennas and Propagation*, 61(8), 4339-4343.
45. G. S. Smith, "Dielectric properties of air at microwave frequencies," *Proceedings of the IEEE*, vol. 53, no. 11, pp. 1632-1633, November 1965.

46. J. R. Mosig and M. Okoniewski, "Air dielectric microstrip lines and slotlines for high temperature applications," *IEEE Transactions on Microwave Theory and Techniques*, vol. 35, no. 9, pp. 833-837, September 1987.
47. M. A. Morgan and A. D. Yaghjian, "The effects of temperature on air-filled cavity resonators," *IEEE Transactions on Microwave Theory and Techniques*, vol. 35, no. 1, pp. 48-54, January 1987.
48. J. D. Dyson, "A Simple Air-Cooled Broadband Antenna for High Temperature Applications," *IEEE Transactions on Antennas and Propagation*, vol. 38, no. 4, pp. 604-606, April 1990.
49. K. J. Vinoy, C. K. Aanandan, and K. T. Mathew, "Design and Development of Air-Dielectric Patch Antenna for High Temperature Applications," *Microwave and Optical Technology Letters*, vol. 48, no. 7, pp. 1379-1383, July 2006.
50. A. M. A. Abou-Elnour, A. A. Kishk, and A. B. Yakovlev, "Design of a Low-Profile Air-Filled Dielectric Resonator Antenna for High Temperature Applications," *IEEE Transactions on Antennas and Propagation*, vol. 58, no. 8, pp. 2772-2776, August 2010.
51. Pozar, D. M., "Introduction to Microwave systems", in "Microwave engineering", 4th Ed., 2011 John Wiley & Sons.
52. Aiken, Nicholas, "VHF Near Field Antenna Design for Wireless Sensing Applications in Harsh Environments", Honors Thesis, Dept. Elect. and Comp. Eng., Univ of Maine, Orono, ME, 2019.
53. J.D.Krauss, "Basic Antenna Concepts" and "The Helical Antenna" in "Modern antenna applications", 2nd Ed., Tata McGraw Hill Publishing Company Limited, New Delhi, India.
54. S. L. S. Kilambi and M. Pereira da Cunha, "Design and Measurements of a Small Normal Mode Helical Antenna with Integrated Microstrip Structure," 2022 Antenna Measurement Techniques Association Symposium (AMTA), Denver, CO, USA, 2022, pp. 1-6, doi: 10.23919/AMTA55213.2022.9955019.
55. A. Takacs, N. J. G. Fonseca and H. Aubert, "Height Reduction of the Axial-Mode Open-Ended Quadrifilar Helical Antenna," in *IEEE Antennas and Wireless Propagation Letters*, vol. 9, pp. 942-945, 2010. Issn: 15485757.
56. Xueli Liu, Shun Yao, S. V. Georgakopoulos, B. S. Cook and M. M. Tentzeris, "Reconfigurable helical antenna based on an origami structure for wireless communication system," in 2014 IEEE MTT-S International Microwave Symposium (IMS2014), 2014, pp. 1-4. Issn: 0149645X.

57. N. Q. Dinh, N. Michishita, Y. Yamada and K. Nakatani, "Design method of a tap feed for a very small normal-mode helical antenna," 2009 Asia Pacific Microwave Conference, 2009, pp. 2416-2419. Issn: 21654743.
58. Dinh, N. Q., Michishita, N., Yamada, Y., & Nakatani, K. "Development of a Very Small Normal Mode Helical Antenna for the Tire Pressure Sensor of TPMS", in IEICE Proceedings Series, 2008, 35(4C32-1).
59. Y. Yamada, W. G. Hong, W. H. Jung and N. Michishita, "High gain design of a very small normal mode helical antenna for RFID tags," in TENCON 2007 - 2007 IEEE Region 10 Conference, 2007, pp. 1-4. Issn: 21593450
60. K. Noguchi, M. Mizusawa, M. Nakailama, T. Yamaguchi, Y. Okumura and S. Betsudan, "Increasing the bandwidth of a normal mode helical antenna consisting of two strips," in IEEE Antennas and Propagation Society International Symposium. 1998 Digest. Antennas: Gateways to the Global Network. Held in conjunction with: USNC/URSI National Radio Science Meeting (Cat. No.98CH36, 1998, pp. 782-785 vol.2. issn: 0-7803-4478-2.
61. H. Nakano, N. Ikeda, Yu-Yuan Wu, R. Suzuki, H. Mimaki and J. Yamauchi, "Realization of dual-frequency and wide-band VSWR performances using normal-model helical and inverted-F antennas," in IEEE Transactions on Antennas and Propagation, vol. 46, no. 6, pp. 788-793, June 1998. Issn: 1558-2221.
62. Dinh, N. Q., Michishita, N., Yamada, Y., & Nakatani, K. "Circuit Theory Analysis of the input impedance in a Tap Feed Small Normal-Mode Helical Antenna" in IEICE Proceedings Series, 51(2B4-5), 2009.
63. N. T. Tuan et al., "Deterministic Equation of Self-Resonant Structures for Normal-Mode Helical Antennas Implanted in a Human Body," in IEEE Antennas and Wireless Propagation Letters, vol. 17, no. 8, pp. 1377-1381, Aug. 2018. Issn: 1548-5757.
64. Woong Hyun Jung, N. Michishita and Y. Yamada, "Novel tapped feed structures for extremely small normal mode helical antennas," 2006 IEEE Antennas and Propagation Society International Symposium, 2006, pp. 1047-1050. Issn: 1947-1491.
65. N. Q. Dinh, T. Teranishi, N. Michishita, Y. Yamada and K. Nakatani, "Simple design equations of tap feeds for a very small normal-mode helical antenna," 2010 IEEE Antennas and Propagation Society International Symposium, 2010, pp. 1-4. Issn: 1947-1491.
66. D. T. Dung, N. Q. Dinh, N. T. Tuan, Y. Yamada and N. Michishita, "Simulation methods of a normal-mode helical antenna in a human body condition," 2016 International Conference on Advanced Technologies for Communications (ATC), 2016, pp. 380-383. Issn: 2162-1039.

67. Hong, W. ., Michishita, N. ., & Yamada, Y. . (2022). "Low-profile Normal-Mode Helical Antenna for Use in Proximity to Metal" in The Applied Computational Electromagnetics Society Journal (ACES), 25(3), 190–198.
68. K. Ochiyama, N. Michishita and Y. Yamada, "Effects of dielectric or magnetic materials to electrical characteristics of very small normal-mode helical antennas," Proceedings of the 2012 IEEE International Symposium on Antennas and Propagation, 2012, pp. 1-2. Issn: 1947-1491.
69. N. Q. Dinh, "A design of very small normal mode helical antenna for wireless communication systems," in The 2012 International Conference on Advanced Technologies for Communications, 2012, pp. 191-194. Issn: 2162-1039.
70. N. T. Tuan, Y. Yamada, N. Q. Dinh and N. Michishita, "Self-resonant structures of normal-mode helical antennas embedded in dielectric and magnetic materials," in 2015 International Conference on Advanced Technologies for Communications (ATC), 2015, pp. 627-632. Issn: 2162-1020.
71. Dung, D. T., Nguyen, Q. D., Trinh, D. Q., & Yamada, Y. "Investigating equations used to design a very small normal-mode helical antenna in free space" in International Journal of Antennas and Propagation, 2018.
72. D. -R. Shin, G. Lee and W. S. Park, "Simplified Vector Potential and Circuit Equivalent Model for a Normal-Mode Helical Antenna," in IEEE Antennas and Wireless Propagation Letters, vol. 12, pp. 1037-1040, 2013. Issn: 1548-5757.
73. Noguchi, K., Mizusawa, M., Yamaguchi, T., & Okumura, Y. " Impedance characteristics of two-wire helical antenna in normal mode" in Electronics and Communications in Japan (Part I: Communications), 81(12), 37-44, 1998.
74. A. Pohl and F. Seifert, "Wirelessly interrogable surface acoustic wave sensors for vehicular applications," in IEEE Transactions on Instrumentation and Measurement, vol. 46, no. 4, pp. 1031-1038, Aug. 1997. Issn: 1557-9662.
75. Sang Il Kwak, Kihun Chang and Young Joong Yoon, "The helical antenna for the capsule endoscope," 2005 IEEE Antennas and Propagation Society International Symposium, 2005, pp. 804-807 vol. 2B. issn: 1947-1491.
76. Kent Smith, "Antennas for low power applications", RF Monolithics.
77. "Surface mount Transformer TC1-1-13M+ RF", Mini-circuits. [Online] Available: <https://www.minicircuits.com/pdfs/TC1-1-13M+.pdf>
78. Smith V4.1, Fritz Dellsperger, 2018, Computer Smith-Chart Tool and S-Parameter Plot software available at <http://www.fritz.dellsperger.net/smith.html>.

APPENDICES

APPENDIX A. SIMULATIONS OF NMHAS WITH HELIX 2

This appendix discusses the simulation of Helix 2 mentioned in Section 4.4.1, connected to microstrip lines of different lengths. The NMHAS with Helix 2 is simulated on HFSS and WIPL-D. Section A.1 gives the dimensions of Helix 2 used for simulation. The simulation response of the NMHAS with Helix 2 on these platforms is discussed in Section A.2 and Section A.3.

A.1 Dimensions of Helix 2

This section gives the dimensions of Helix 2 connected to different microstrip lines. The Helix 2 is fabricated using the same screw used to fabricate Helix 1 (Table 2.1) which is chosen for all the measurements and simulations so far in this work. Table A.1 gives dimensions of the Helix 2.

d [mm]	h [mm]	D _h [mm]	S [mm]	N
0.9	8.	6.3	0.47	27

Table A.1: Dimensions of Helix 2

A.2 Simulation of NMHAS with Helix 2 on HFSS

As discussed in Section 2.5, helical structure is connected to microstrip lines of varying lengths. Specifically, the helix structure is sequentially connected to four different microstrip lines measuring 0.5", 1", 2", and 3". In each of the subsections, simulation results are presented for NMHAS with Helix 2 employing microstrips with the different lengths mentioned above. For simulation purposes in HFSS, a rectangular radiation box with dimensions of 25cm × 25cm × 30cm is utilized.

A.2.1 Half inch microstrip line:

Helix 2 is connected at one end of a half-inch microstrip line, and the 50Ω generator input is connected at the other end of the microstrip line. The ground plane of the microstrip line serves as the ground plane for the helix structure, thus composing the NMHAS. Figure A.1 shows the computed frequency response of Helix 2 connected to the half-inch microstrip line. Specifically, Figure A.1a displays the magnitude of the reflection coefficient ($|S_{11_Simulated}|$), while Figures A.1b and A.1c show the real and imaginary parts of the input impedance, respectively.

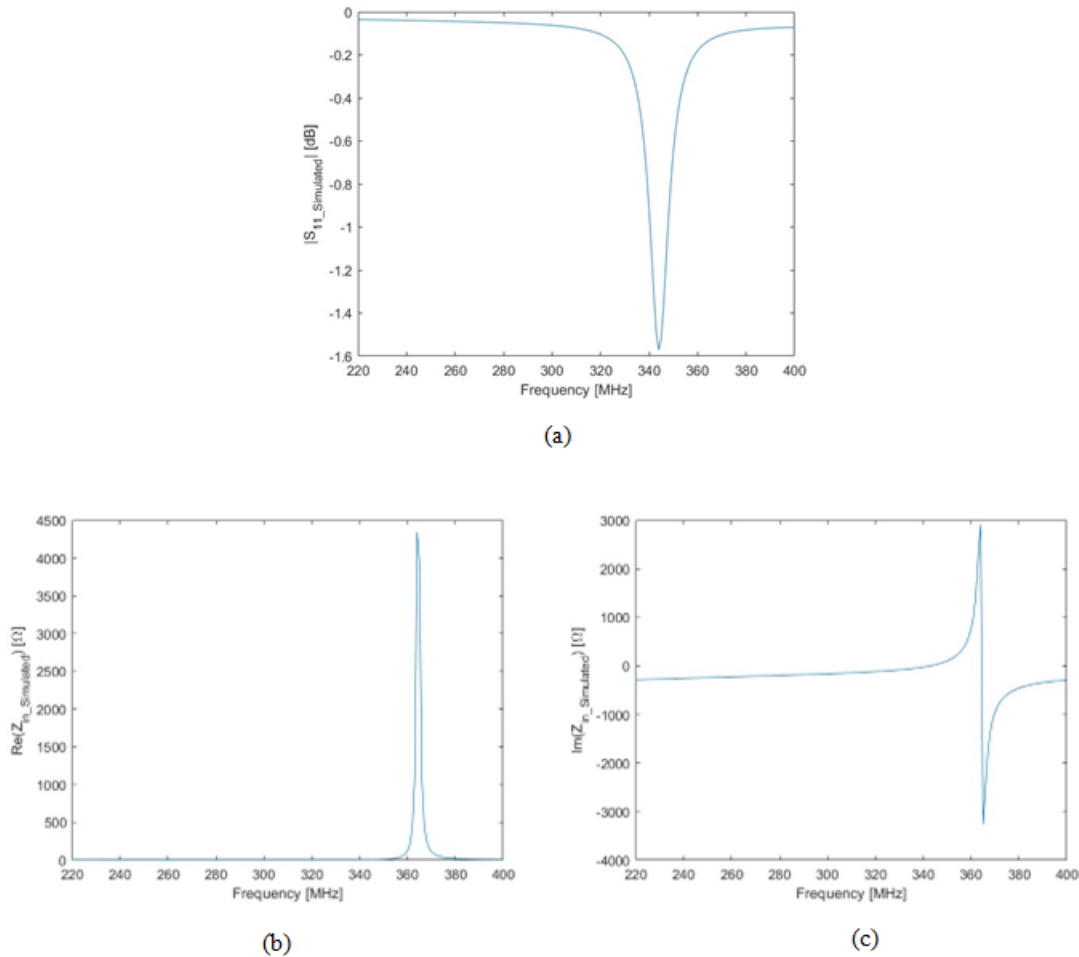


Figure A.1: Frequency response of Helix 2 connected at the end of half-inch microstrip line simulated on HFSS: a) $|S_{11_Simulated}|$ [dB]; b) $\text{Re}(Z_{in_Simulated})$ [Ω]; c) $\text{Im}(Z_{in_Simulated})$ [Ω].

A.2.2 One-inch microstrip line

Helix 2 is connected at one end of a one-inch microstrip line, and the 50Ω generator input is connected at the other end of the microstrip line. Figure A.2 shows the computed frequency response of Helix 2 connected to the one-inch microstrip line. Specifically, Figure A.2a displays the magnitude of the reflection coefficient ($|S_{11_Simulated}|$), while Figures A.2b and A.2c show the real and imaginary parts of the input impedance, respectively.

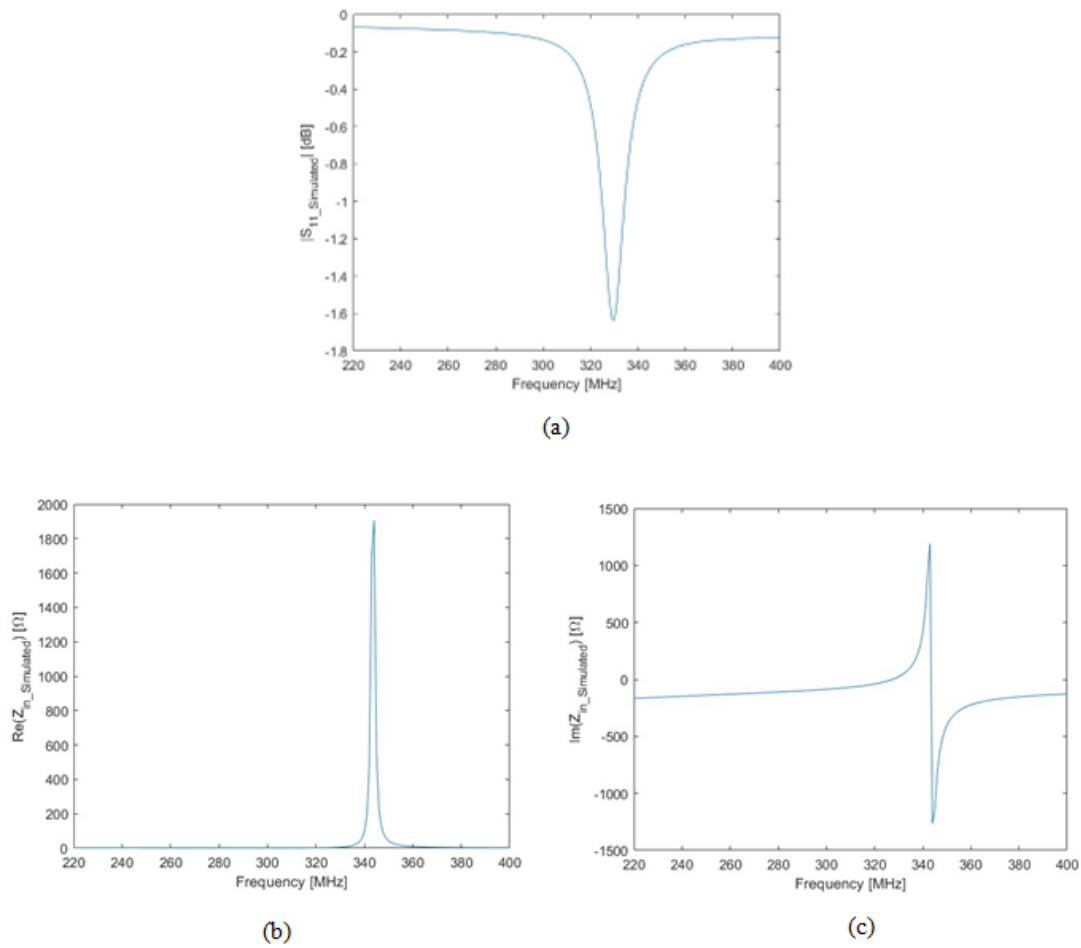


Figure A.2: Frequency response of Helix 2 connected at the end of one-inch microstrip line simulated on HFSS: a) $|S_{11_Simulated}|$ [dB]; b) $\text{Re}(Z_{in_Simulated})$ [Ω]; c) $\text{Im}(Z_{in_Simulated})$ [Ω].

A.2.3 Two-inch microstrip line

Helix 2 is connected at one end of a two-inch microstrip line, and the 50Ω generator input is connected at the other end of the microstrip line. Figure A.3 shows the computed frequency response of Helix 2 connected to the two-inch microstrip line. Specifically, Figure A.3a displays the magnitude of the reflection coefficient ($|S_{11_Simulated}|$), while Figures A.3b and A.3c show the real and imaginary parts of the input impedance, respectively.

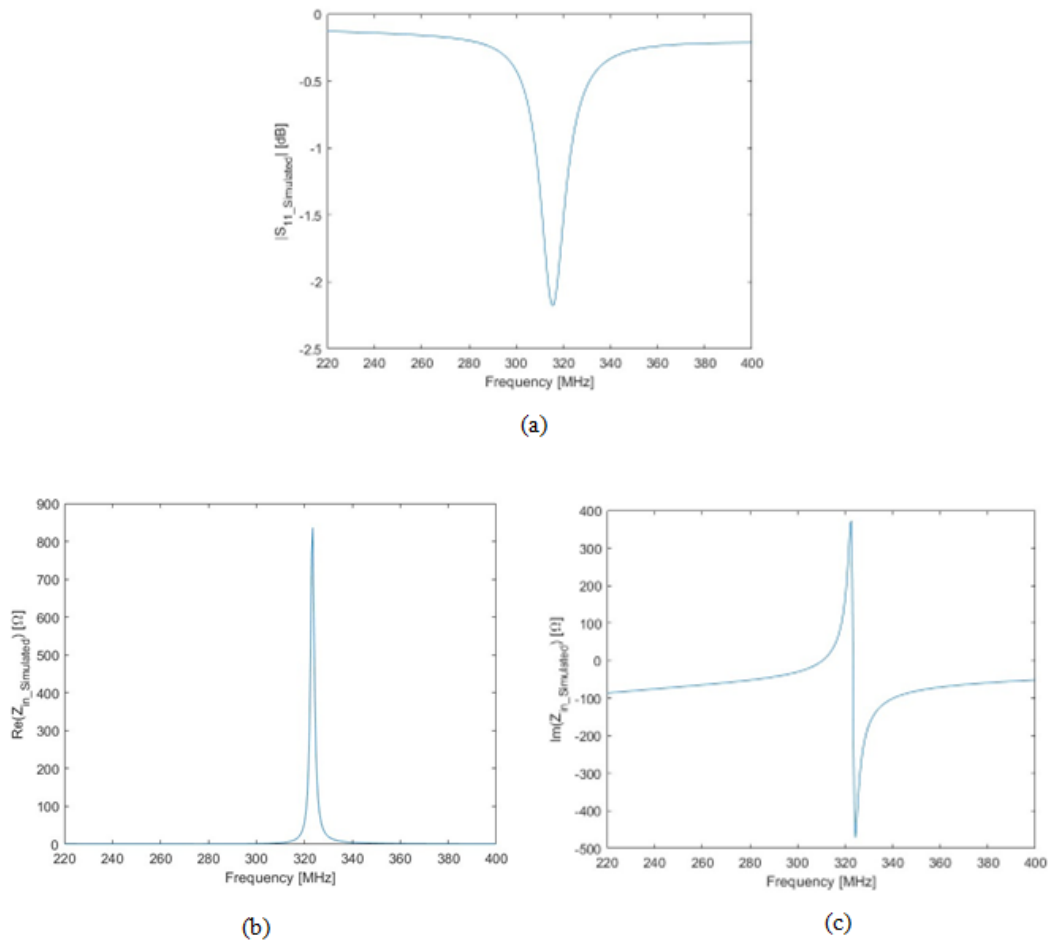


Figure A.3: Frequency response of Helix 2 connected at the end of two-inch microstrip line simulated on HFSS: a) $|S_{11_Simulated}|$ [dB]; b) $\text{Re}(Z_{in_Simulated})$ [Ω]; c) $\text{Im}(Z_{in_Simulated})$ [Ω].

A.2.4 Three-inch microstrip line

Helix 2 is connected at one end of a three-inch microstrip line, and the 50Ω generator input is connected at the other end of the microstrip line. Figure A.4 shows the computed frequency response of Helix 2 connected to the three-inch microstrip line. Specifically, Figure A.4a displays the magnitude of the reflection coefficient ($|S_{11_Simulated}|$), while Figures A.4b and A.4c show the real and imaginary parts of the input impedance, respectively.

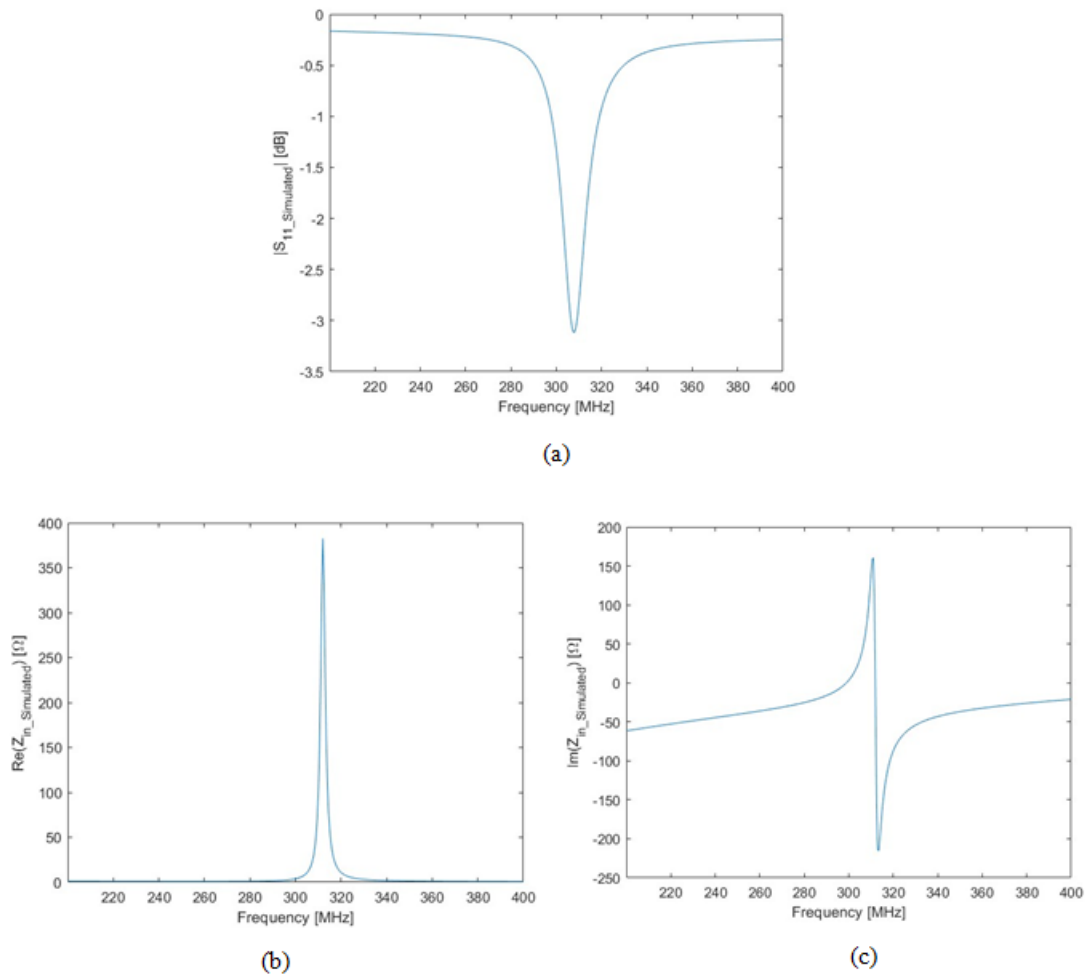


Figure A.4: Frequency response of Helix 2 connected at the end of three-inch microstrip line simulated on HFSS: a) $|S_{11_Simulated}|$ [dB]; b) $\text{Re}(Z_{in_Simulated})$ [Ω]; c) $\text{Im}(Z_{in_Simulated})$ [Ω].

A.3 Simulations of NMHAS with Helix 2 on WIPL-D

This section discusses the simulations using WIPL-D of Helix 2 connected to different lengths of microstrip line. The dimensions of the structure used for the WIPL-D simulations are the same used in the ANSYS-HFSS simulations.

A.3.1 Half-inch microstrip line

Fig A.5 shows the frequency response of Helix 2 connected to half-inch microstrip line. Fig A.5a shows the magnitude of reflection coefficient ($|S_{11_Simulated}|$), Fig A.5b shows the real part of input impedance and Fig A.5c shows the imaginary part of input impedance.

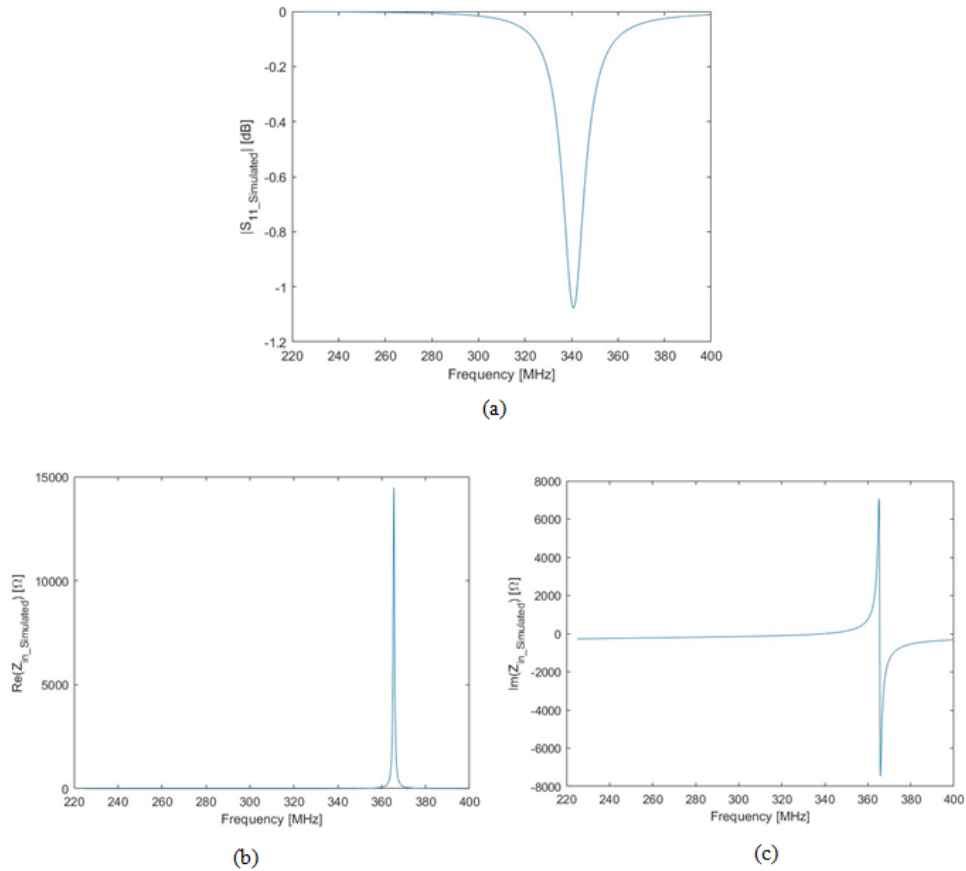


Figure A.5: Frequency response of Helix 2 connected at the end of half-inch microstrip line simulated on WIPL-D: a) $|S_{11_Simulated}|$ [dB]; b) $Re(Z_{in_Simulated})$ [Ω]; c) $Im(Z_{in_Simulated})$ [Ω].

A.3.2 One-inch microstrip line

Fig A.6 shows the frequency response of Helix 2 connected to one-inch microstrip line. Fig A.6a shows the magnitude of reflection coefficient ($|S_{11_Simulated}|$), Fig A.6b shows the real part of input impedance and Fig A.6c shows the imaginary part of input impedance.

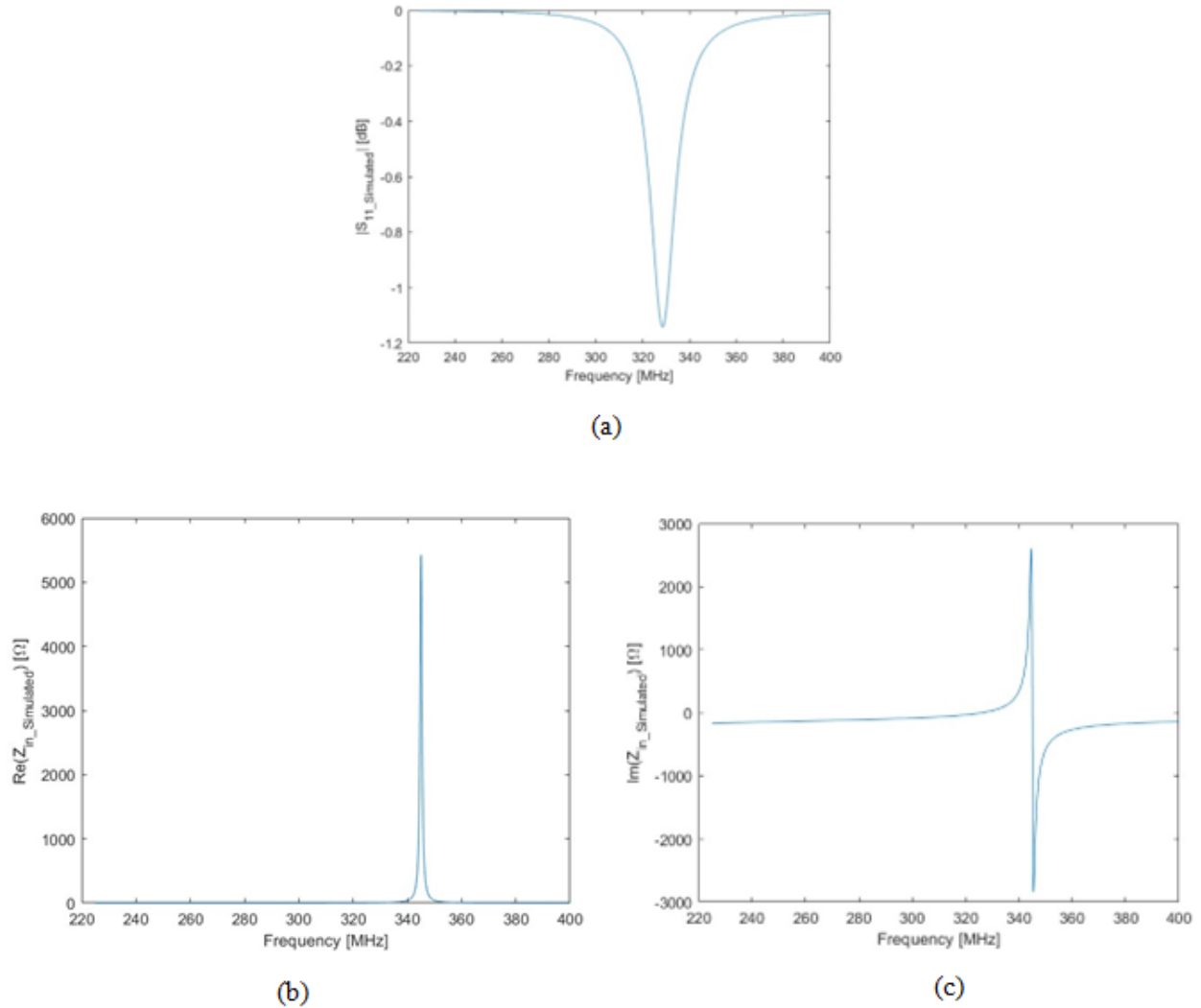


Figure A.6: Frequency response of Helix 2 connected at the end of one-inch microstrip line simulated on WIPL-D: a) $|S_{11_Simulated}|$ [dB]; b) $\text{Re}(Z_{in_Simulated})$ [Ω]; c) $\text{Im}(Z_{in_Simulated})$ [Ω].

A.3.3 Two-inch microstrip line

Fig A.7 shows the frequency response of Helix 2 connected to two-inch microstrip line. Fig A.7a shows the magnitude of reflection coefficient ($|S_{11_Simulated}|$), Fig A.7b shows the real part of input impedance and Fig A.7c shows the imaginary part of input impedance.

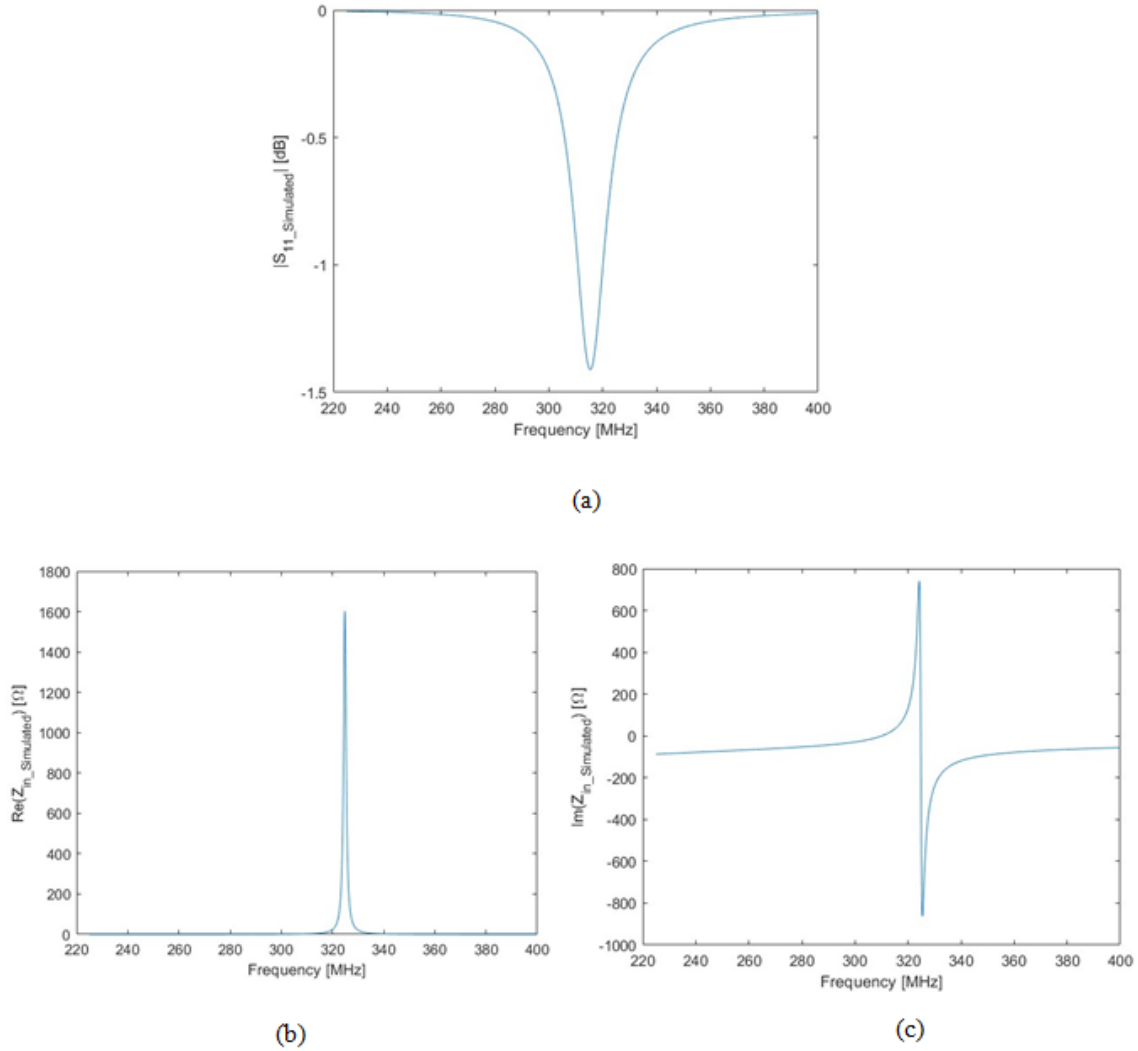


Figure A.7: Frequency response of Helix 2 connected at the end of two-inch microstrip line simulated on WIPL-D: a) $|S_{11_Simulated}|$ [dB]; b) $\text{Re}(Z_{in_Simulated})$ [Ω]; c) $\text{Im}(Z_{in_Simulated})$ [Ω].

A.3.4 Three-inch microstrip line

Figure A.8 shows the frequency response of Helix 2 connected to three-inch microstrip line. Figure A.8a shows the magnitude of reflection coefficient ($|S_{11_Simulated}|$), Figure A.8b shows the real part of input impedance and Figure A.8c shows the imaginary part of input impedance.

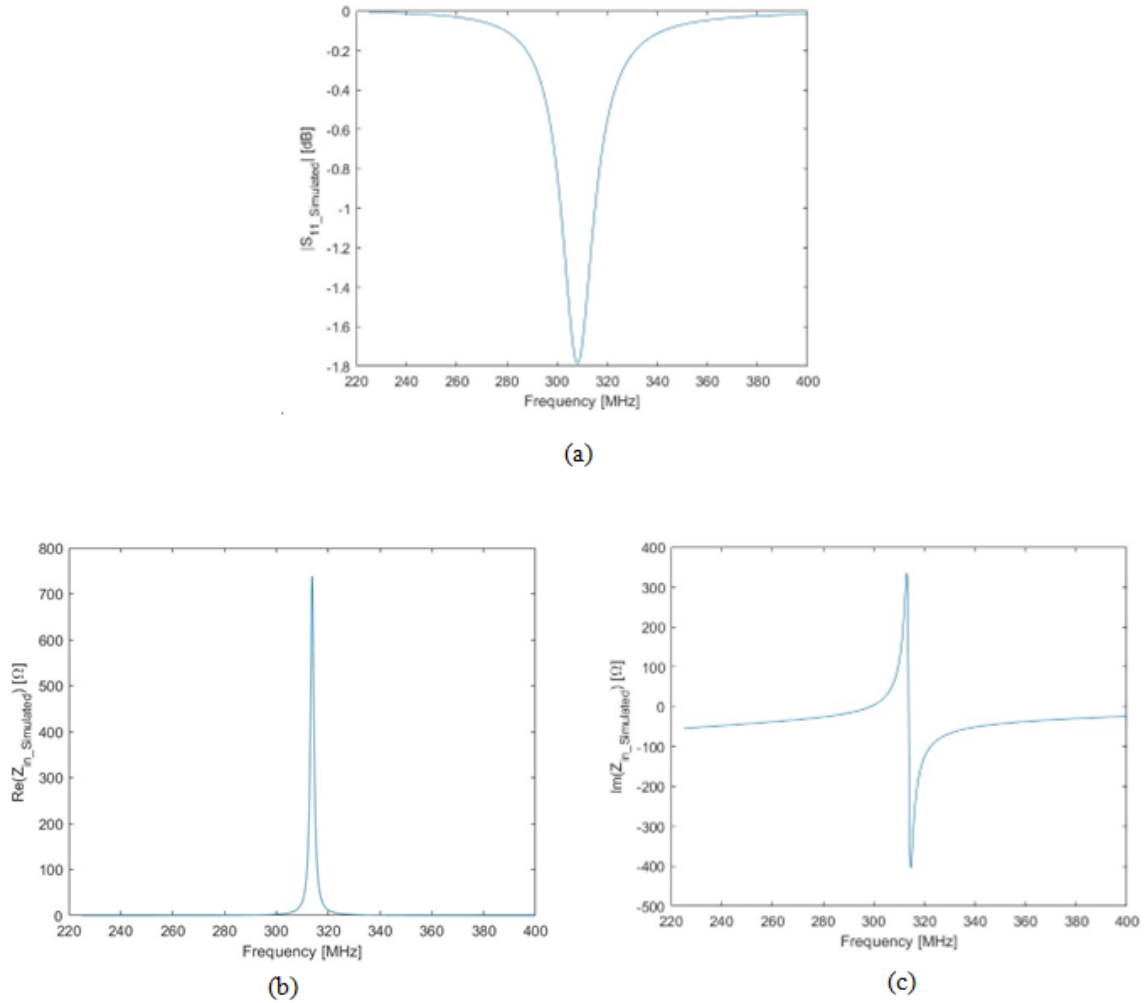


Figure A.8: Frequency response of Helix 2 connected at the end of three-inch microstrip line simulated on WIPL-D: a) $|S_{11_Simulated}|$ [dB]; b) $\text{Re}(Z_{in_Simulated})$ [Ω]; c) $\text{Im}(Z_{in_Simulated})$ [Ω].

APPENDIX B. MEASUREMENT OF HELIX 2 CONNECTED TO DIFFERENT MICROSTRIP LINES

This appendix shows the measurements of Helix 2 connected to different microstrip lines in both the laboratory and the anechoic chamber.

B.1 Measurements of Helix 2 connected to different microstrip lines in laboratory setup

This section discusses the response of the NMHAS when Helix 2 is connected to different microstrip lines measured in Laboratory setup as shown in Figure 5.1a.

B.1.1 Half inch microstrip line

Figure B.1 shows the S_{11} and respective impedance response at Plane B (Figure 4.5) when Helix 2 is connected to half inch microstrip line.

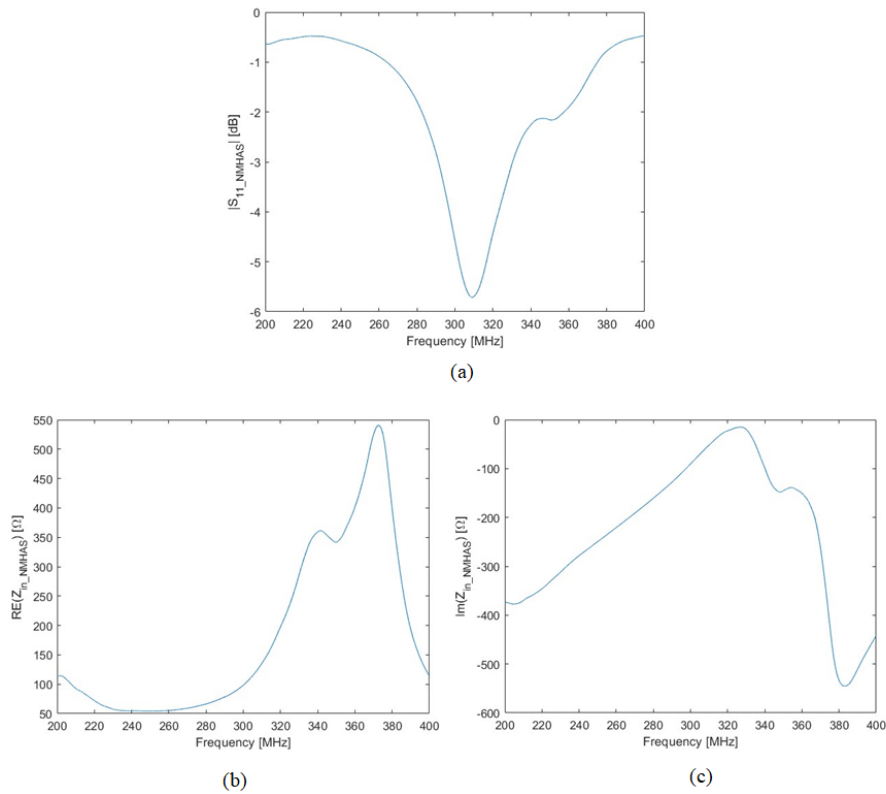


Figure B.1: Measured response of Helix 2 connected to half inch microstrip line in setup shown in Figure 5.1a: a.) $|S_{11_NMHAS}|$ [dB]; b.) $\text{Re}(Z_{in_NMHAS})$ [Ω]; c) $\text{Im}(Z_{in_NMHAS})$ [Ω].

B.1.2 One inch microstrip line

Figure B.2 shows the S_{11} and respective impedance response at Plane B (Figure 4.5) when Helix 2 is connected to one inch microstrip line.

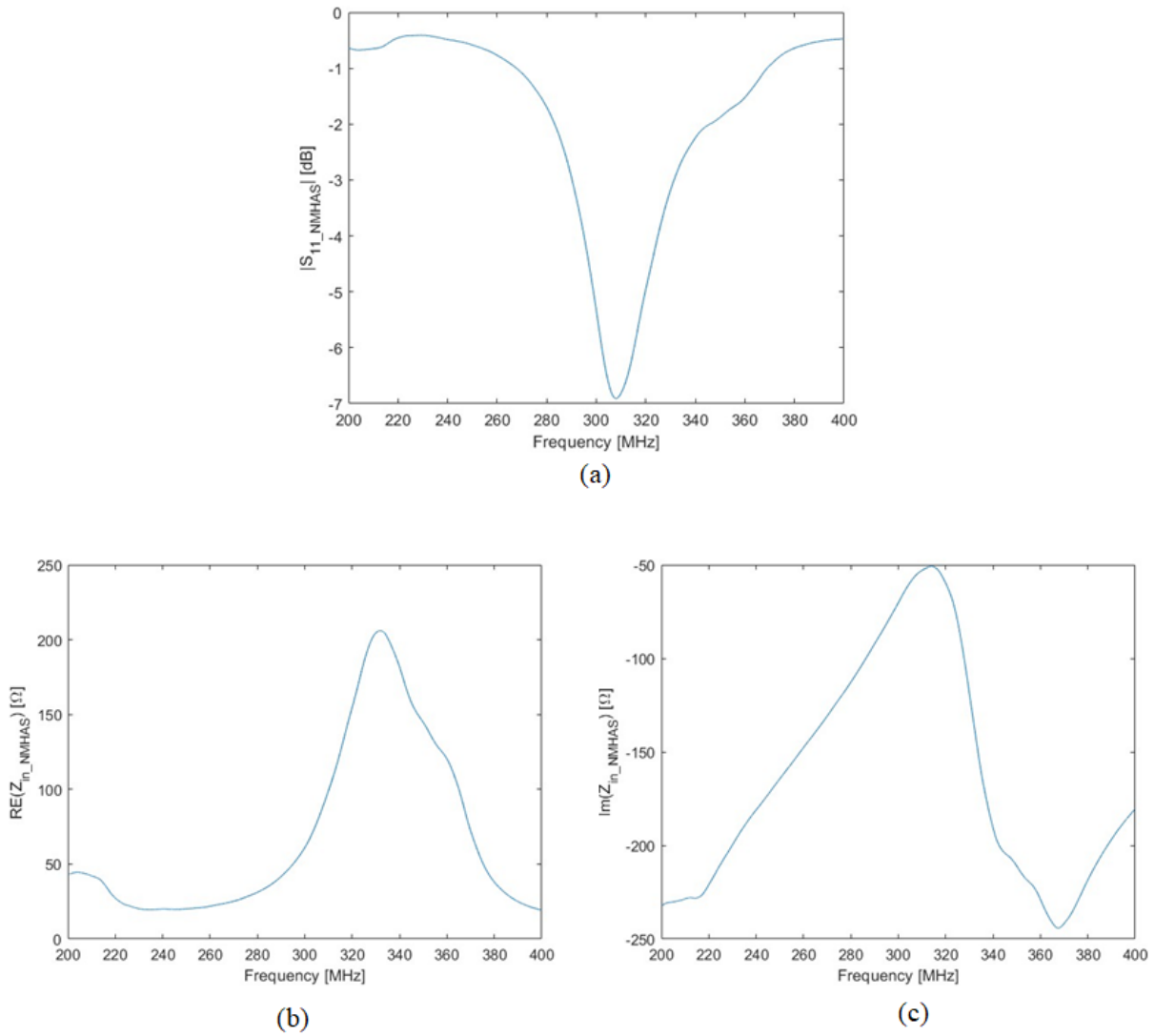


Figure B.2: Measured response of Helix 2 connected to one inch microstrip line in setup shown in Figure 5.1a: a.) $|S_{11_NMHAS}|$ [dB]; b.) $RE(Z_{in_NMHAS})$ [Ω]; c.) $Im(Z_{in_NMHAS})$ [Ω].

B.1.3 Two inch microstrip line

Figure B.3 shows the S_{11} and respective impedance response at Plane B (Figure 4.5) when Helix 2 is connected to two inch microstrip line.

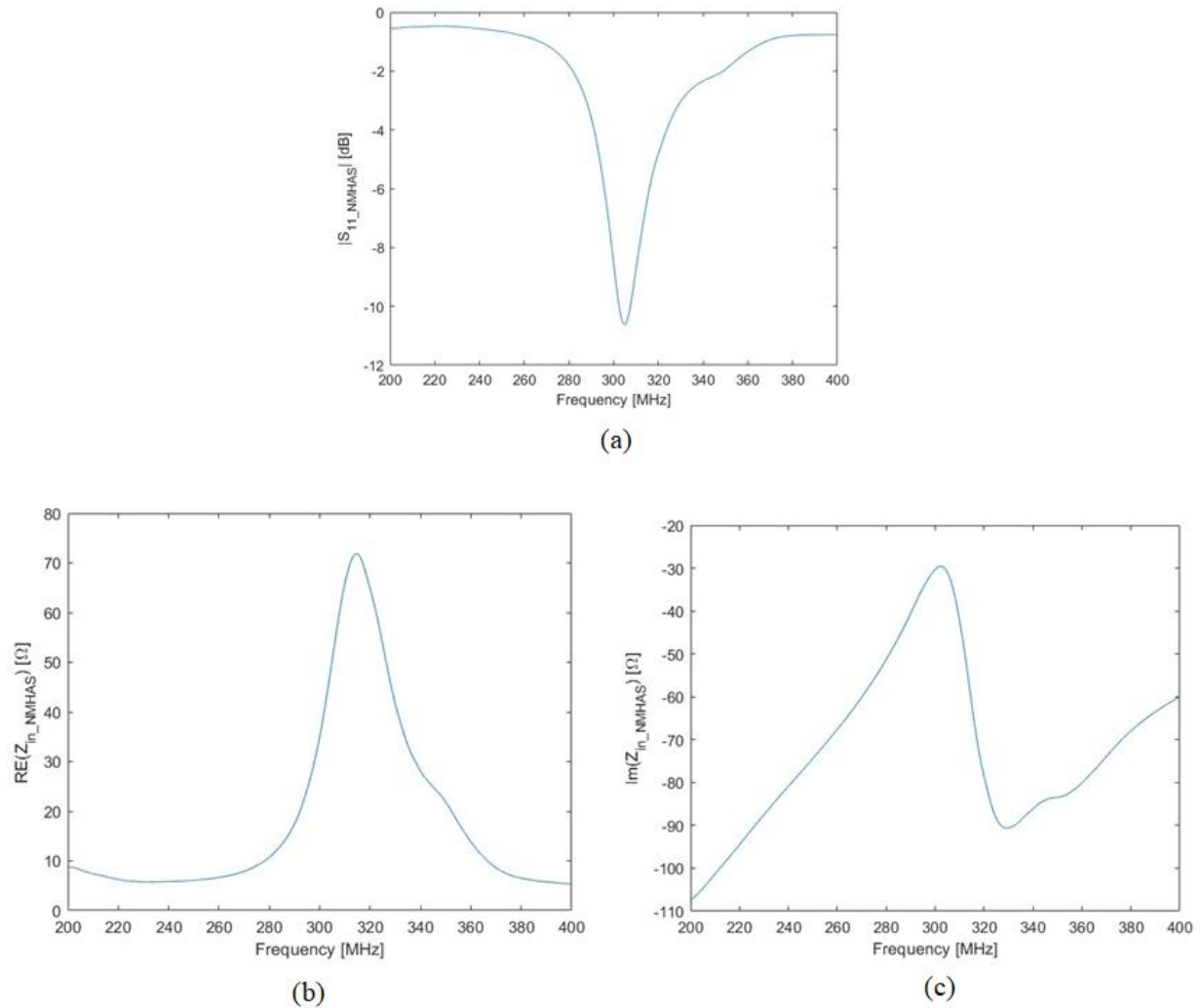


Figure B.3: Measured response of Helix 2 connected to two inch microstrip line in setup shown in Figure 5.1a: a.) $|S_{11_NMHAS}|$ [dB]; b.) $\text{Re}(Z_{in_NMHAS})$ [Ω]; c) $\text{Im}(Z_{in_NMHAS})$ [Ω].

B.1.4 Three inch microstrip line

Figure B.4 shows the S_{11} and respective impedance response at Plane B (Figure 4.5) when Helix 2 is connected to three inch microstrip line.

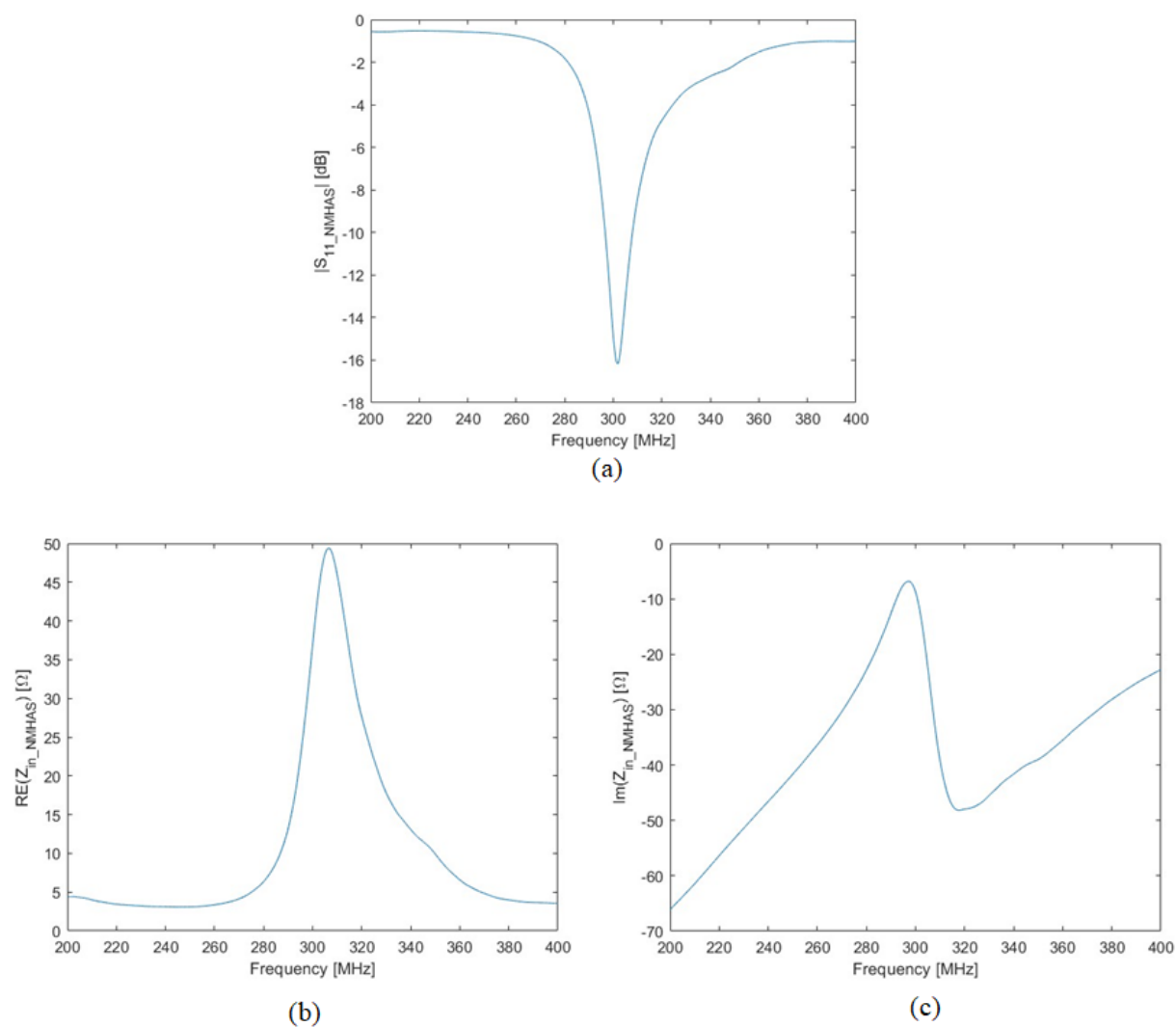


Figure B.4: Measured response of Helix 2 connected to three inch microstrip line in setup shown in Figure 5.1a: a.) $|S_{11_NMHAS}|$ [dB]; b.) $\text{Re}(Z_{in_NMHAS})$ [Ω]; c.) $\text{Im}(Z_{in_NMHAS})$ [Ω].

B.2 Measurements of Helix 2 connected to different microstrip lines in anechoic chamber

This section discusses the response of the NMHAS when Helix 2 is connected to different microstrip lines measured in an anechoic chamber as shown in Figure 5.1b.

B.2.1 Half inch microstrip line

Figure B.5 shows the S_{11} and respective impedance response at Plane B (Figure 4.5) when Helix 2 is connected to half inch microstrip line.

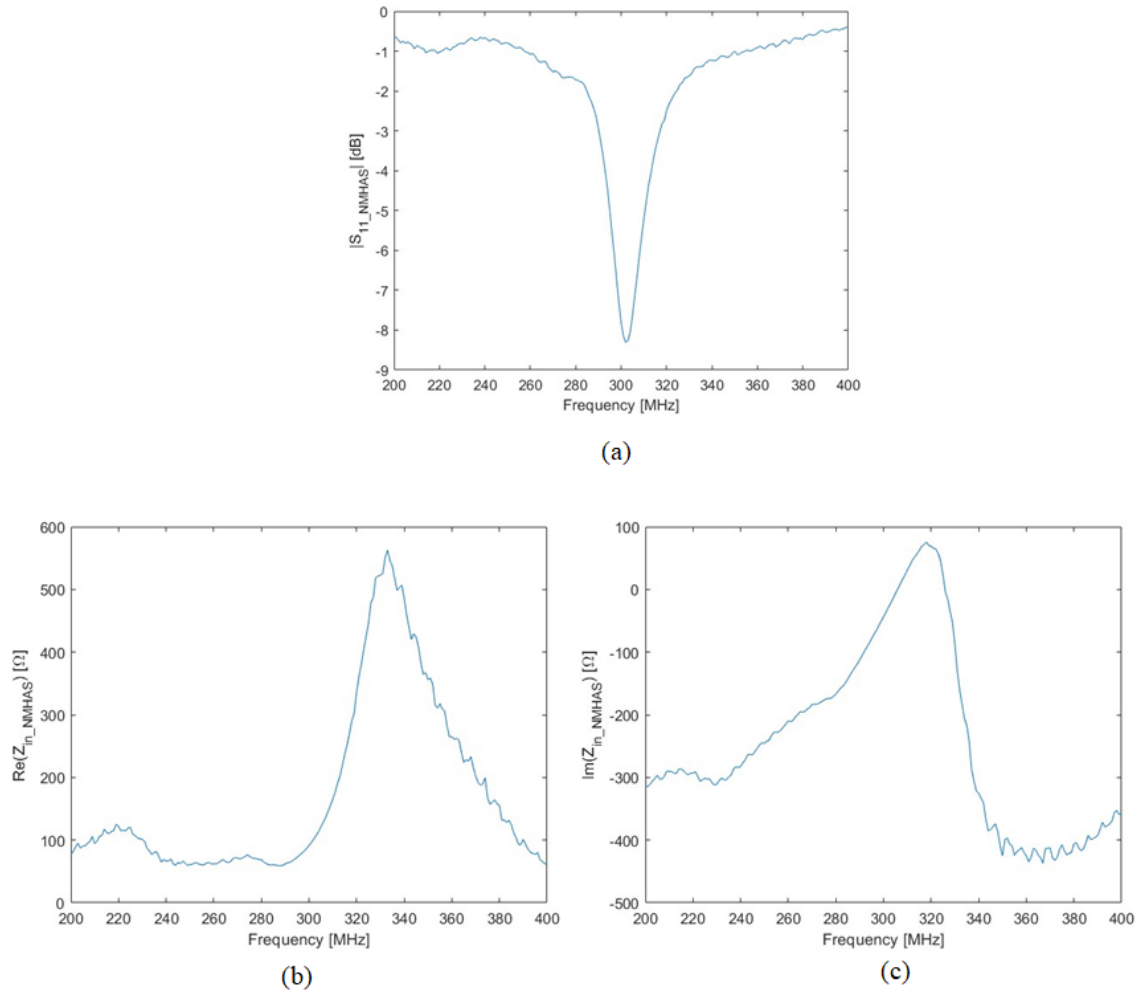


Figure B.5: Measured response of Helix 2 connected to half inch microstrip line in setup shown in Figure 5.1b: a.) $|S_{11_NMHAS}|$ [dB]; b.) $\text{Re}(Z_{in_NMHAS})$ [Ω]; c.) $\text{Im}(Z_{in_NMHAS})$ [Ω].

B.2.2 One inch microstrip line

Figure B.6 shows the S_{11} and respective impedance response at Plane B (Figure 4.5) when Helix 2 is connected to one inch microstrip line.

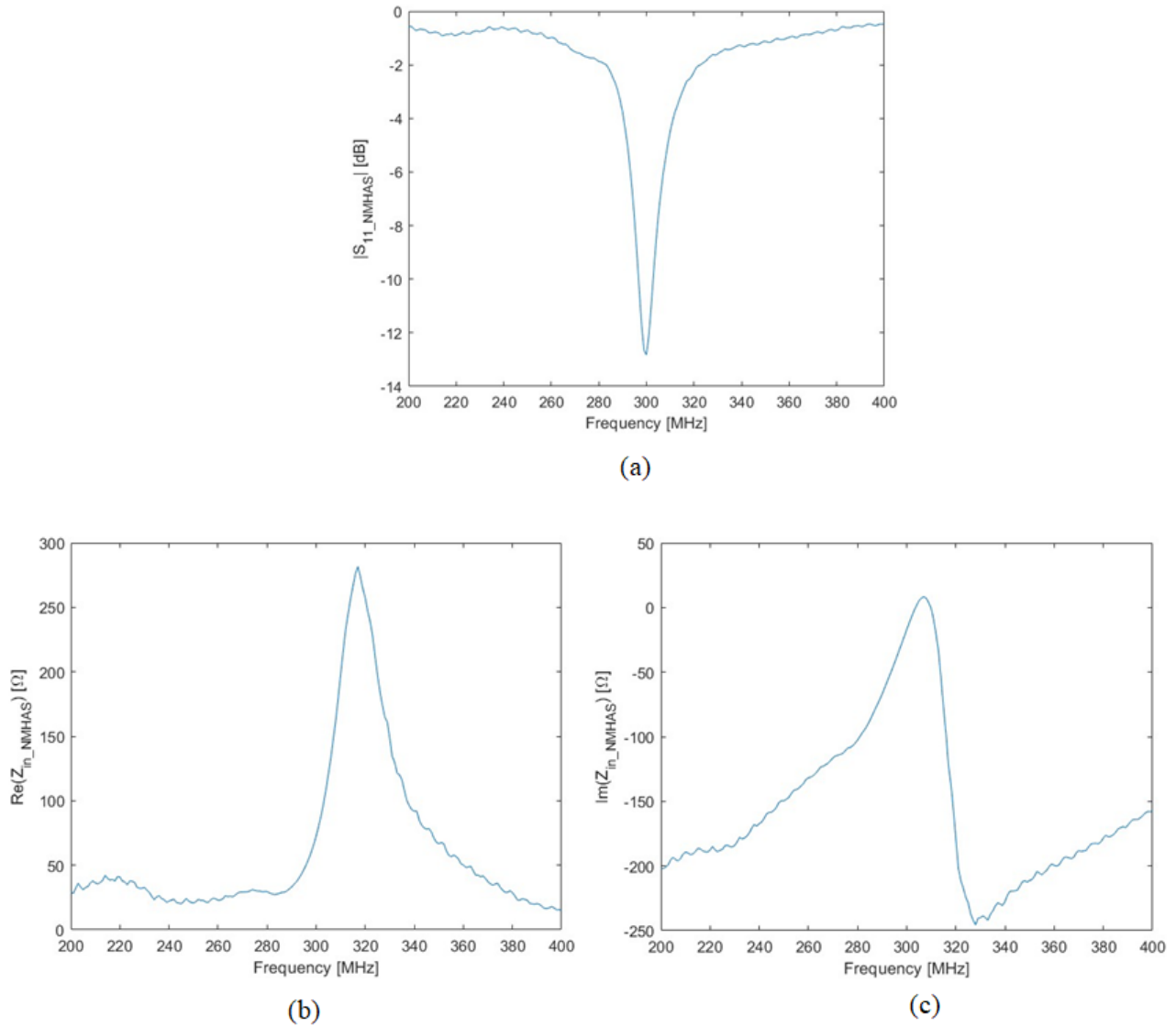


Figure B.6: Measured response of Helix 2 connected to one inch microstrip line in setup shown in Figure 5.1b: a.) $|S_{11_NMHAS}|$ [dB]; b.) $\text{Re}(Z_{in_NMHAS})$ [Ω]; c.) $\text{Im}(Z_{in_NMHAS})$ [Ω].

B.2.3 Two inch microstrip line

Figure B.7 shows the S_{11} and respective impedance response at Plane B (Figure 4.5) when Helix 2 is connected to two inch microstrip line.

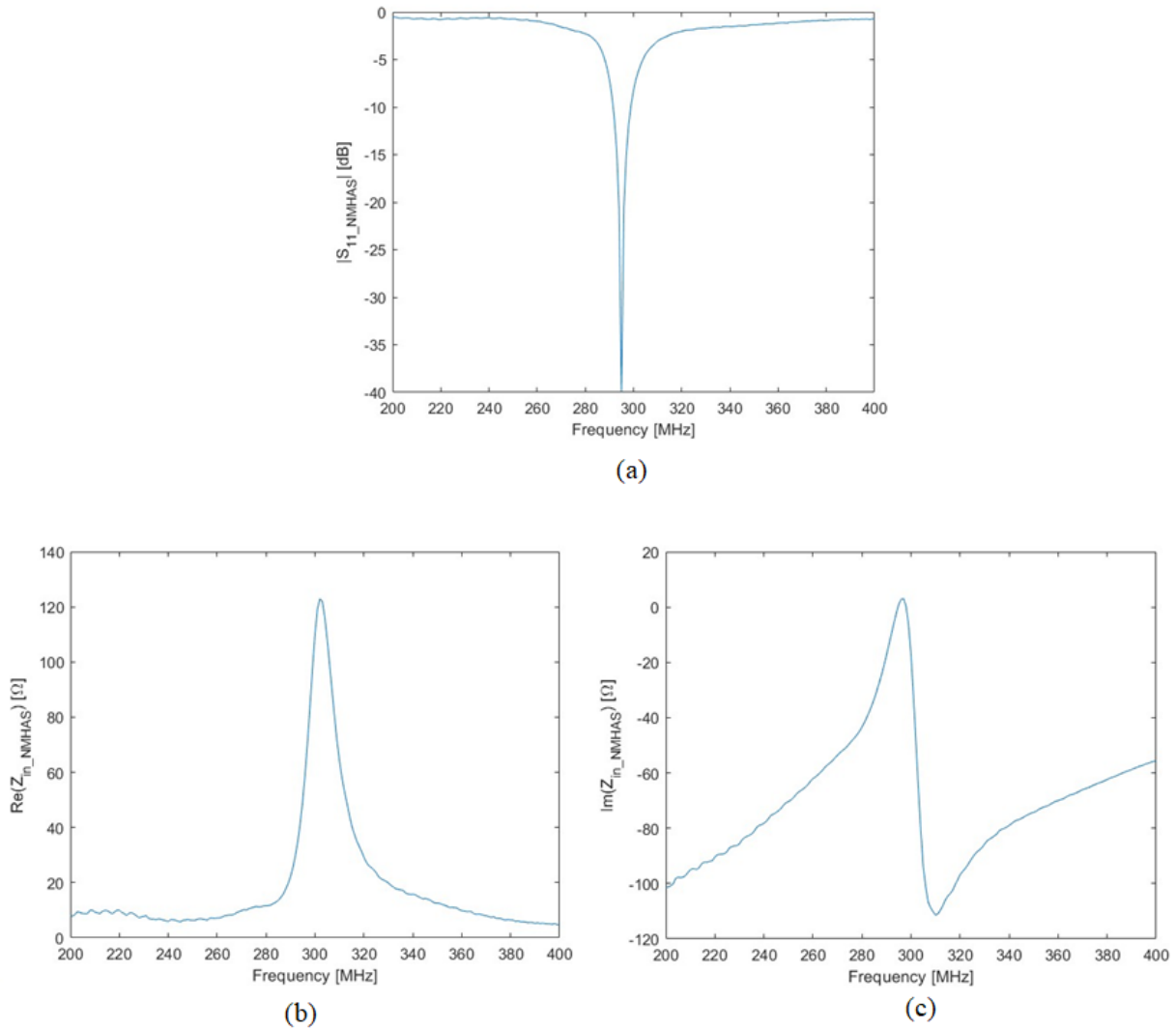


Figure B.7: Measured response of Helix 2 connected to two inch microstrip line in setup shown in Figure 5.1b: a.) $|S_{11_NMHAS}|$ [dB]; b.) $\text{Re}(Z_{in_NMHAS})$ [Ω]; c) $\text{Im}(Z_{in_NMHAS})$ [Ω].

B.2.4 Three inch microstrip line

Figure B.8 shows the S_{11} and respective impedance response at Plane B (Figure 4.5) when Helix 2 is connected to three inch microstrip line.

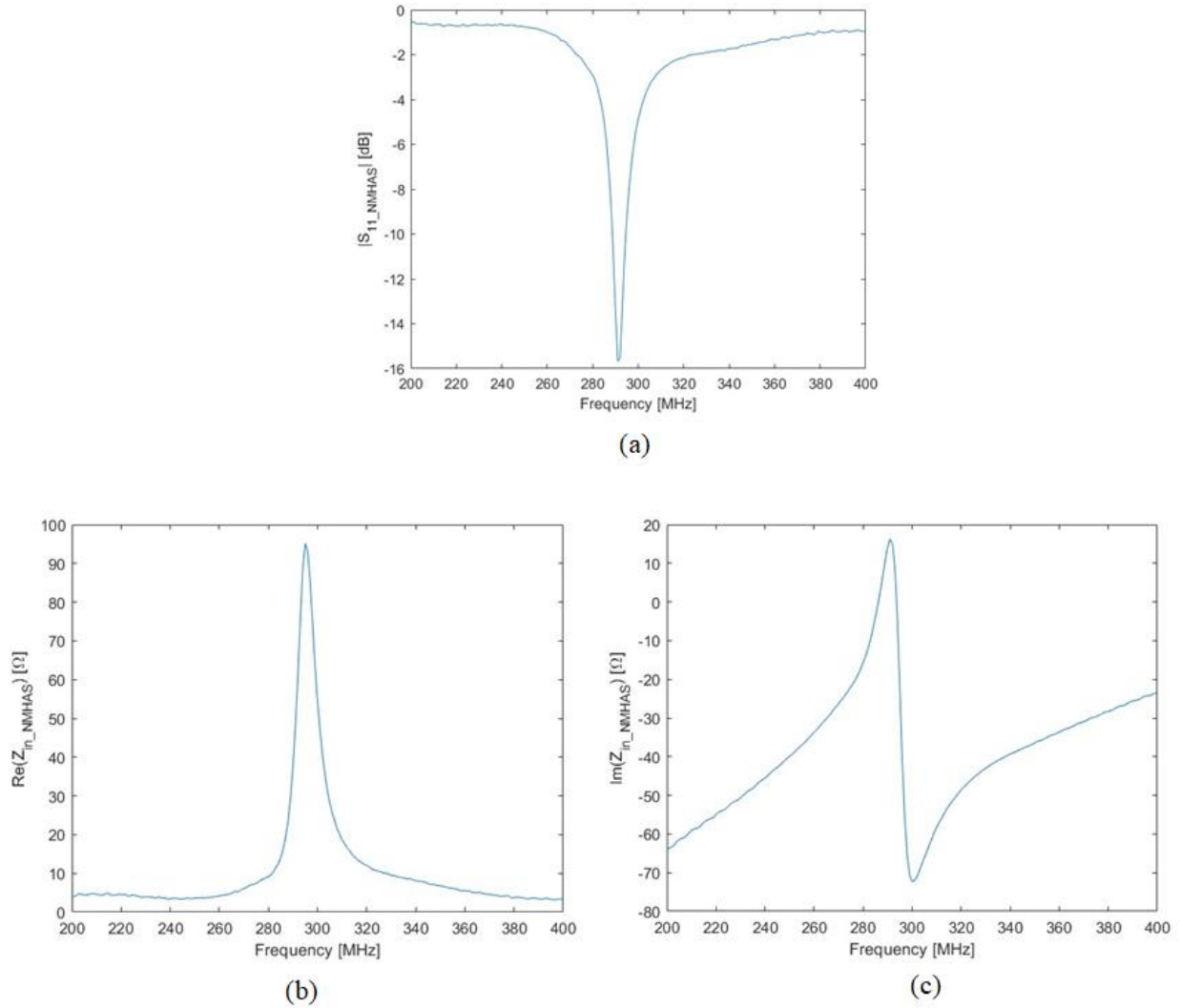


Figure B.8: Measured response of Helix 2 connected to three inch microstrip line in setup shown in Figure 5.1b: a.) $|S_{11_NMHAS}|$ [dB]; b.) $\text{Re}(Z_{in_NMHAS})$ [Ω]; c.) $\text{Im}(Z_{in_NMHAS})$ [Ω].

APPENDIX C. TRANSFERRING OF IMPEDANCE

This appendix details the MATLAB code used to transfer S_{11} and impedance measured at Plane A to Plane B (Figure 4.5). Figure C.1 shows the representation of MATLAB code implemented to calculate the S_{11} and impedance at Plane B.

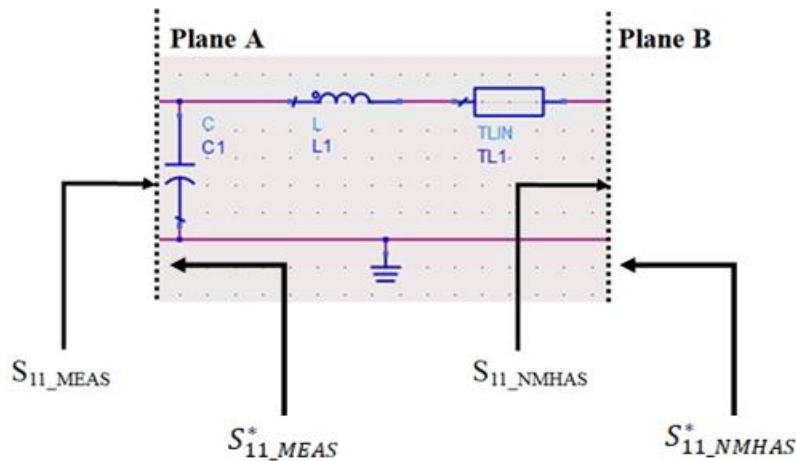


Figure C.1: Representation of MATLAB code implemented.

Below is given the MATLAB code for Function. The conjugate of S_{11_MEAS} , $S_{11_MEAS}^*$ is calculated

```
function [zin,s11_f,s11_db,freq] = transformation_ac(SMA)
c=2.1e-12;                               %%capacitor value C = 2.1pF
l=13e-9;                                 %%inductor value L = 13nH
k=1/(30*300e6);                          %%k = d/v where d is the distance and v is the phase velocity

freq = SMA(:,1);                          %%define first column as frequency
length = size(freq);
s11_db = SMA(:,2);
s11_mag = db2mag(s11_db);
s11_ang = SMA(:,3);
s11_ang_rad = deg2rad(s11_ang);
[s11_r,s11_i] = pol2cart(s11_ang_rad,s11_mag);
s11 = s11_r + 1i*s11_i;                   %%define s11 as measured at the end of SMA connector
top = 1+s11;
bottom = 1-s11;
nor_z11 = top ./ bottom;                  %%calculating normalized z11 at the end of the SMA
                                          connector
z11 = 50*nor_z11;                         %%calculating impedance at the end of the SMA connector
```

```

re = real(z11);
im = imag(z11);
con_z11 = re - 1i*im;           %%calculating conjugate of impedance at SMA connector
con_y11 = 1./con_z11;          %%calculating conjugate admittance
for i = 1:length                %%initializing a for loop
    z_c(i,1) = -1i/(2*pi*freq(i)*c); %%calculating impedance of capacitor
                                        connected in parallel
    z_l(i,1) = 1i*2*pi*freq(i)*l;      %%calculating impedance of inductor
                                        connected in series
    y_c(i,1) = 1./z_c(i,1);            %%admittance of the capacitor in parallel
    y_p(i,1) = con_y11(i,1) + y_c(i,1); %%parallel combination conjugate z11 and
                                        capacitor (admittance of the combination)
    z_p(i,1) = 1/y_p(i,1);             %%impedance of parallel combination
    z_s(i,1) = z_p(i,1) + z_l(i,1);    %%adding the impedance of series inductor
    nor_zs(i,1) = z_s(i,1)/50;         %%normalizing the total impedance
    top_s11m(i,1) = nor_zs(i,1)-1;
    bottom_s11m(i,1) = nor_zs(i,1)+1;
    s11m(i,1) = top_s11m(i,1)/bottom_s11m(i,1); %%calculating s11 at end of the
                                        inductor
    [theta(i,1), mag_s(i,1)] = cart2pol(real(s11m(i,1)), imag(s11m(i,1))); %%converting
                                        cartesian form to polar form
    ang(i,1) = rad2deg(theta(i,1));    %%changing the angle in radians to degrees
    ang_r(i,1) = ang(i,1)-2*k*360*freq(i,1); %%adding the phase introduced by
                                        transmission line
    ang_m(i,1) = deg2rad(ang_r(i,1));  %%converting the angle in degrees to radian
    [real_sfc(i,1),im_sfc(i,1)] = pol2cart(ang_m(i,1), mag_s(i,1)); %%converting the
                                        s11 into real imaginary using the modified angle
    sfc(i,1) = real_sfc(i,1)+1i*im_sfc(i,1); %%s11 at the end of transmission line
    top_zcon(i,1) = 1+sfc(i,1);
    bottom_zcon(i,1) = 1-sfc(i,1);
    nor_zcon(i,1) = top_zcon(i,1)/bottom_zcon(i,1);
    zcon(i,1) = 50*nor_zcon(i,1);
    zin(i,1) = real(zcon(i,1))-1i*imag(zcon(i,1)); %%finding zin using s11
                                        %%finding conjugate of zin
    nor_zin(i,1) = zin(i,1)/50;
    s11_f(i,1) = (nor_zin(i,1)-1)/(nor_zin(i,1)+1); %%s11 with conjugate zin value
    s11_db(i,1) = mag2db(abs(s11_f(i,1))); %%magnitude of s11 in db
end
s11_f;
s11_db;
zin;
end

```

APPENDIX D. SENSITIVITY OF NMHAS TO PHYSICAL DIMENSIONS OF THE STRUCTURE

D.1 Compression

For compressing the helical structure, a rubber band is stretched across the ends of the helical structure. This caused a slight bend in the structure and hence is not uniformly compressed.

Figure D.1 shows the setup of the compressed structure in anechoic chamber.

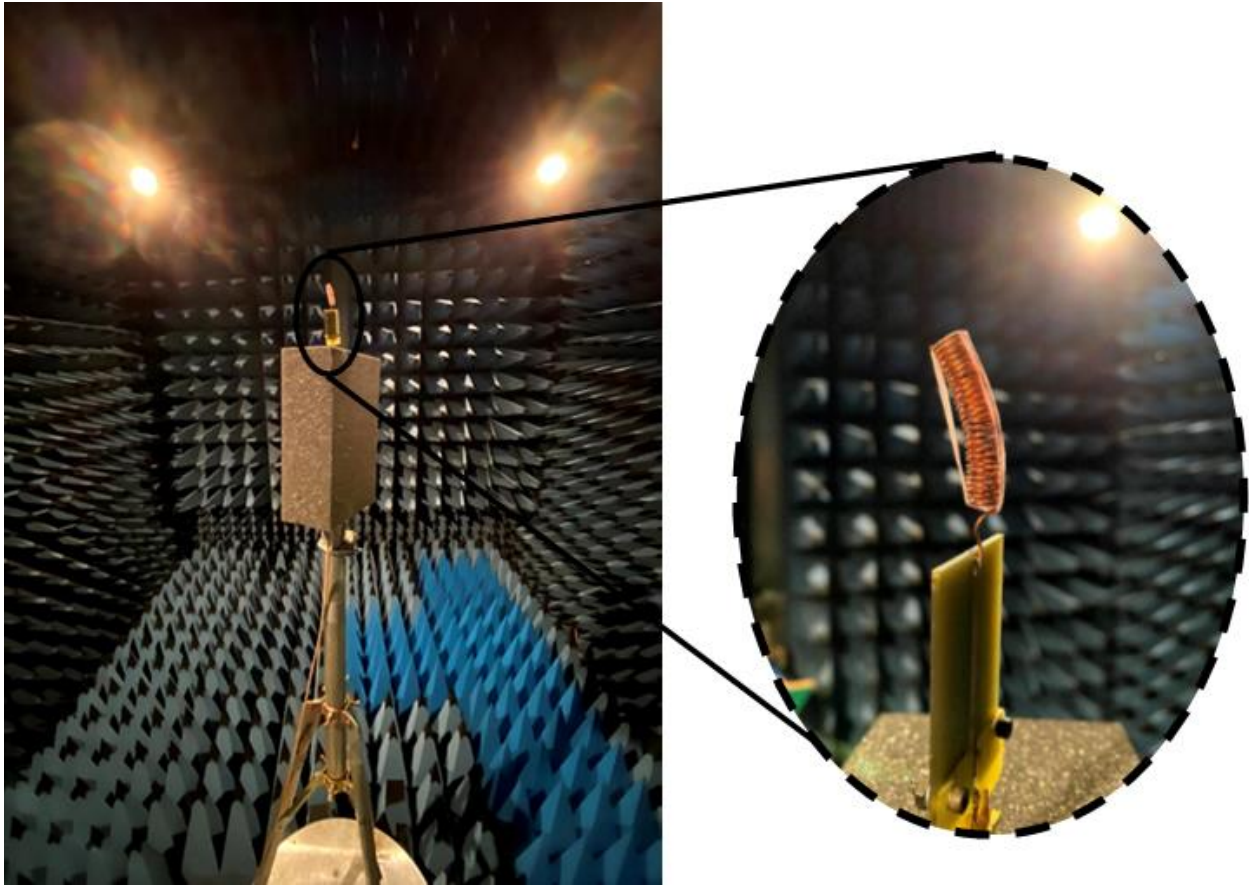
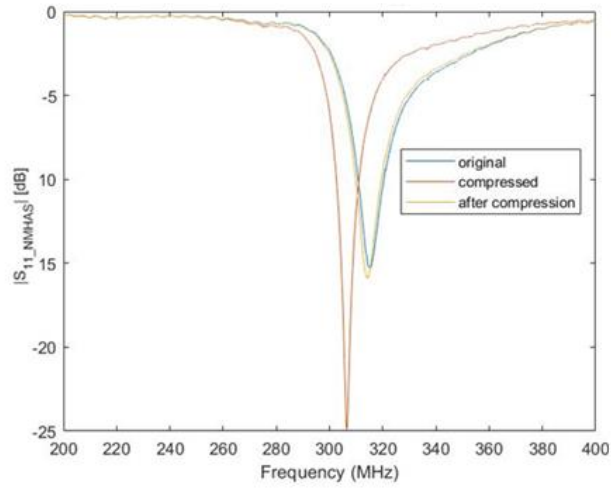
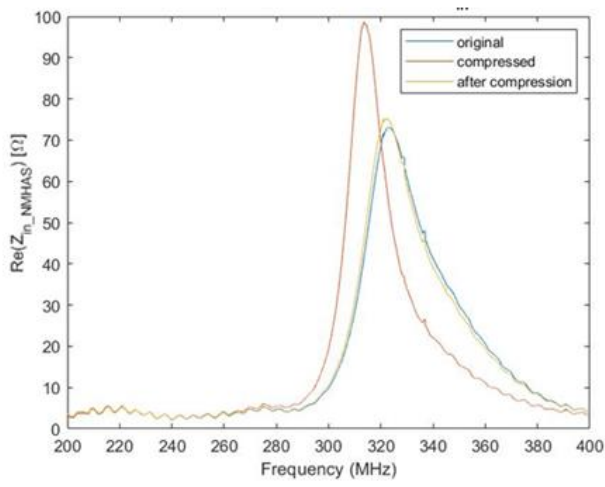


Figure D.1: Compressed helix connected to a two inch microstrip line mounted on a tripod in the anechoic chamber.

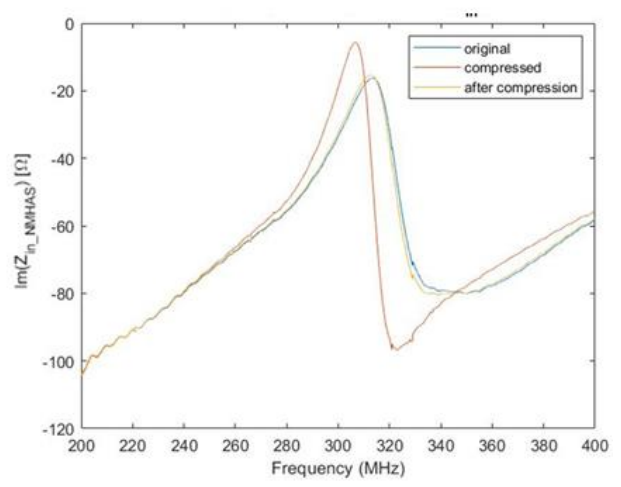
Figure D.2 shows the response of the NMHAS when the helix was compressed. It can be seen that the resonant frequency decreases as observed from the simulation measurements reported in Chapter 3.



(a)



(b)



(c)

Figure D.2: Measured response of compressed helical structure when connected to a two inch microstrip line: a.) $|S_{11_NMHAS}|$ [dB]; b.) $\text{Re}(Z_{in_NMHAS})$ [Ω]; c.) $\text{Im}(Z_{in_NMHAS})$ [Ω].

D.2 Expansion

The helical structure was elongated keeping the diameter of the helix constant. Figure D.3 shows the elongated NMHAS mounted on antenna mounting structure in the anechoic chamber. The spacing between the turns of the helix was increased by using cardboard pieces of thickness 0.6 mm.

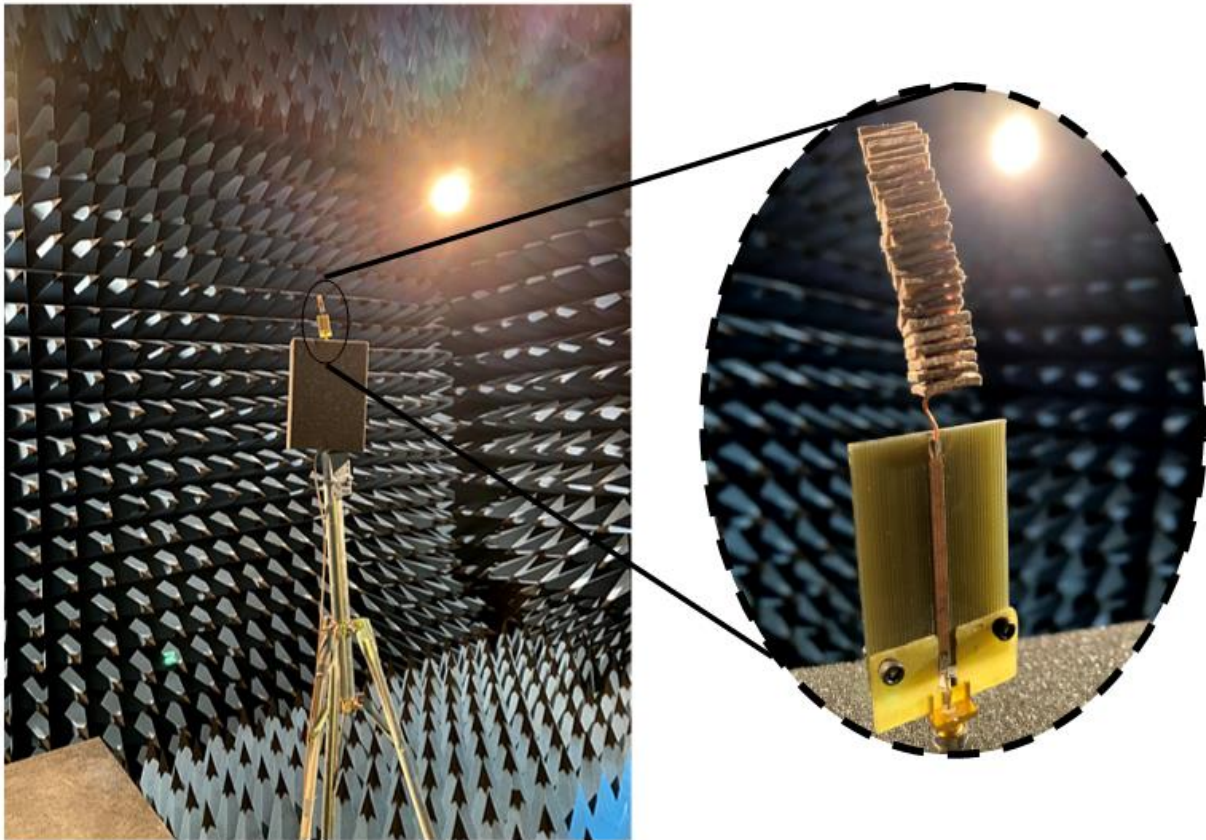
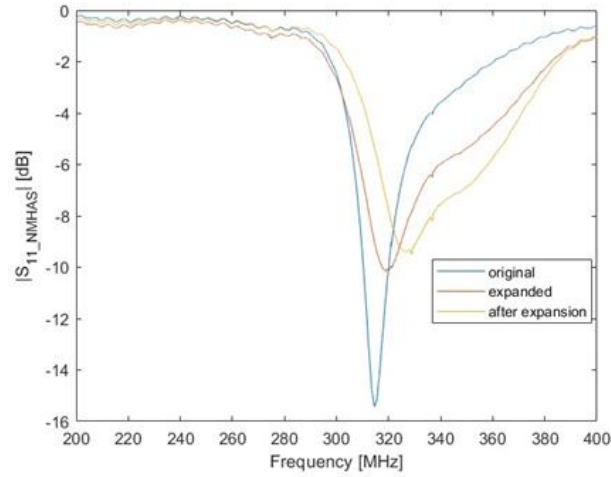
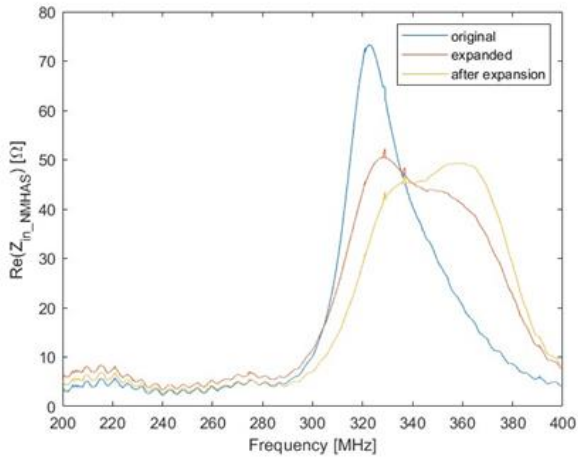


Figure D.3: Elongated helix connected to a two inch microstrip line mounted on a tripod in the anechoic chamber

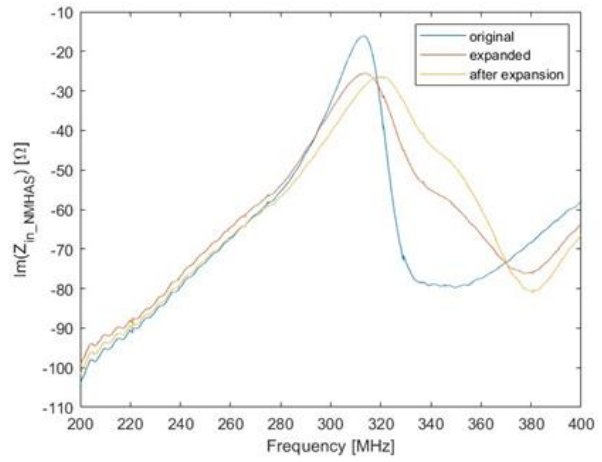
Figure D.4 shows the response of the NMHAS when the helix was expanded. Same helix was used for both expansion and compression measurements. Hence, any discrepancies in the response can be attributed to changes in physical dimensions of the helix due to multiple compressions and expansions.



(a)



(b)



(c)

Figure D.4: Measured response of elongated helical structure when connected to a two inch microstrip line: a.) $|S_{11_NMHAS}|$ [dB]; b.) $\text{Re}(Z_{in_NMHAS})$ [Ω]; c.) $\text{Im}(Z_{in_NMHAS})$ [Ω].

BIOGRAPHY OF THE AUTHOR

Sri Lekha Srimat Kilambi was born in Hyderabad, Telangana, India in 1997. She graduated from Osmania University, College of Engineering, Hyderabad, Telangana, India in 2018 with a B.E in Electronics and Communication Engineering. Her research interests include Electromagnetics and RF Antennas. Miss. Srimat Kilambi has worked as a graduate research assistant in the Microwave Acoustics Laboratory and as a graduate teaching assistant for ECE 210 Electric Circuits I, ECE 351 Fields and Waves, ECE 453 Microwave Engineering, and ECE 465 Introduction to Sensors. Miss. Srimat Kilambi presented a paper at the Antenna Measurements and Techniques Association in 2022. Sri Lekha Srimat Kilambi is a candidate for the Master of Science degree in Electrical Engineering from the University of Maine in December 2023.